Master's Thesis

ASSESSMENT OF GULLY EROSION BY LINKING PHOTOGRAMMETRIC APPROACHES AND FIELD MEASUREMENTS

for attainment of the academic degree of

Diplomingenieur

presented to the

Institute of Hydraulics and Rural Water Management,
Department of Water - Atmosphere - Environment,
University of Natural Resources and Life Sciences, Vienna

by

KLUIBENSCHÄDL Florian

Supervisor: Ao.Univ.Prof. Dipl.-Ing. Dr.nat.techn. Andreas Klik
Co-supervisor: Dipl.Ing. Stefan Strohmeier

Vienna, June 2, 2014

Acknowledgements

It doesn't take much imagination to understand the special character of field studies abroad. Experiencing learning curves of various kinds is the logical consequence of leaving home for an extended stay overseas. What I have learned during this study is not bound to the field of my research. Personal and intellectual growth was enhanced by the challenging fieldwork in the Ethiopian highlands and the wonderful time I had during the whole stay there. Therefore, I would like to express my gratitude to all people and organisations, which supported and enabled this research.

I want to thank my supervisor Andreas Klik for his engagement with the partnering projects and for the freedom he allowed me during the project's evolution. I sincerely thank my co-supervisor Stefan Strohmeier for his unending support and Reinfried Mansberger for his critical feedback and help in the remote sensing domain.

Partnering organisations of the project "Unlocking the potential of rainfed agriculture in Ethiopia for improved rural livelihood" played a key role in enabling the fieldwork and the stay abroad in general. I am grateful for the assistance given by ARARI, the Gondar Agricultural Research Institute and ICARDA. I would particularly like to thank Wondimu Bayu (ARARI) and Feras Zidat (ICARDA) for their advice and support. I received generous help from all the staff at my temporary office (GARC). I want to convey my deepest gratitude to Baye Ayalew and Muuz Gebretsadik whose help in the field, at the office and in social situations was indispensable. I would also like to express my gratitude to the Austrian Development Agency for their financial support of the partnering project.

I truly appreciated the illuminating discussions and the exciting moments I shared with my fellow students Christoph, Claire and Ingrid. They also know best how grateful I am for all the support, hospitality and tolerance the local community at the Aba Kaloye and the Ayaye watershed showed towards us.

Finally I would like to thank my loved ones, my family and friends who gave me support throughout my studies. I especially appreciated the encouragement from and motivating discussions with my flatmates and close friend Christoph. I want to thank Molly for her continuing emotional support and her precious help with the subtleties of the English language.

Abstract

Erosion processes in the Ethiopian Highlands manifest in various ways. Gullying can add significantly to negative on- and off site effects, thus knowing the severity of different erosion processes is crucial for sound decision making. This study focuses on the assessment of gully erosion in the Aba Kaloye case study catchment near Gondar, Ethiopia. It evaluates the total soil loss within three gully sections and tests the applicability of close range photogrammetry for rapid gully growth data acquisition.

Fieldwork for this study took place between June 17^{th} and September 5^{th} 2012 in the small 36 ha Aba Kaloye catchment of the northern Amhara tropical highland region. One aim, the method analysis, was to compare the ground based close range photogrammetric and the manual plumb line gully surveying approaches. The assessment of soil loss rates attributable to gullying in the case study catchment was the second goal. This part of the study is based on data acquired with the manual tape measurement technique.

Experiences with the CRP measurement approach may alleviate the provision of calibration and validation data for modeling purposes in general. Providing insights into temporally and spatially high resolving gully surface models, the method could also contribute to future gully erosion model development. The study outlines experiences gathered during fieldwork and the analysis process of the terrestrial close range photogrammetric approach. For ten channel cross-sections, the study evaluates a method-consistency variable: Coordinate elevation residues between the methods are found to lie within the range of a few centimeters.

The soil loss at three reaches of the channel network are 12.32, 7.78 and $9.40m^3$ and they occur within a total investigated gully length of approximately $47m$. The estimated total gully erosion share lies between 5.8 and 18% of the catchments total sediment freight occurring between June 27^{th} and August 8^{th} 2012.

Zusammenfassung

Aufgrund klimatischer, topografischer sowie sozialer Bedingungen manifestieren sich in Äthiopiens tropischen Hochlandregionen unzählige Bodenerosionserscheinungen durch Wasser. Die vorliegende Arbeit beleuchtet das Phänomen der Gullyerosion und bedient sich dazu zweier Methoden zur geometrischen Abbildung ephemerer Gerinne. Die Datenerhebung mittels Maßband-Lotmessung sowie photogrammetrischer Aufnahme wurde zwischen 17. Juni und 5. September 2012 in einem 36 ha großen Einzugsgebiet nahe Gondar (Amhara-Region) in Äthiopien durchgeführt.

Ein Ziel der Studie war die Erarbeitung eines Arbeitsablaufes zur Oberflächenmodellierung von Erosionsgräben mittels kostengünstiger, bodengestützter Nahbereichsphotogrammetrie. Eine Gegenüberstellung der Resulate beider Methoden ermöglicht zwar keine qualitativen Aussagen zur Genauigkeit des photogrammetrischen Ansatzes, jedoch verdeutlicht sie die Stärken und Schwächen dieser Technik sowie die Fehler und Schwierigkeiten die bei Aufnahme und Auswertung gegebener Oberflächengeometrien auftreten können. Die mittlere quadratische Abweichung (RMSE) der Höhenwerte von Gullyprofilkoordinaten beider Oberflächenmodelle erlauben eine qualitative Aussagen zur Übereinstimmung der Methoden.

Außerdem wird mit den erhobenen Daten eine Abschätzung jenes Anteils der erodierten Sedimentfracht durchgeführt, welcher der Erosion in Gullies zuzurechnen ist. Diese Berechnung, ebenso wie eine Beschreibung der zeitlichen Entwicklung von Erosionsgräben, basiert auf dem Vergleich der Bodenoberflächen dreier Untersuchungsabschnitte zu unterschiedlichen Zeitpunkten. Datengrundlage hierfür ist die Messung von insgesamt 18 Gullyquerschnitten mittels Lotmessungen. Gemeinsam umfassen die untersuchten Gullyabschnitte eine Länge von etwa 47 m. Die Volumszunahme beläuft sich auf 12.32, 7.78 und 9.40 m^3 für den Zeitraum zwischen 27. Juni und 05. September 20012. Für den kürzeren Zeitraum vom 27. Juni bis 8. August 2012 liegen außerdem Daten zu Niederschlag, Abfluss und Sedimentfracht beim Gebietsauslass vor. Für diesen Zeitraum beschreibt die vorliegende Studie hypothetische Szenarios, welche auf einen 5.8 bis 18 prozentigen Anteil der Gullyerosion an der gesamten Sedimentfracht schließen lassen.

Contents

List of Abbreviations	
Abbreviation	Description
CCD	Charged-Coupled Device: The image sensor format of the camera harware this study uses
CP	Check Point
CRP	Close-Range Photogrammetry
CS1, CS2, .., CS24	Cross-Section: Except CS24 they are in nubered ascending starting at the top of a gully reach.
DSM	Dense Surface Model: A point cloud resulting from the DSM-generation process in the software PhotoModeler Scanner
G1, G2, G3, G4	Gully reaches under investigation. G4 further devides into a southern (G4.1) and a northern branch (G4.2)
GCP	Ground Control Point
m a.s.l	Meter Above Sea Level
NPD	Nick-point distance: The distance between the topmost cross-section and the head incision of the gully under investigation
PCL	Point Cloud Size: The number of points in a Dense Surface Model
PL	Plumb-Line: referring to the method of plumb line surveying of cross-sections
PM	PhotoModeler Scanner: An EOS Systems Inc. Photogrammetry software
PP	Pass Point (see GCP)
Q1, Q3	The lower (25%) and upper (75%) quartile of a data
RMS/RMSE	Root Mean Square Error
S1, S2, S3	Field sessions where the measurements and image recording took place.
TGEL	Thinning Grid Edge Length: A parameter describing the cell size in the LASTools software suite thinning algorithm
TIN	Triangulated Irregular Network: A vector based surface representation format

1 Introduction and Objectives

Particles forming the sediment load at the outlet of a catchment or river basin differ in origin and are — theoretically — also distinguishable by the factors leading to their creation. Irrespective to the origin, these particles induce manifold downstream problems, above all environmental and economic costs. Regardless of whether or not downstream or off-site costs outweigh the negative economic on-site effects of soil erosion, they usually justify conservation efforts to some extent [Morgan 2005, pp. 1-3].

Pimentel et al. [1995] conclude for the US territory that each $1 invested in soil conservation efforts, would result in savings of $5.24. Hence, reaching a broad social consensus about the benefits of conservation is a matter of time, but selecting sound conservation measures requires profound knowledge of the prevailing situation [Morgan 2005, cap. 7].

Hydrological (erosion) models are a common tool in soil conservation planning, they are used for soil loss prediction (where and when) and assessment, and even to gain a better understanding of erosion process interactions. The popularity of erosion models provides for two reasons to deal with gully erosion research practices.

First, there is the need to calibrate models. Irrespective to their type (empirical, physically based conceptual), it is desirable to calibrate a model in order to improve results [Jetten, Roo, and Favis-Mortlock 1999]. At the watershed scale — a scale quite important at the policy and decision making level — calibrating parameters for channel processes, and therefore gully erosion data is of interest for certain modelling approaches (e.g. [Fox and Papanicolaou 2008]).

Current models incorporate channel process components at a very coarse level only. As a result, parameters needing calibration in this sector are few. This fact leads to the second argument for a revival of gully research with state of the art methods: Increasing model complexity does not necessarily correspond to soil erosion prediction quality. However, future models will aim do a better job in physically modelling gully erosion processes [Merritt, Letcher, and Jakeman 2003, p. 792; Morgan and Nearing 2011, p. 392]. Hence, documenting gully development in a temporal resolution of single events and a spatial resolution which covers small scale gully features can provide useful information for the model component design.

On a collaborative basis within the international project "Unlocking the potential of rainfed agriculture in Ethiopia for improved rural livelihoods" (ICARDA, ARARI, EIAR, Sasakawa-Global-2000, BOKU), field investigations on the gully development in the small Aba Kaloye catchment near lake Tana, the northern Amhara region of Ethiopia, took place in the Summer 2012. Various erosion processes are visible in the 36 ha small case study catchment. While all of these processes are viewed as a threat to farming

efforts, this study investigates the loss of arable soil due to gullying. The assessment focuses on four distinct gully sections which clearly show active erosion phenomenons and which are part of the catchments ephemeral channel network.

Overlapping ground based photographs, taken with a non-metric digital camera were taken as input data for a detailed photogrammetric analysis. Using the resulting high resolution surface models, one goal of the study was to assess the applicability of this remote sensing method in the given domain.

In order to provide comparison and backup data, as well as for verification purposes, the field work was designed to incorporate manual plumb line and tape cross-section (CS) measurements as well. This method uses an approximately horizontal reference string and number of vertical depth measurements between string and soil surface to describe and quantify a CS area.

After reviewing and working with the photogrammetric data it turned out that, under the given circumstances of the study (planned workload and the image acquisition strategy), it is not feasible to provide an adequate case study assessment (gully erosion rates at certain points in the Aba Kaloye catchment) based on this approach. However, since both methods were applied at the beginning, middle and end of the rainy season it was possible to elaborate gully erosion rates for the case study on the basis of plumb line measurements.

The fieldwork used geo-referenced buried stones to retrace the location of 24 CSs at four gully reaches. These markers were also necessary to add a consistent outer orientation to the dense surface point clouds resulting from photogrammetric analysis. Amongst all markers are control points which, excluded from the photogrammetric reconstruction process, provide a subsequent error estimation database. The software package PhotoModeler (PM) Scanner® was used to derive surface models from the point clouds. Comparing the surfaces from different points in time for a specific gully reach reveals volumetric soil loss for the area.

Independent of the gully volume evaluation, one aim of this work is the elaboration of a feasible work-flow for the assessment of (ephemeral) gully erosion based on close range photogrammetry. This should alleviate the provision of calibration and validation data for modelling purposes and contribute to future gully erosion model development. Within the framework of the case study the method is applied and an erosion volume is derived for one specific gully reach within the catchment.

2 Gully Erosion Research

A global population, still growing, faces agricultural challenges of different kinds. In some regions, soil deterioration is currently one of the biggest threats to agricultural productivity. As an umbrella term, soil erosion incorporates manifold phenomena. Often these phenomena have prevailed for millennia forming an (ecological) equilibrium, however more and more they are regionally affected by mankind.

Nyssen et al. [2004, pp. 288 sqq.] specify erosive rains and steep slopes as two natural drivers. Deforestation, farming systems and the stagnation of agricultural techniques are anthropogenic catalysts for soil erosion and degradation in the Ethiopian highlands. By presenting values between 166.6 and 543.7 $J\ cm\ m^{-2}\ h^{-1}\ year^{-}1$ for the Universal Soil Loss Equation (USLE) erosivity index R, Krauer [1988] lists reasons for spatially comprehensive sheet erosion processes almost everywhere in Ethiopia (compare figure 9). Intense rainfalls, missing interception and sloping surfaces amongst other factors potentially lead to (channelled) surface runoff and — due to the resulting shear stress on the soil surface — the development of erosion rills and larger incisions especially in the highland regions [Zachar 1982, pp. 328 sqq.; Nyssen et al. 2004, p. 288].

With respect to gully erosion, negative impacts are not limited to the loss of soil and arable land. Enhanced drainage or the change of local groundwater bodies at several scales are critical developments in some regions where plant water availability is precarious. Off-site effects result, for example, from increasing connectivity at the watershed scale. Depending on the context, further negative impacts are the transportation of pollutants and nutrients or the siltation of surface water bodies [Nyssen et al. 2004; Valentin, Poesen, and Li 2005].

Development of erosion gullies, and therefore their share in total erosion rates clearly depends on environmental controls such as soil type, topography, climatic conditions and, for examole, on land use as one of the most pressing human impact factors [Valentin, Poesen, and Li 2005]. Also, gully morphology and temporal progress of gullying is diverse. As a result, detailed temporal and spatial observations are necessary to link spatial and temporal variables with environmental controls.

2.1 Classification

Erosion phenomena occur globally. As a result, terminology differs between regions and languages. Zachar [1982] gives an overview of international terms describing water erosion and classification systems. Gully erosion, as a type of water erosion, is profoundly different to any form of areal erosion. It is a top level class on its own in the majority of classification systems. The term has a broad meaning, it incorporates several forms of linear erosion and it

Figure (1) Gully 1 head at research session one and session two.

does not per se specify whether benignant or malignant erosion occurs. The latter of these terms describes higher, the former lower, total soil loss than soil formation rates. Morgan describes gullies as,

> relatively permanent steep-sided water courses that experience ephemeral flows during rainstorms. Compared with stable river channels, which have a relatively smooth, concave-upwards long profile, gullies are characterised by a headcut and various steps or knick points along their course. ... Gullies also have a relatively greater depth and smaller width than stable channels, carry larger sediment loads and display very erratic behaviour, so that relationships between sediment discharge and runoff are frequently poor [Morgan 2005, p. 30].

The form of gully cross-sections (CS) is one of the most apparent properties for classification. Zachar [1982] lists broad, narrow, flat and round gullies and associates the vertical and lateral erosion with narrow V-shaped and broader U-shaped gullies respectively. Another erosion process related to a distinct form of gullies is backward, retrograde or headcut-erosion. Here, waterfall erosion prevails due to an abrupt and significant incision at the top end of gullies. Figure 1 shows the result of the plunge-pool effect, a phenomenon leading to a quick upwards moving and lateral expanding head incision [Bocco 1991].

Litereature indicates classification thresholds between erosion rills and gullies. As an example, gullies have a minimum depth of 0.5 m according to the Soil Science Society of America [2008]. However, ephemeral gullies are incisions at concentrated flow paths whose size or depth can be less than these threshold. In contrast to permanent gullies, ephemeral gullies do not obstruct normal tilling activities. They vanish through such operations just

to reoccur after some additional runoff events. This definition undermines the common approach to differentiate water erosion phenomena by physical erosion mechanisms. No clear distinction between rill and ephemeral gully erosion exists. At the upper end of the scale it is a difficult (and at least to a certain extent subjective) challenge to find the boundary between large gullies and river channels [Morgan and Nearing 2011, p. 361]. Figure 44a illustrates an example of the latter while one research site in this study, namely the top parts of G4, feature a continuous transition from rill to gully erosion (see figure 43).

2.2 (Gully) Erosion Investigation Techniques

Effects of gully erosion as well as the reasons for the phenomenon are manifold. Gully growth expressed as volumetric changes within a certain time period are one indicator that gully erosion research tries to assess. Additionally, gully densities within a certain area, gully length development, longitudinal and transversal cross-section changes and the dependency of these attributes on the environment are of interest [Zachar 1982, 145f.].

2.2.1 Direct and Indirect Field Methods

Corresponding to the variable appearance of gully erosion processes, a wide variety of measurement techniques exist. Amongst them, photogrammetric methods are not what one would call a recent development. Aerial photography has been used in the investigation of control measures since 1935 and ground level stereophotogrammetry was subjected to scientific research in the early 1970's [Zachar 1982, p. 189]. Technological developments, especially the introduction of digital cameras in combination with improved soft- and affordable hardware, are the driving forces for a revival of scientific interest in this method in the recent past. Still, many studies focus on aerial photogrammetry (see 3.2), but depending on the scale of the research area, ground based approaches are an economic and fast tool to do the job.

Direct measurement tools like profilometer, single rod or measurement tape can provide detailed gully geometries, but as soon as three-dimensional data is the aim of a study, these approaches limit either the spatial resolution or a domain's extent. Some indirect measurements (e.g. remote sensing or detailed maps) can overcome these limitations at the cost of a reduced range of application and often higher expenditures. Other indirect measurements such as fingerprinting approaches try to distinguish sediment sources without any interest in specific gully features [see e.g. Krause et al. 2003].

2.2.2 Erosion Modeling

Since sophisticated (complex, distributed) models have come into use to evaluate (long term) soil loss and to assess protective measures, distinguishing

between the different erosion types has become more important.
In 1991, Bocco stressed that a physical formulation, capable of modelling gully growth does not yet exist. He therefore states, that a purely statistical approach is tolerable [Bocco 1991]. In the field of gully modelling, Morgan and Nearing [2011, 368ff.] distinguish three different purposes: (i) To evaluate time and location of the occurence of ephemeral and permanent gullies, (ii) to model soil losses in such features and (iii) to compute gully headcur retreat. In fact, any approach they list in either of these classes incorporates empirical relationships of variables and environmental parameters.

Only few established erosion models implement the second of the three mentioned ideas [Nachtergaele and Poesen 1999, p. 694], and while distributed models necessarily cover (detachment and) transportation processes in routing channels, the question is if and how to deal with the potentially dynamic behaviour, for example a longitudinal growth of these waterways.

According to Poesen et al. [2003] gully erosion accounts for a minimum of 5% up to a maximum of 90% of the total soil loss in a catchment. Considering this variability, one might even question the validity of state of the art watershed modelling attempts. Currently no model integrates the full range of geomorphological processes [Morgan and Nearing 2011, p. 19]. However, it is the author's opinion that the establishment of rapid and high resolving data acquisition techniques can potentially contribute to the improvement of future modelling approaches. For now, an increasing availability of gully erosion rates might help to parametrise, calibrate and validate existing erosion models [see e.g. Haregeweyn et al. 2013].

3 Remote Sensing and Soil Erosion Research

Various remote sensing technologies and methods are potentially well suited to the task of erosion research. Aerial photographs, satellite images and all their secondary products are without a doubt an essential input when it comes to creating medium to large scale erosion models. Additional input for such models and for a variety of other soil science applications, can be sourced e.g. from spectral reflectance, radar or lidar (radio or light detection and ranging)[Schmugge et al. 2002; Anderson and Croft 2009].

King et al. examine a list of variables which, a) affect hydrological systems and are b) accessible via remote sensing. They show the use of empirical relationships to provide for these variables in runoff and erosion models and therefore focus their research on data gained from aerial photos, radar and satellite. These data sources allow for the assessment of variables, often indirectly related to the runoff and sediment formation. Land use, plant (residue) cover and surface roughness are only a few examples of such independent factors in erosion models.

When it comes to variables affecting runoff and sediment transfer functions, digital elevation maps are the most prominent product derived from satellite imagery, aerial photos and — if a comparatively low vertical resolution is acceptable — radar images and synthetic aperture radar (SAR) interferometry [King et al. 2005b; King et al. 2005a; *An Overview of SAR Interferometry*]. With respect to the optical measurement and monitoring of rills and gullies, King et al. stress that the geometry of such features is easily recognisable, but also point out difficulties of automation. Incisions appear like linear traces in high resolution satellite images or in aerial photos taken from high altitudes. Deriving routing networks is a task studied by many authors over the past few decades. Examples and further information on the topic are available from: Gardner, Connors, and Hu [1989]; Ottlé, Vidal-Madjar, and Girard [1989]; Hughes, McDowell, and Marcus [2006]; Bartley et al. [2008]; Nardi, Campo, and Rinaldi [2013].

A rather narrow understanding of the term remote sensing limits the spatial scales of applications, as observation systems are based on satellites or airplanes. Widening the definition to terrestrial and surface-adjacent observation platforms underpins the importance of remote sensing in the field of erosion research.

At spatial scales below several hundred meters, remote sensing techniques make use of the same physical principles as distance techniques. Nevertheless, it is sometimes necessary to utilize different approaches when measuring the same properties at different scales. For example, when assessing the surface roughness of bare soils at plot or watershed scale, it is possible to discern tillage related properties (amongst others) from a combination of optical and

SAR imagery [Moran et al. 2002; Baghdadi et al. 2002]. At smaller scales, close range photogrammetric (CRP) data enables the examination of tillage results or micro scale ($<$ 10 cm) surface roughness to be studied accurately and economically.

Warner [1995] for example, used a 35 mm analogue non metric camera to capture photos from a step ladder above ploughed soil. With a low cost system he achieved empirical accuracies of 1.2, 1.8 and 2.1 mm in X, Y (the image plane) and Z direction respectively. Studies with comparable shooting distances, for example Jester and Klik [2005] or Taconet and Ciarletti [2007], report similar resolutions of less than 5 mm for height measurements. However, studies using this technology in the field of soil science do not agree on the need for expert knowledge for photogrammetric analysis. This reflects that the extent of experience necessary for applying CRP techniques depends on the research object. However, modern hardware and advances in the analytical evaluation algorithms reduce the number of steps in the CRP work flow (see Figure 3). Also, an ever growing number of scientific, industrial and service CRP applications [Luhmann 2002, pp. 15-18] suggests a decreasing necessity for photogrammetric expert knowledge. Furthermore, compared to laser scanning technology, ground based as well as aerial based CRP have the benefit of relatively low costs.

3.1 Photogrammetry - Basics and Applications

Photogrammetry is based on the processing of one or more images in order to measure form and location, as well as to describe and interpret the appearance of real-world objects. The following sub-sections describe basic principles, the assets and drawbacks and the particular properties of CRP, a sub-branch of the photogrammetric remote sensing technique, which is of special interest for this study.

3.1.1 Definition and Applications

The historical development of photogrammetry spans more than a century [Linder 2003, Preface; Luhmann 2002, pp. 18-25] [Albertz 2007]. It is therefore not surprising that numerous definitions exist, originating either from different centuries or scientific fields. At the Kyoto congress of the International Society for Photogrammetry and Remote Sensing (ISPRS) in 1988, Photogrammety and Remote Sensing were not decoupled from each other and defined as,

> the art, science, and technology of obtaining reliable information about physical objects the environment through the process of recording, measuring and interpreting imagery and digital representation thereof derived from non-contact sensor systems.

An American Society for Photogrammetry and Remote Sensing publication defines photogrammetry very similarly as,

> the art, science,change folder of latex automatical compilation files and technology of obtaining reliable information about physical objects and the environment through processes of recording, measuring, and interpreting photographic images and patterns of electromagnetic radiant energy and other phenomena [American Society for Photogrammetry and Remote Sensing 2004].

As a result of the long term development of photogrammetry and its diverging fields of application, a vast amount of different recording sensors, measuring and interpretation devices exist. Geodesy is a traditional field of application, in which aerial photos serve as input data for photogrammetric analysis. Here, measurement results are present only after an analysis process, which is (temporally) separated from the image recording (offline-photogrammetry). It is therefore possible to take the pictures sequentially with the same recording device. This is the approach of choice in many other fields, especially where rather small camera-to-object distances from a few centimetres up to some hundred meters prevail (CRP). Examples are:

- Automobile, machine and ship maufacturing
- Architecture, city planning, archaeology
- Structural engineering (deformation measurement of structural buildings, mining, etc.)
- Medicine
- Several disciplines in the natural sciences (fluid mechanics, material sciences, soil science, etc.)

Some of the above-mentioned fields, as well as other industrial applications (robotics - machine vision), require immediate results. Online-systems therefore use two or more image sensors, which simultaneously record the scene of interest [Luhmann 2002, pp. 15-18].

3.1.2 Technical and Mathematical Background

Measuring physical objects from images (as the definitions suggest is the main task of photogrammetry) is possible from only one photo. Of course, from a two dimensional image pane, only two dimensional information is available. The majority of applications certainly aim to gain three-dimensional object descriptions. This is possible by applying the principles of stereoscopic viewing to a photo-pair whose elements cover the same scene and have slightly different exposure positions. Most branches of this technique

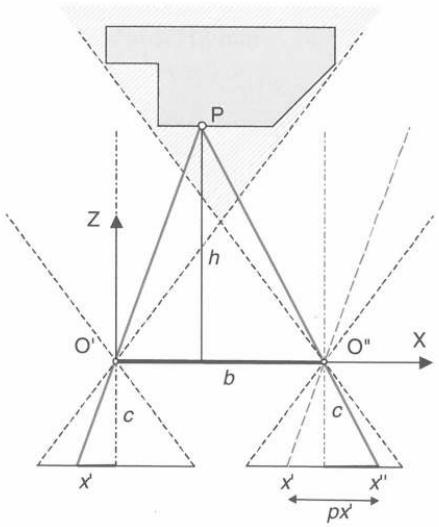

Figure (2) Standard case of stereoscopy: image planes are coplanar and show an offset in X-direction only (Source: Luhmann [2002, p. 321])

usually utilize more than two photos to cover either a larger extent, or to incorporate multiple perspectives and thereby avoid shading effects (compare section 3.1.3). Figure 2 depicts the basic case of deriving the depth information from two homologous image rays intersecting at object point P.

Defining the origin of a three-dimensional Cartesian coordinate system in the left projection center leads the following equations to compute object coordinates by measuring image coordinates x' and y', as well as the the x-parallax px':

$$X = \frac{h}{c} \times x' = m_b \times x' \qquad Y = \frac{h}{c} \times y' = m_b \times y' \tag{1}$$

and in the direction perpendicular to the image plane

$$Z = h = \frac{b \times c}{x' - x''} = \frac{b \times c}{px'} \tag{2}$$

Figure 2 also incorporates the concept of central perspective where all rays of light travel from the object through one single point, the projection center O' or O''. Despite the fact that lenses and cameras do not accurately represent this model, the geometrical relations of the focal length c, the recording distance h and the basis b form the basis of photogrammetric analysis.

Whether the image source is a digital or analogue camera has a rather large impact on the photogrammetric operational process (see figure 3). Further-

more, the field of application, the necessary measurement resolution and the accuracy in object space affect research decisions related to hardware, e.g. whether non-metric cameras and commercial lenses can provide acceptable data for the subsequent analysis [Linder 2003, p. 3].

On the software side, (commercial) state of the art implementations cover most parts of the analysis process figure 3 depicts. Unfortunately most photogrammetric workstations (software packages) do not reveal much of the approaches they use to

- calibrate cameras,
- do the exterior (relative) orientation mathematics,
- reconstruct objects and point-clouds from oriented images,
- or to detect features.

Coordinate (feature) modelling and the measurement of homologous points representing these coordinates is possible by solving collinearity equation systems as part of spatial resection, intersection and/or bundle adjustment methods. Geometric properties of the recoding system (=interior orientation, IO) and the orientation of images in object space (=exterior orientation, EO) provide for the parameters of these equation systems. IO and EO parameters are themselves derived from features (tie points, GCPs), detected either manually or automatized in the photographs [Luhmann 2002, pp. 119, 234, 428 sqq.]. Information passes through the photogrammetric process in the form of photons, chemical structures and electronic signals. The analytical processing of this information requires the definition of coordinate systems for the object space, at the image pane and for the photogrametric models. Transformation approaches are necessary to translate coordinates in between these systems. Luhmann [2002, pp. 29-50] provides a set of transformation equations for the planar and three-dimensional space. Another section of his textbook [pp. 50-74] summarises fitting approaches necessary for overdetermined equation systems, a challenge in photogramtric science.

Photo control: Several tasks of the photogrametric process depend on the recognition and definition of coordinates in the source images. It is necessary to define identical (homologous) features, common to adjacent images of stereoscopic models. Depending on whether knowledge on the object space coordinates of such a point exist, it is possible to distinguish tie points (TP) and ground control points (GCP) [Mather 1999, p. 71].
TPs allow for the measurement of their image coordinates in two or more images which subsequently leads to the (relative) EO (Figure 6a) of images (see 3.1.2). It is even possible to infer interior orientation parameters if the number of measurements exceeds four TPs.

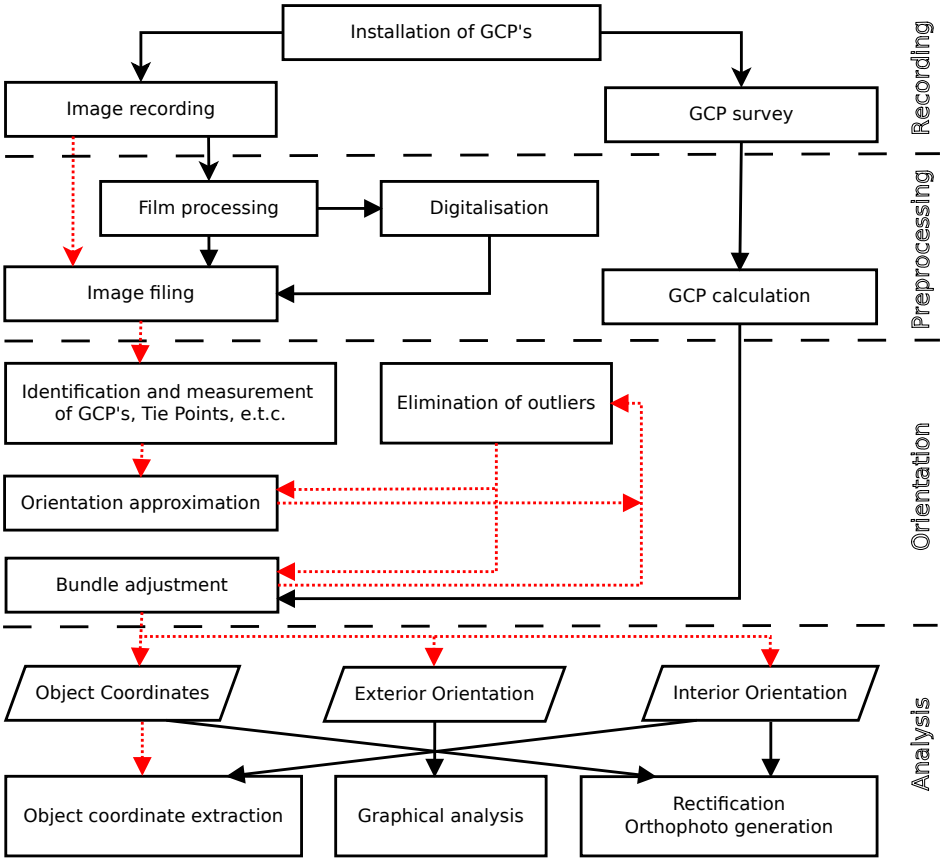

Figure (3) Operational procedure for image acquisition and analysis (red: automatable when using digital systems) (Source: modified after Luhmann [2002, p. 12])

Knowledge of the location of reference points in a superordinate Cartesian coordinate system is essential, as it assists the transformation between model and object space. Image coordinate measurements and the determination of object space coordinates of at least tree GCPs allows for the establishment of the absolute orientation (Figure 6b) of images or the stereoscopic model they represent.

The term *pass point* is a literal translation of the German word Passpunkt, which in German has the same meaning as GCP. Unfortunately this results in confusion with German speakers: In English-speaking areas a pass point simply describes a feature, common to conjugate images of a model. The term GCP, which, in the authors opinion, implies to a certain degree that it is observed from above the ground, e.g. from an air plane, drone or satellite, is used in the prevailing ground based application of CRP for the sake consistent terminology.

Another distinction between GCP's used to orientate the model (reference points - RP) and the ones available for validation and error estimation

(check point - CP) is possible. Further names such as control point, ground or photo control, tie strip or connection point are used to name GCPs and TP's in the relevant literature [Newby 2012, p. 378; Chandler 1999, pp. 53-54; Linder 2003, p. 65].

Interior and Exterior Orientation: The interior orientation defines a) the relative position of the projection center to the image pane and b) the distortion parameters. Figure 4a shows the principal point (H') and principal distance (c or f') parameters which describe the orientation. A radial-symmetric, often polynomial, function (3) incorporates the distortion parameters. Figure 4b illustrates the most significant (radial) distortion effects, a typical feature of all lenses. [Luhmann 2002, 118ff]

$$\Delta r'_{rad} = A_1 \times r'^3 + A_2 \times r'^5 + A_3 \times r'^7 + ... \tag{3}$$

Additional distortion parameters are necessary to consider asymmetric and de-centering lens distortion effects (4) whose magnitudes usually depend on the quality of the lens.

$$\begin{aligned} \Delta x'_{tan} &= B_1 \times (r'^2 + 2x'^2) + 2B_2 \times x' \times y' \\ \Delta y'_{tan} &= B_1 \times (r'^2 + 2y'^2) + 2B_2 \times x' \times y' \end{aligned} \tag{4}$$

Assessing the EO of images, their spatial position ($X_0Y_0Z_0$) and direction ($R(\omega\phi\kappa)$), is another part of the analysis process. Providers of aerial surveying products potentially include these parameters in the image delivery, although calculating it is part of each modern software product as well. A mathematical analysis implements, similar to many other tasks in photogrammetry, the model of central perspective to describe the relationship between image coordinates ($x'y'$) and the corresponding object space coordinates (XYZ). Figure 5 shows how the vector sum of X_0 pointing at the projection center O' and X^* originating in O' results in the object coordinate X. Equation (5) expresses this relation mathematically.

$$X = X_0 + X^* \tag{5}$$

$$X^* = m \times R \times x' \tag{6}$$

Vector X^* is unknown and declared in the superordinate coordinate system as X or X_0. It is expedient to express this with equation (6), where x' is the image vector (with $z = -c$), R is the rotation matrix and m is a scaling factor. Substituting X^* with (6) resolves to (7).

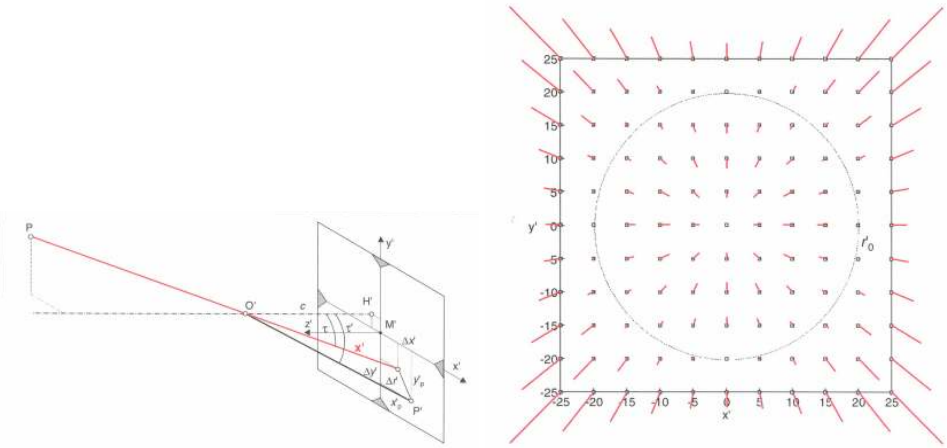

(a) Interior orientation (Source: Luhmann [2002, p. 119], modified)

(b) Radial symmetric distortion effects (Source: Luhmann [2002, p. 122])

Figure (4) $\Delta x'$ and $\Delta y'$ in 4a represent the distortion effects visible in 4b. The principal distance, or camera constant c, is actually not constant since it depends on the focus. In most applications the focus is set to infinity where the principal approximates to the focal distance: $c \approx f'$

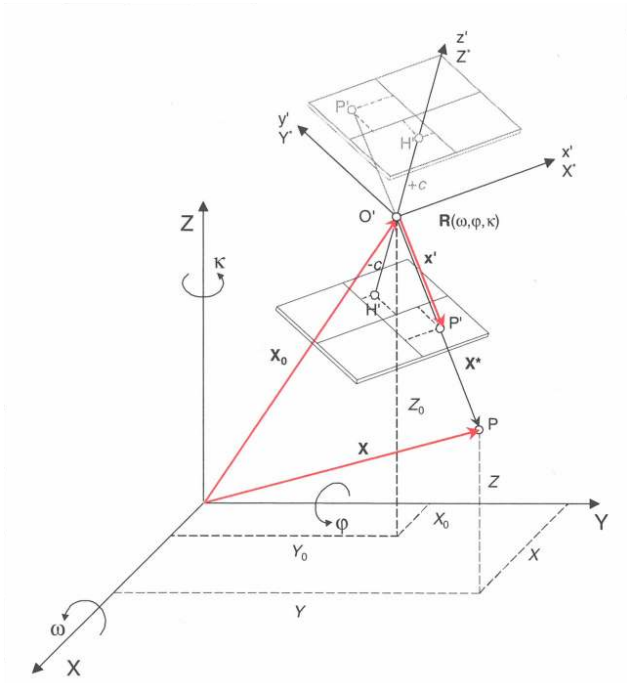

Figure (5) Exterior Orientation and central projection (Source: Luhmann [2002, p. 252])

$$X = X_0 + m \times R \times x'$$

$$\begin{bmatrix} X \\ Y \\ Z \end{bmatrix} = \begin{bmatrix} X_0 \\ Y_0 \\ Z_0 \end{bmatrix} + m \times \begin{bmatrix} r_{11} & r_{12} & r_{13} \\ r_{21} & r_{22} & r_{23} \\ r_{31} & r_{32} & r_{33} \end{bmatrix} \times \begin{bmatrix} x' \\ y' \\ z' \end{bmatrix} \tag{7}$$

Reformulating and extending this equation system with the principial point $H'(x'_0, y'_0)$ and the distortion parameters $\Delta x'$ leads to equation (8).

$$x' - x'_0 - \Delta x' = \frac{1}{m} \times R^{-1} \times (X - X_0)$$

$$\begin{bmatrix} x' - x'_0 - \Delta x' \\ y' - y'_0 - \Delta x' \\ x' - x'_0 \end{bmatrix} = \frac{1}{m} \times \begin{bmatrix} r_{11} & r_{21} & r_{31} \\ r_{11} & r_{22} & r_{32} \\ r_{13} & r_{23} & r_{33} \end{bmatrix} \times \begin{bmatrix} X - X_0 \\ Y - Y_0 \\ Z - Z_0 \end{bmatrix} \tag{8}$$

Dividing the first two equations by equation three in (8) respectively, sheds the collinearity equations (9) so very fundamental in photogrammetry.

$$x' = x'_0 + z \times \frac{r_{11} \times (X - X_0) + r_{21} \times (Y - Y_0) + r_{31} \times (Z - Z_0)}{r_{13} \times (X - X_0) + r_{23} \times (Y - Y_0) + r_{33} \times (Z - Z_0)} + \Delta x'$$

$$y' = y'_0 + z \times \frac{r_{12} \times (X - X_0) + r_{22} \times (Y - Y_0) + r_{32} \times (Z - Z_0)}{r_{13} \times (X - X_0) + r_{23} \times (Y - Y_0) + r_{33} \times (Z - Z_0)} + \Delta y' \tag{9}$$

The fundamental equations of photogrammetry (9) form the basis of different methods to calculate orientation parameters, such as the spatial resection or the direct linear transformation (DLT) approach [Luhmann 2002, 239ff., 246ff.]. Since for a single image six unknown variables $(X_0, Y_0, Z_0, \omega, \phi, \kappa)$ exist, at least three GCPs must provide for X,Y and Z-vlaues in (9). Further applications relying on the collinearity equations are the relative positioning of a stereo image pair (see figure 6a) or the bundle adjustment (BA) method. These approaches yield the orientation of either two or multiple images in a model coordinate system (ralative orientation). A subsequent spatial similarity transformation requires at least three GCPs to put the resulting model in the object space (see figure 6b).

The two-step approach of first setting up a coherent image model and then transforming it into object space is traditionally called aerotriangulation or the aerial triangulation method. These terms connote air-born images

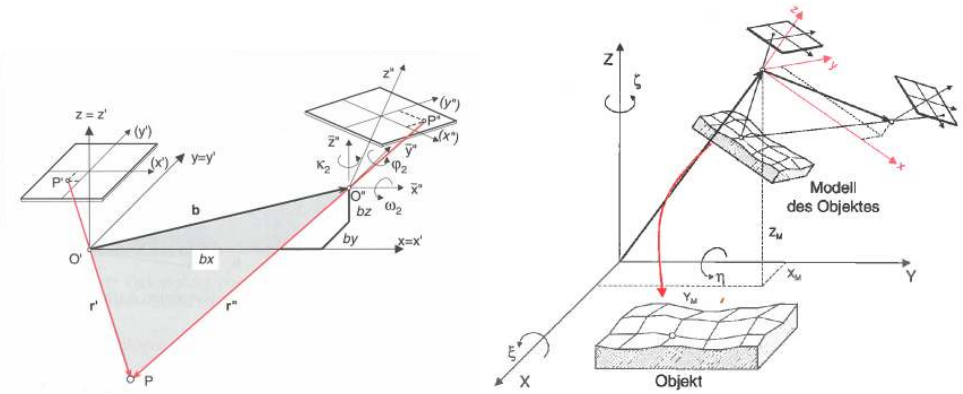

(a) Relative orientation (Source: Luhmann [2002, p. 252], modified)

(b) Absolute orientation (Source: Luhmann [2002, p. 264])

Figure (6)

and approximately parallel image panes and in fact BA algorithms considerably vary from these traditional techniques. The process of BA implements a simultaneous calculation of all unknown orientation parameters of an image set and its prevalence has been closely related to soaring computational power since the early 1980s [Luhmann 2002, pp. 249 sqq., 266 sqq.].

Some quality characteristics of GCPs — other than visibility and distinctiveness in the photos — depend on the approach to establish the photogrammetric model (EO). If the approach utilizes tie points to create a model in an arbitrary space (SfM see 3.1.3), providing GCPs distributed over the whole research area in order to be visible in each image is not mandatory. Nevertheless, while a good distribution within a image is necessary to provide a sturdy orientation of the image, a good GCP-distribution within a multi-image model provides for a sturdy absolute orientation of the model.

Camera Calibration: This term describes the evaluation of internal geometric properties for a recording device and, depending on the sensor system in use, for a certain image recording situation. Metric cameras do not feature focusable lens systems and are manufactured in a robust way, calibrating them is a one-time or rarely reoccurring job. In contrast, the measurement quality achievable with partially-metric cameras and especially off-the-shelf consumer camera systems, highly depends on the calibration either a) immediately before the image recording process, b) as part of the photogrammetric analysis (on-the-job) or c) particular for each single image (on-the-job with varying interior orientation). Especially in the field of CRP, situations occur where camera parameters change within one image set. The principal distance, for example, varies if re-focusing becomes necessary between the pictures [Luhmann 2002, pp. 133-125].

Luhmann [2002, 502ff.] distinguishes between three main calibration processes for which two are of practical relevance for CRP. Mathematical analysis of photographs form the basis of most calibration approaches such as the calibration with a target grid and simultaneous or self-calibration.

The target grid calibration approach involves a flat or three dimensional set-up of target points or lines. Knowing the relative position and lengths of these geometries, it is possible to assess the camera parameters e.g. with bundle adjustment algorithms. Since a physical separation between the calibration and image recording prevails, this approach is prone to errors resulting from changes in temperature or the camera configuration. If, for example, photo recording of the target point field and the actual object happens to be in a significantly different spatial scale, the camera-focus is different in the two recording sessions.

By putting a target field or pass points on top of the scenery of interest, it is potentially possible to integrate the calibration in the actual image recording and analysis. Such an on-the-job calibration reduces the aforementioned risks and is a common approach in the field of CRP. A continuation is to substitute the test field with tie-points and pass-points. The latter are inevitable to define the datum (origin and scale) of the object coordinate system.

Feature-Recognition and Matching: Calculating XYZ coordinates of an arbitrary object point is restricted to a previous recognition of the same point in at least two images. While manual recognition is feasible (but often not best practice) for a reasonable number of TPs and GCPs, it is the prominent advantage of photogrammetry to gather dense surface information about objects, and therefore requires the recognition of numerous points. Image matching, the process of connecting conjugate feature coordinates (representing homologous points) of image pairs comprises feature- and area based matching approaches. Using only the latter method is possible for specific photogrammetric cases (e.g. in abundance of orientation parameters), however a combination of both tasks is the state-of-the-art approach in CRP.

Feature based approaches: In feature based image registration, the automated evaluation of homologous points is a two-step process. The first step itself, the recognition and segmentation of features, is a hierarchical process consisting of a pixel-value-threshold and a pixel-connectivity analysis, the assessment of form and size of connected pixel ranges, and the storage of image coordinates where adequate features occur. Luhmann [2002, 432f.] provides a list of interest operators, algorithms which may indicate the existence of discernible pixel patterns (features) within local image windows.

Subsequent to the definition of feature coordinates (point representa-

tions), a matching step seeks feature-conjunction across images. However, the matching of individual features is not the only scope of matching algorithms. For the generation of dense surface models, a consistent detection of homologous image patterns is the goal in the field of image matching approaches. Especially in CRP, where complex deformations (different scales, distinct perspectives , etc.) prevail frequently between images, feature based methods are significantly advantageous compared to area based matching [Zitová and Flusser 2003].

Area-based methods: Area-based methods form a class of image matching methods, focusing not on the detectransformstion of features, but rather on the matching of them. A classical example for area-based matching utilizes the normalized cross-correlation coefficient σ_{fg} [Luhmann 2002, 413f.]. Tebourbi et al. [2000] give a lucid description of how correlation based approaches reach sub-pixel accuracy: These approaches fit a second order curve to the correlation values (10), which result from an integer based incremental shift of $n \times n$ pixel windows. Afterwards, they perform an analysis of the curve maximum and compute the disparity of the matching points.

$$\rho_{fg} = \frac{\sigma_{fg}}{\sigma_f \times \sigma_g} \tag{10}$$

with

$$\sigma_{fg} = \frac{\sum[(f_i - \bar{f})(g_i - \bar{g})]}{n}$$

$$\sigma_f = \sqrt{\frac{\sum[(f_i - \bar{f})^2}{n}} \qquad \sigma_g = \sqrt{\frac{\sum[(g_i - \bar{g})^2}{n}}$$

and

$\bar{f}, \bar{g}$: arithmetic grey values

n : number of pixels in the reference and search window

Of course, various alternatives to the presented area- and feature based matching approach have emerged over the past few decades [Brown 1992; Zitová and Flusser 2003]. Further it is no surprise that the whole field of multi-view-stereo algorithms — software logic which includes feature detection and matching in order to compute dense surface models — is complex and in rapid development. In addition to the daunting complexity of the field, end users barely obtain information about implementation specifications of commercial software. It is therefore a tedious task to follow the suggestions of Zitová and Flusser [2003] to choose and adjust the type of mapping functions (in the matching algorithm) 'according to a priori known information

about the acquisition process and expected image degradations'. Despite most software products providing a set of parameters in order to meet the image characteristics (resolution, texture, feature size), it is not assured that the photgrammetric workstation is able to deal with strong angles when it comes to the reconstruction of an object surface. PM Scanner®, for example, requires preferably parallel camera positions.

3.1.3 Structure from Motion - SfM

While Snavely, Seitz, and Szeliski [2008] associate the phrase 'structure from motion' with the elaboration of multiple relative image orientations by finding corresponding features(feature matching), Fonstad et al. [2013] call SfM a photogrammetric process — and technologies used in relation to this process — discriminable from classical photogrammetry. The two main differences concern a) the process section in figure 3 where GCPs are introduced and the collinearity equations (9) are solved and b) the type of image registration methods the process employs. In the frame of classical photogrametric analysis, the orientation of single images via GCPs is prior to solving collinearity equations. A model draws real world results from the combination of single oriented image pairs right away. In contrast, the SfM process first elaborates an arbitrary model using automatically matched tie points. Only in a second step it introduces real world coordinates to establish the absolute orientation as figure 6b depicts. This approach became possible when the early 2000s saw the development of advanced feature recognition and matching approaches (3.1.2). They aim to be invariant to different scales and are also tolerant to divergent orientations [Snavely, Seitz, and Szeliski 2008]. These new generation feature matching algorithms (the Scale Invariant Feature Transform SIFT [Lowe 2004] is one representative), are now part of many modern software implementations. In combination with self-calibration-capable bundle adjustment approaches, they allow a significant reduction of subtasks in the photogrammetric process.

SfM is of special interest for trial CRP (taking photos after the trial and error principle), as it is capable of processing a large number of differently scaled and oriented photos. This alleviates modelling of complex surface structures, where only multiple perspectives allow for a complete representation of the object. Gully morphology, especially at scales below a couple of meters, can feature structures where it is necessary to deviate from a well ordered recording path.

3.2 Photogrammetry as a Gully Investigation Technique

Section 2.2 covers reach scale gully erosion measurement techniques including few direct approaches, lidar, aerial photogrammetry and the close range

remote sensing counterparts. Amongst these methods, terrestrial based CRP is rather uncommon, whereas for the other approaches several studies exist.

Nachtergaele and Poesen [1999] for instance, used aerial stereoscopic viewing to extract lengths of ephemeral gullies without demanding height measurements. Daba, Rieger, and Strauss [2003] took historic stereo-photos to evaluate the change of gully volume over a 30-year time period. They achieved a R^2 of .65 and .71 when comparing depth and width measurements from the field with a photogrametrically sourced digital elevation model (DEM). They report a consistent overestimation of gully depth measured from aerial photos and point to the problematic applicability of large scale imagery. While the assessment of volumetric soil losses from major gullies at basin or catchment scale seems feasible using aerial based photogrammetry, studies focusing on the shape or volume of small and medium sized gullies usually rely on other data sources.

In their comparative study on the accuracy of different field methods for gully erosion measurement, Castillo et al. [2012] stress the establishment of unmanned aerial platforms such as blimps, kites, helicopters or quadrocopters in gully erosion research [e.g. Marzolff and Poesen 2009; Giménez et al. 2009; Niethammer et al. 2012; Fonstad et al. 2013]. Equipped with imagery sensors, such unmanned aerial vehicles (UAV's) can overcome the limited spatial resolution of high altitude digital photogrammetry. A drawback of auto-piloted UAV-solutions is the rather expensive navigation system. On the other hand, radio controlled systems add the need for experienced pilots [Niethammer et al. 2012].

4 Material and Methods

4.1 The Context of the Case Study

Applying the CRP method in a case study environment adds first hand knowledge on the strengths and weaknesses of this approach. The prevailing context drastically differs from classical photogrammetric fields of application. It confronts the surveyor with various concerns. The importance of each concern (e.g. spatial or temporal resolution, relative image orientation, etc.) might be similar or diametric in different utilisation of the same method. This is especially true for on-site data acquisition which in the prevailing case mainly depends on the accessibility of recording positions.

The context of the case study also raises the question of the scalability of aforementioned measurement approaches and their results for further use in watershed scale models. But the area under investigation as well as adjacent regions serve as case study subjects for various other research projects and the prevalence of measurement infrastructure for hydrological variables indicates the catchment's special character within the Gumara-Maksegnit watershed. With the superior watershed being focus of further research, this study on gully erosion has the potential to contribute to a set of measurement variables and therefore to the understanding and modelling of hydrological processes in the whole region.

4.1.1 Gumara-Maksegnit Watershed and Sub-Catchments

The study's research sites for three dimensional gully investigation lie within the 36 ha small Aba Kaloye sub-catchment of the Gumara Maksegnit watershed (see figure 7). Other research takes place in this area, mainly coordinated through projects of the International Center for Agricultural Research in the Dry Areas (ICARDA), or of national institutions, such as the Amhara Regional Agricultural Research Institute (ARARI) and the Gondar Agricultural Research Institute (GARC). The Gumara Maksegnit watershed is subject to an integrated water management research project which focuses on rainwater conservation and horticultural applications. The study presented here uses hydrological and geomorphological datasets either gathered in collaboration with (or for) the project "Unlocking the potential of rainfed agriculture in Ethiopia for improved rural livelihoods" [*Unlocking the potential of rainfed agriculture in Ethiopia for improved rural livelihoods Ongoing Research*].

The Gumara river drains into Ethiopia's biggest lake and it is one of four larger tributaries to the Lake Tana. The basin is situated in the northwestern region of the Ethiopian highlands. These highlands are also known as the water tower of northern and eastern African countries, a logical appellation considering the international significance of the Blue Nile River, which originates at the outlet of Lake Tana.

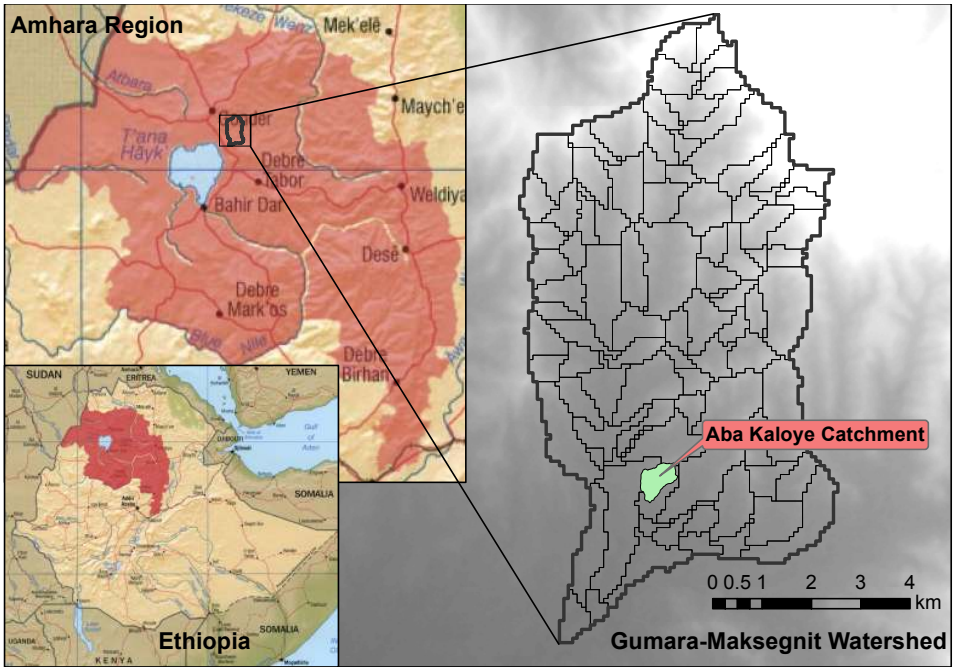

Figure (7) Map of the research area. As a part of the Gumara-Maksegnit watershed, the Aba Kaloye catchment lies north-east of the lake Tana and the Amhara region capital Bahir Dar. (Source: [top/bottom left *Online*; *Online*], modified)

The geographic position of the Aba Kaloye's channel network outlet is $+12°25'\,26.00''$ north, and $+37°\,35'\,7.20''$ west. A flume existing at this point lies at an elevation of 1990 meters above sea level (m a.s.l.) and the catchment reaches a maximum elevation of 2134 m a.s.l. Therefore it represents a small share of East Africa's 710 million km^2 of tropical highlands between 1000 and 2500 m a.s.l. The average population density in this landscape class is 79 inhabitants per km^2 and the dominant weathering type is medium to severe water erosion. Sheet and rill erosion as well as gullying are the most prevalent processes throughout the region (Figure 8) [Nyssen, Poesen, and Deckers 2009].

4.1.2 Climatic Conditions and Land Use

The Lake Tana Basin experiences a mean annual precipitation of about 1280 mm and an estimation of the actual evapotranspiration and the water yield of the basin is 733 mm and 392 mm respectively. With large diurnal and rather small seasonal changes in temperature, the catchment lies in the "tropical highland monsoon" climatic region [Setegn, Srinivasan, and Dargahi 2008]. Due to the geographic latitude snowfall is generally limited to the most elevated mountain peaks. The maximum precipitation of the prevailing 'unimodal' rainfall regime occurs during July and August, and the June to

Figure (8) At the end of the dry season, bare soil is prone to sheet and rill erosion. Despite many cracks boosting infiltration processes, surface runoff occurs during rainfalls of high intensities.

September period is the main rainy season, not only in the Lake Tana Basin, but in an agriculturally significant portion of Ethiopia (Figure 9) [Gissila et al. 2004; Seleshi and Zanke 2004].

The fading dry period leaves withered vegetation and as a result of tillage practices and famished livestock, vast areas of bare soil. It is during this time of the year when the brown vertisol given at the study site [Setegn, Srinivasan, and Dargahi 2008] features countless cracks several centimetres wide. The average depth of the heavy A-horizon is 70 cm (see 4.1.5), though the spatial variability of this property is high at the catchment scale.

Following the classification scheme Dixon [2001] provides, the 'Highland Perennial', 'Highland Temperate Mixed' and 'Maize Mixed' farming systems prevail in the region [Nyssen, Poesen, and Deckers 2009]. The author's impression gained during the fieldwork is that the highland tempered mixed system reflects the situation in the Aba Kaloye catchment most aptly. However, some non plant cultivation related parameters of the other two farming systems match his impression as well: the farm size is less than two hectares and cattle is numerous. Oxen-ploughing is a common practice and livestock also provides for milk and manure. The latter is true for goats and sheep as well, which also represent a substantial income share. Other income sources

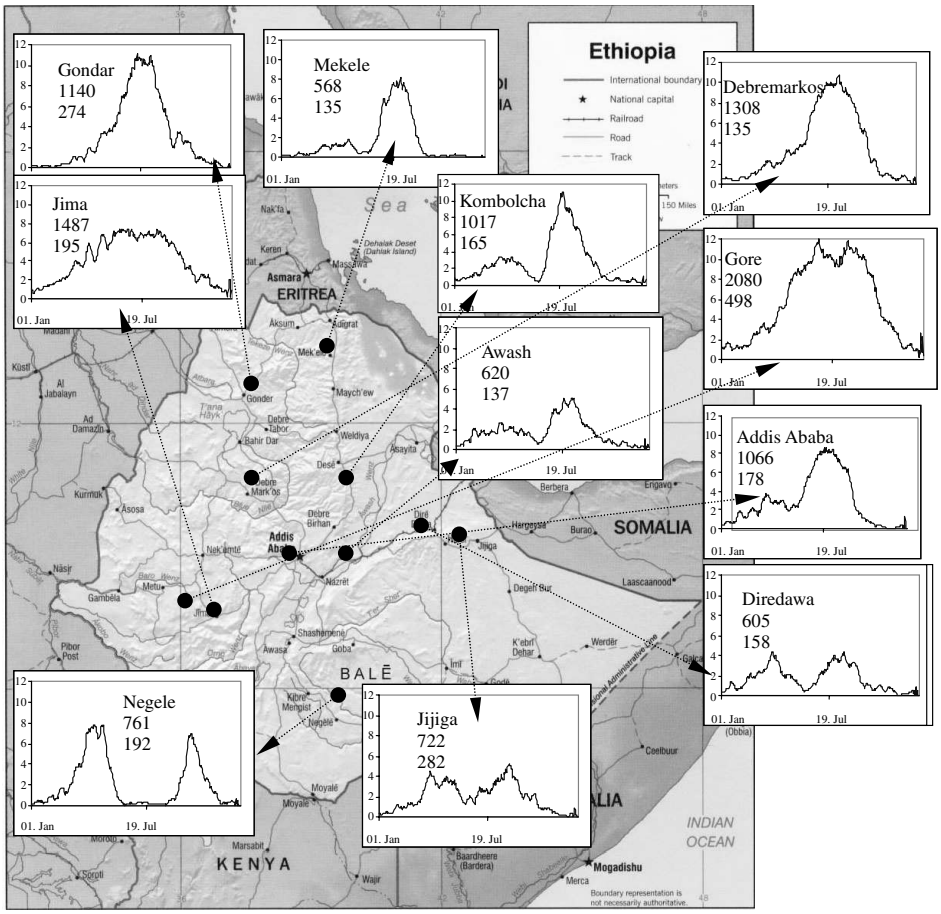

Figure (9) 10-day running mean rainfall (mm) for 11 stations in Ethiopia. Each graph contains numbers for the average annual rainfall and its standard deviation. The straight line distance between the Gondar station and the Aba Kaloye catchment is roughly 25 km (Source: Seleshi and Zanke [2004]).

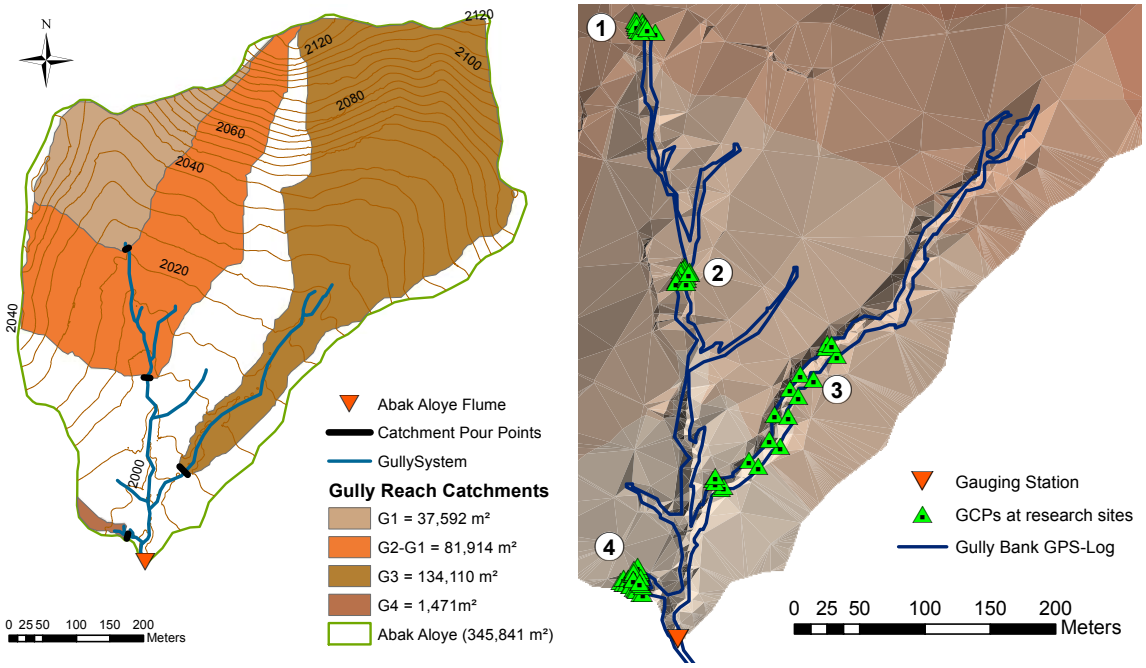

(a) The Aba Kaloye watershed and gully reach catchments

(b) Location of the gully reaches under investigation

Figure (10) Fluvial system of the Aba Kaloye catchment and gully reaches under investigation.

and staples are small grains, peas, broad beans and tef [Dixon 2001].

4.1.3 Hydrology and Sediment Regime

In the spatial domain of the Aba Kaloye catchment, partitioning of fields either follows topographic features such as gullies, divides or established footpaths. The total length of the drainage network equals approximately 1300 m (figure 10). The fluvial system in Aba Kaloye catchment comprises various channel types such as stabilized, active, permanent and ephemeral gully reaches and a deeply entrenched gorge, although field measurements were only conducted at reaches one to four in figure 10b. Most cultivated areas lie in the lower parts of the catchment, where gently rolling slopes form the landscape. Here, one deeply entrenched channel divides the catchment (see figure 44a).
At the gauging station, sensors exist to measure the discharge height and it's turbidity. An ombrograph records rainfall data in close proximity to the sensor-equipped weir.

Where possible, this study attempts to provide meaningful data to assess the gully erosion in the Aba Kaloye catchment. Distinct sediment yield originating from sheet/rill and gully erosion is of special interest.

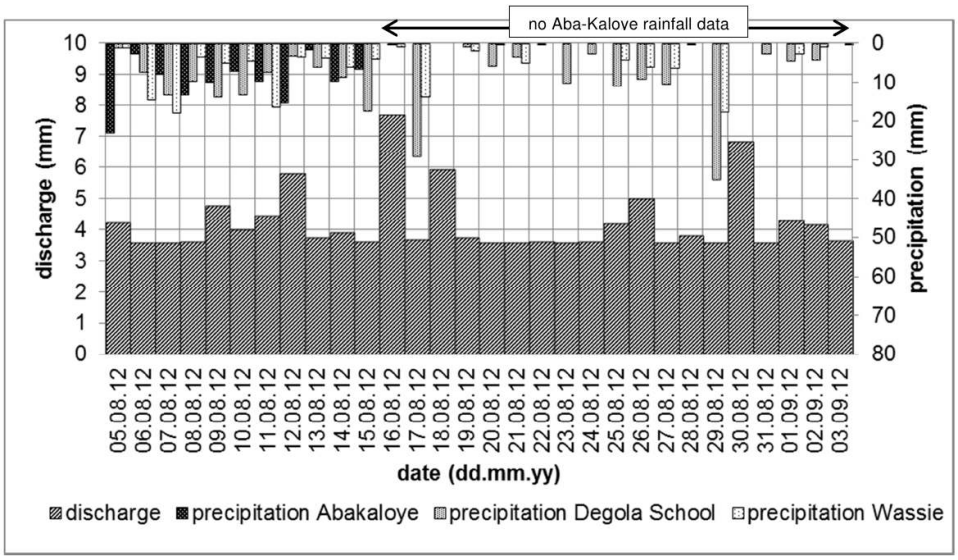

Figure (11) Rainfall and runoff events in Gumara watershed, the domain in which the Aba Kaloye catchment is situated. (Source: Zehetbauer [2014, p. 29]).

Zehetbauer [2014, 39ff.] specifies the catchment's runoff-coefficient, the ratio between runoff and rainfall, explicitly for nine storm events. These events lie in the same period this study focuses on and show runoff-coefficients between 9 and 35%. Unfortunately [Zehetbauer 2014, 41ff.] reports many technical difficulties with respect to data recording and while stressing the uncertainty of her results, she attests to a total soil loss of $12.93 tha^{-1}$ attributable to 15 runoff events in the period between July 5^{th} and August 12^{th}. Due to data loss and erroneous data, rainfall data at the Aba Kaloye rain gauge is limited according to figure 11.

4.1.4 Soil Degradation

The Lake Tana Basin area encounters various pressures on the natural resources of land and water. The potential of hydroelectric power generation, eco-tourism, intensified agriculture and livestock breeding results in the region being of national significance [Setegn et al. 2009]. Nyssen, Poesen, and Deckers [2009] state that current processes of land degradation are not attributable to recent hydrological changes (e.g. rain patterns). They rather tend to find causes in human activity without excluding the possibility of "Boserupian" processes.
In the field of soil degradation, the term "Boserupian process" describes developments, in which a higher population does not inevitably result in a higher pressure on land, but rather leads to innovations such as soil con-

servation strategies. On the contrary, "Malthusian" theories characterise a growing population as the cause for social and ecological stress, resulting in land degradation and harmful long-term effects [Grepperud 1996].

For natural conditions, Morgan [2005, p. 4] report erosion rates between 1 and $5\,t\ ha^{-1}$ for Ethiopia. When cultivated, these rates may increase to between 4 and $48\,t\,ha^{-1}$. Of course, this does not mean that erosion is visible everywhere, as spatial variability of soil properties, precipitation patterns, topographical gradients and especially vegetation cover results in a spatial variability of erosion phenomena. Nevertheless, Setegn et al. [2009] stress a negative impact of soil erosion for the whole Lake Tana Basin. They mention off-site impacts such as sediment deposition, a reduction of storage capacity, flooding, pollutant and nutrient transport. As a main cause, they postulate the rapid growth of population, deforestation and overgrazing. Furthermore, they attest a failure of land and water resource planning as well as a lack decision support tools.

In contrast, Nyssen, Poesen, and Deckers [2009] conclude that in many areas rehabilitation is under way. This is the conclusion of several studies conducted in tropical highland areas, inter alia the Tigray region of Ethiopia. Nevertheless, the authors cite the need for extended in situ soil and water conservation and nutrient management practices. This might be espacially true for the Lake Tana basin, a region gaining less attention in the studies Nyssen, Poesen, and Deckers mention.

4.1.5 Data Acquisition and External Data

Image acquisition and plumb lime measurements took place during three measurement sessions (S1–S3) at June $26^{th}/27^{th}$, August $8^{th}/9^{th}$ and September $3^{th}/5^{th}$ 2013. Figure 12 illustrates the intervals between these dates and provides an overview on the data available from cooperating projects.

In addition to data recorded at the weather and runoff gauging stations, third party topographic data from a field survey allows for the assessment of gully catchment areas. A GIS-based Kriging algorithm uses surveyed point data with an average nearest neighbour value of $8.7m$ and provides for a continuous elevation map. The catchment areas in figure 10a are the result of a subsequent surface flow direction analysis.

Furthermore, a soil map point-dataset with a resolution of 500m allows for the spatial interpolation of soil depth and texture parameters [Mehammednur Seid et al. 2013]. Table 1 lists the outcomes of the ordinary Kriging interpolation of his data. Since these soil parameters possess a high spatial variability, the point information for G1 through G4 should be treated with caution.

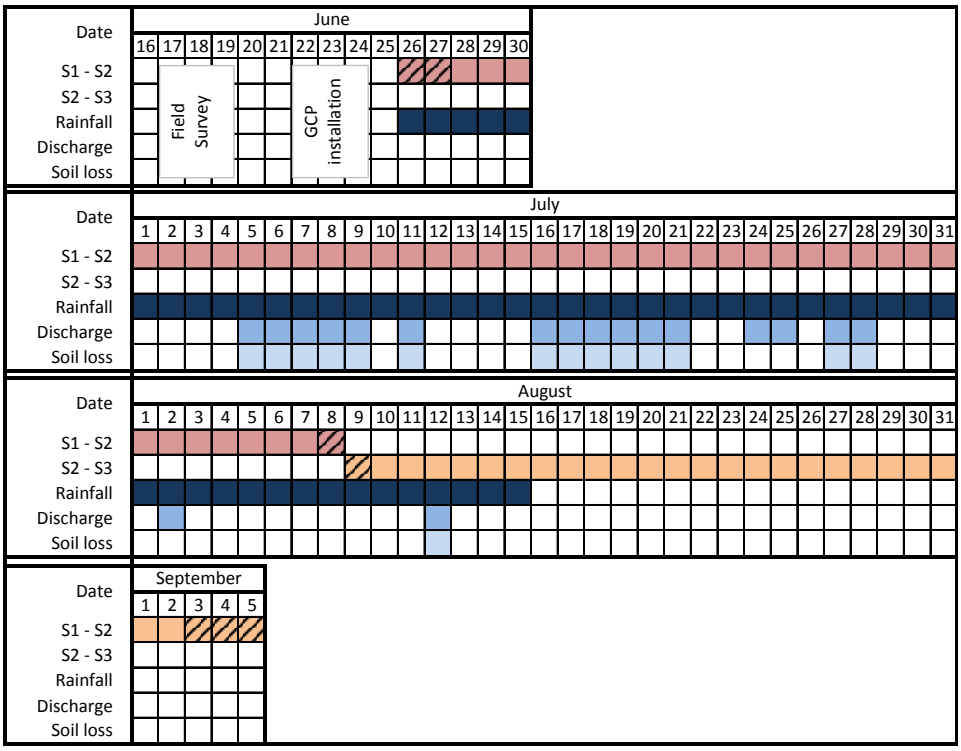

Figure (12) Field work schedule and data availability for the rainy summer season 2012. Hatched boxes indicate the days of the photogrammetric and manual data recording. (Rainfall, discharge and sediment data: Zehetbauer [2014, 68ff]).

Table 1: Soil parameters at the locations under investigation (Data: ongoing partnering projects (ICARDA, GARC) and [Mehammednur Seid et al. 2013]).

Research Site –	Depth cm	Sand %	Silt %	Clay %
G1	91	30	31	39
G2	91	28	29	43
G3	87	28	28	44
G4	98	26	23	51

4.2 Fieldwork

During an initial field survey the selection of four gully reaches took place. No stringent rules where set up as a decision support system, however parameters such as surrounding topography, channel inclination, the incidence of head cut features and a qualitative estimation of reach activity influenced the choice of the four locations. Figure 10 shows the distribution of four

research sites in the catchment and figure 13 includes a more detailed map displaying the gully reaches under investigation. The appendix to this work includes photographs of the gully reaches (see 7.1).

Gully 1 (G1) is the topmost channel reach in the catchment. At the time of a first field survey, early rainy season's precipitation events already scoured out a vertically scarped headwall basin. Overhanging, vertical and near-vertical side walls at the top of this reach change into more sloping walls approximately 10 m down the channel at CS4. Vegetation eventually covers the side walls of the gully and further down the incision levels out with the surrounding terrain at several segments. However, even at unimpaired sections of the thalweg, drift and other indices testify ephemeral surface flow.

Approximately 200 m below G1, another nick point cuts significantly into the thalweg. At this point the second investigation area (G2) was set up, where CS5 - CS8 cover another apparently active gully reach over a length of approximately 13 meters.

The lower segment of the catchment's eastern gully system branch (see figure 10) was selected for its remarkably low ratio between gully width to depth (W/D ratio). The gully itself predefines the G3 research area: in between CS9 and CS14 it is simply not possible to leave or enter the gully. Since it was hardly possible to establish GCPs within the gully (see 4.2.1), it was necessary to use GCPs at the two ends to the deep V-shaped trench to provide for sturdy absolute orientation parameters (see 3.1.2).

The fourth investigation site is an (ephemeral) valley side gully with a maximum continuous extent between its head — although a rather smooth transition makes it difficult to pinpoint the top end of the gully — and the merging point with the valley floor gully of about 40 m. The lower part of this gully forms a deep trench, often exposing bedrock material. Close vegetation, mainly impenetrable scrub (as figure 14 depicts), covers this section of the gully, making plumb line measurements nearly impossible and the photo-recording strategy as described in section 4.2.4 not applicable. Therefore, this study investigates the two sub-reaches G4.1 and G4.2 which respectively cover 18m from CS15 to CS23 and 10 m from CS24 to CS21.

4.2.1 Photo and Cross-Section Control:

For both measuring techniques outlined in this chapter, a network of reference points along the gullies under investigation was necessary. Zachar [1982, pp. 140-114] provides a repertoire of various objects adequate as permanent or provisional on site markings. For the stationary method of levelling (the pole method) fixed points represent start and end marks when stretching a level string over the gullies. For the photogrammetric approach, such permanent markings are essential for the camera orientation and to orientate different (geodetic) model within one local coordinate system.

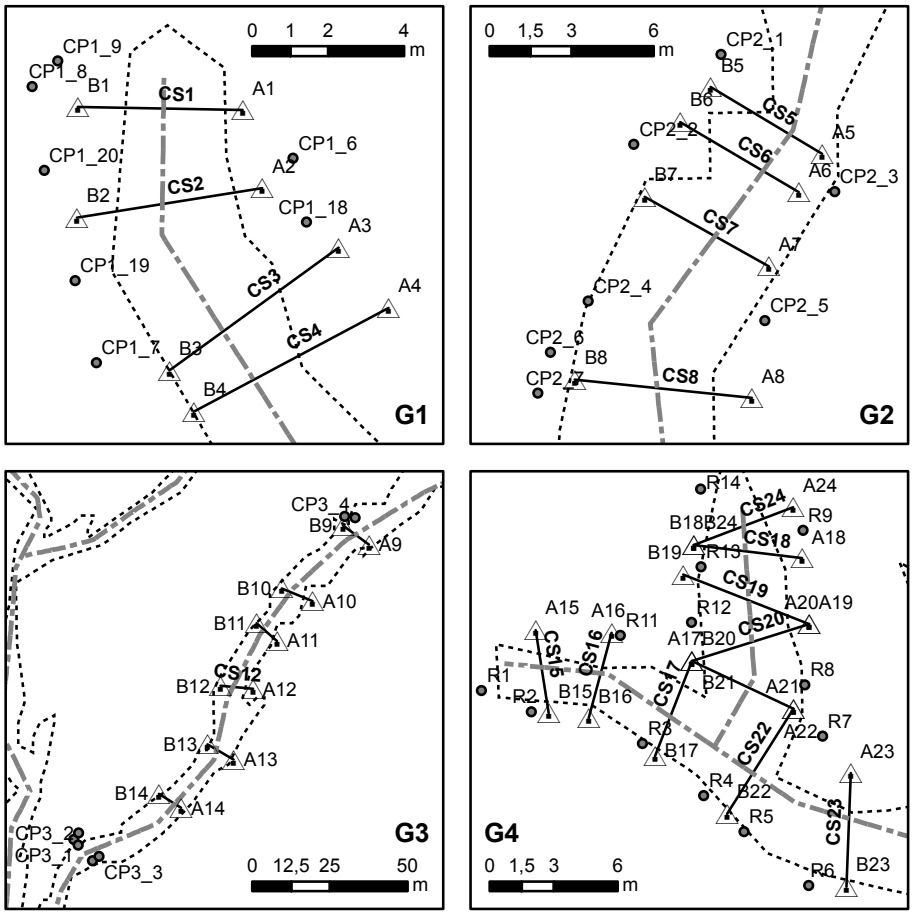

Figure (13) Labelling of the gully reaches starts at the highest elevation (G1) and this strategy was applied to the cross-sections as well (CS1, CS2, ..., CS24). The CS-defining GCPs are consistently labeled as A1–A24 and B1–B24.

Figure (14) The gully site number four shows ephemeral gullying processes at the top most investigation areas, and a deep channel section establishing a continuum with the main floor valley. The foreground scene shows two GCPs supporting a CS reference line.

The Ethiopian rural highland environment requires specific precautions when selecting marker materials. Termites undermine the long term stability of untreated wooden pins and metal rods are a valuable good which are therefore easily lost. In order to overcome these threats, partly buried stones were set up along the gullies under investigation. This was possible since local farmers commonly spare out a strip along the gullies when tilling the land.

The stones served as temporal GCPs and therefore had to be in place for the entire time-window of research from July until September 2012. To increase the accuracy of all measurements, a cross or circle was painted on the top side of the stones depending on their purpose as control- or validation-points. In the context of an ICARDA-Coordinated research project, colleagues supervised a topographic survey of the catchment and geo-referenced a first set of GCP coordinates in cooperation with an external service provider. The remaining GCPs for G1 where surveyed during a second pass, again by an external service provider who unfortunately delivered the coordinates in a

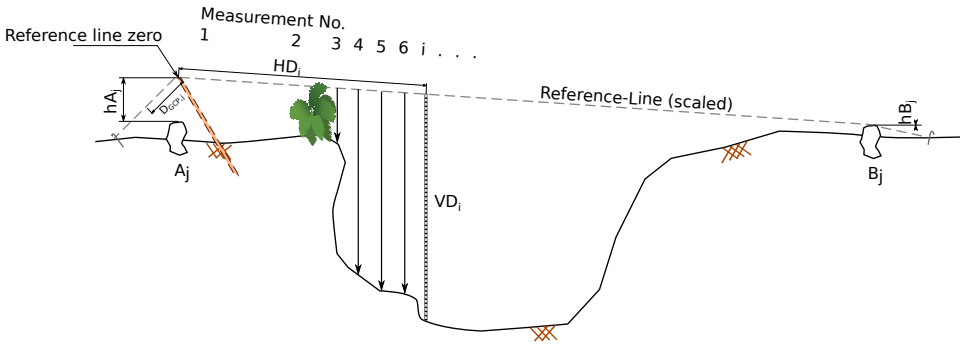

Figure (15) Scheme for setting up a plumb line CS measurement.

reference coordinate system and data format different to the first set. However, the survey took place at the end of the field-work period. It was therefore possible to add GCPs at any time. This was necessary for CS24, which was added to the set of CS after a rapid longitudinal growth of G4.2 (the northern branch of G4 in figure 13) had taken place during the time-interval between S1 and S2.

4.2.2 Cross-Section Measurement

At certain cross-sections where the two reference string-anchoring GCPs happened to be below the ground or vegetation between them, inclining timber stakes with an approximate length of 55 cm were installed in order to lift the line. This was done in such a way that the top end of the stakes ended up above the GCPs and allowed them to serve as diagonal struts (see figure 15).

To avoid errors, the reference line zero-point was set up in (horizontal) coincidence with a GCP situated at the orographic left (A_i) side of the gully. It was not possible to consistently follow this strategy so we recorded the offset between zero-point and the GCP (D_{GCP}) and considered it in the partial automation of a subsequent CS analysis.

Using a metal tape measure hooked to the reference line, the plumbing distance VD_i was measured in regular intervals at string marks $D_{GCP}+HD_i$. HD_i intervals where reduced to 5 cm to record abrupt morphological changes and extended up to several decimetres, where no topographic changes prevailed. The latter was mostly applied beyond the gullied area to cover the unimpaired soil surface. This provides a validation criterion when comparing the same CS measurements of distinct measurement sessions.

In addition to the CS plumb lines, the perpendicular distance between the site specific topmost CS to the corresponding gully head or nick point (NPD) was measured following the approach figure 16 illustrates. Since CS24 was

(a) Measuring the nick-point-distance at G4.1

(b) Measuring the nick-point-distance at G2

Figure (16) Some situations required the use of sticks, vertically oriented by sight, to alleviate nick-point-distance (NPD) measurements

added just before the recording session S2, the total head retreat above the formerly topmost CS18 calculates for S2 and S3 as the sum of the distance between CS18 - CS24 and the NPD above CS24.

4.2.3 Practical Photogrammetric Issues and Accuracy Estimation

The mean photo scale M_b or the mean photo scale number m_b describes the relation between recording distance h and focal length c or the point distance X in object space, compared to point distance x' in image space (see figure 2).

$$m_b = \frac{h}{c} = \frac{X}{x'} = \frac{1}{M_b} \tag{11}$$

Facing the technical specifications of recording or scanning systems, an adequate photo scale is important to achieve expedient object space resolutions. At this point it is important to differentiate between accuracy in the directions of X and Y, and the accuracy in the Z dimension of a stereo-model.

$$dX = m_b \times dx' \qquad dY = m_b \times dy' \tag{12}$$

$$s_X = m_b \times s_{x'} \tag{13}$$

While simply applying error propagation to the image measurement accuracy dx', the derivation of (11) results in an estimation for the first two dimensions (12) and the mean error s_X (13), this is not true for the latter. Here, the differentiation (14) of (2) suggests that the object space accuracy depends on the scale m_b as well as on the distance to base ration h/b.

$$s_z = \frac{Z^2}{b \times c} \times s_{px'} = \frac{h}{b} \times \frac{h}{c} \times s_{px'} \tag{14}$$

Thus, the relative orientation of image pairs strongly affects the usability of these photos in a photogrammetric project. With a small basis b, glancing intersections of homologous image rays arise and the measurement accuracy deteriorates. The terms strong and weak angle of separation describe the shape between the intersecting lines PO' and PO'' in figure 2. For the determination of depth-values, its optimum is 90 degrees. While this optimum angle of separation has positive effects on the stereo model quality, it undermines (automated) feature matching due to the significantly different perspective between the two images of the pair.

Considering the distance h to be constant, the need for overlapping image areas in combination with a defined focal length limits the maximum basis b. When modelling an erosion gully with ground based photography, the distance h mainly depends on the recording strategy. Gully morphology, vegetation at the gully banks and the availabillity of camera positioning tools (equipment in general) are factors this strategy depends on. Figure 17 illustrates an approach, in which pictures of the incision wall and floor are taken standing opposite to these features and beyond the edge or breakline of the gully. Assuming the gully width to be three meters, the average distance from the camera position to the gully wall surface may be $\approx 6m$. Nevertheless, the distance X^* from the camera to the gully sole or an arbitrary point (e.g. an GCP) at the opposite gully bank is somewhat smaller in the first, and significantly bigger in the second case. With the camera constant being e.g. $c = 6mm$ for a compact camera, the photo scale number calculates to $m_b = 1,000$ for the regions showing the gully wall. Further assuming the camera sensor pixel pitch to be e.g. $1.52\mu m$, a resolution of $1.52mm$ is feasible at the gully wall.

While techniques such as sub-pixel target matching aim to mitigate the rather low resolution in regions beyond the opposite gully break line, the low intersection angle between image rays and the surface is yet another factor potentially preventing the establishment of dense surface models. Even with good h/b ratios prevailing, model imperfections (imperfect relative exterior orientation) lead more easily to a backfiring feature matching algorithm, which assumes a feature to be at a certain position in space.

4.2.4 Photogrammetric Survey

Before each photo recording session, targets in the form of round yellow plastic lids with a diameter of 95 mm where put on top of the GCPs. Vegetation sometimes necessitated elevating the targets. Lumps of clayey soil

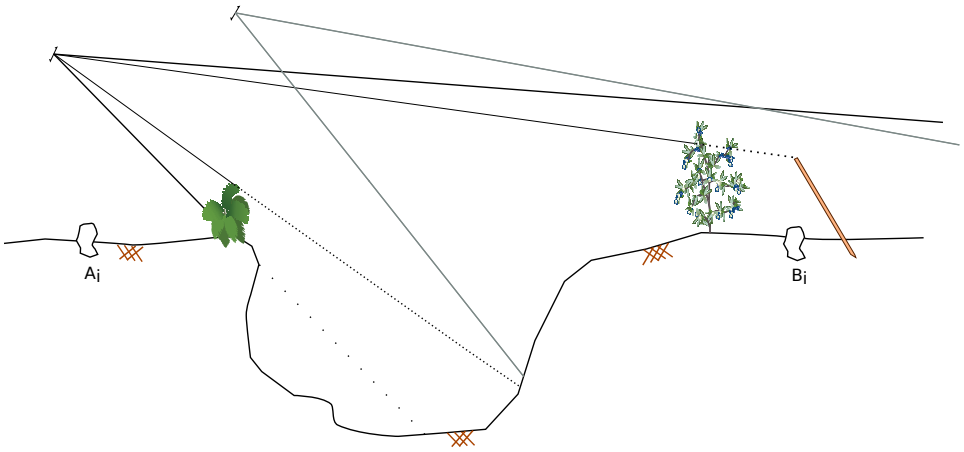

Figure (17) The gully morphology, especially the width and depth affect the recording distance h when following a photo recording configuration lateral to the erosion channel.

facilitated the glue to put the targets on top of timber stakes. Some of the stakes were set up explicitly for this purpose, but at some locations, stakes were reused from the prior plumb line CS measurement. When carrying out the analysis this turned out to be a mistake, as stakes installed to lift the CS reference string potentially obstructed the view to the actual GCPs. The targets height above the GCP was determined with a measurement tape and recorded with 5 mm accuracy.

Table 2 lists the photos taken with a Panasonic DMC-FT1 consumer camera. The CCD sensor of this device covers approximately 12.2 effective Megapixels over 4011 columns and 3016 rows. It is impossible to deactivate the optical zoom of this camera, so the minimum focal length of the optical zoom was used to take all images. Section 4.3.2 describes the later calibration of the camera which was conducted with the same camera configuration.

Photo recording for the gullies number 1, 2 and 4 followed the strategy that section 4.2.3 briefly describes and figure 17 illustrates: The recording took place with the projection-center situated at either the orographic left or right hand gully bank and the orientation towards the opposite gully wall and (if possible) the gully sole. After each shot the camera position moved parallel to the gully guaranteeing an image overlap of at least 60 percent. The intention was to achieve a larger overlapping area. Having small distances between each camera position (the basis so to say) allows one to select image pairs with geometric properties adequate to their purpose.

Table 2: Number of photos taken of each gully during the field-sessions S1–S3

Gully	S1	S2	S3	Σ
G1	151	98	167	416
G2	85	104	148	337
G3	323	232	283	838
G4	108	68	327	503
Σ	667	502	925	2094

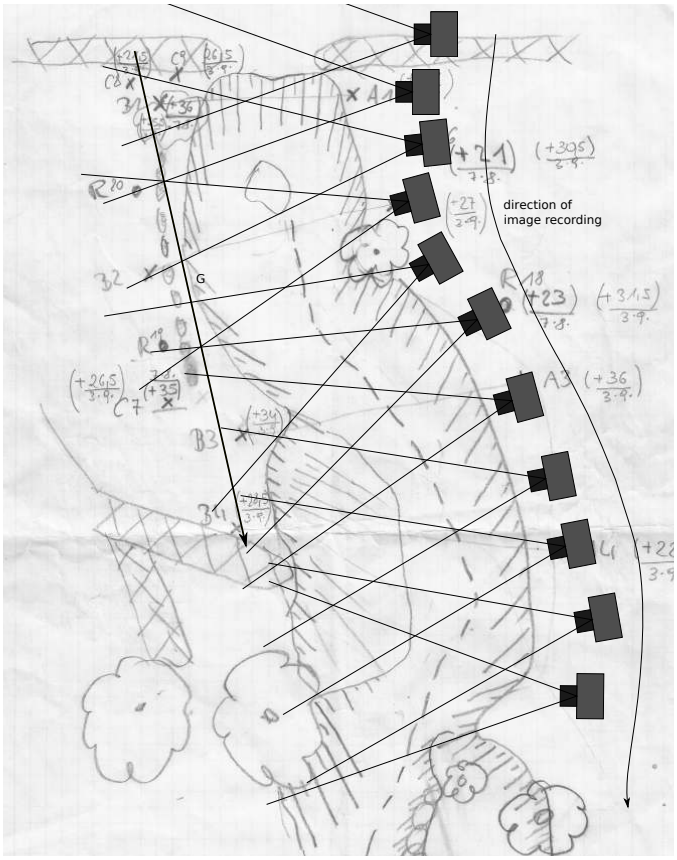

Figure (18) The schematic overlay of a sketched field map highlights the GCP distribution in the whole research area (elliptic marks). It further includes exemplary camera positions, overlapping image frustums and the area a photogrammetric model could cover. GCPs available for the absolute orientation string together following vector G.

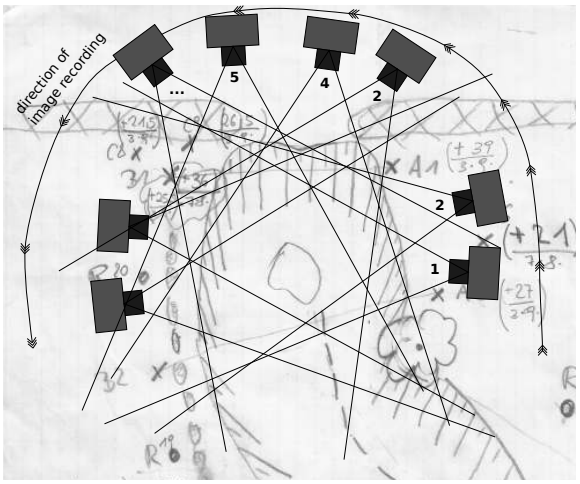

Figure (19) An approach to record images for a stereoscopic model covering both sides of the gully. The pictures shot from above the gully head do not necessarily comprise surface modelling qualities, they rather connect the two opposing image sets. This, in turn, results in GCPs (elliptic marks) scattered over the whole model area, providing strong parameters for an absolute orientation transformation.

Considering the dimensions and geometry of the U-shaped gullies number 1 and 2 and imposing the necessity to include GCPs in the image sets results in glancing intersections between homologous axis and the terrain surface (figure 17). This aggravates the feature recognition and matching process since it compromises high-contrast and adequate sized targets. Luhmann [2002, p. 496] defines a lower limit of 20 for object surface and 45 for control point target intersection angles and stresses the threat of eccentric midpoints of round targets. Using yellow plastic lids to signalize GCPs allows for an adjustment of the targets to face towards the camera position, but it is impossible to ensure all points in the image extents to be below the aforementioned limits. Furthermore, it is especially difficult to achieve an even distribution of GCPs in the model because the gully edge and the recording perspective impose boundaries for their positioning at the opposite gully bank. Therefore, in a model which covers only one side of the gully, all GCPs are lined up. Thus, the 7-parameter similarity transformation is very sensitive to both flawed real world coordinate measurements and an inaccurate modelling of the very same coordinates. Vector G in figure 18 represents the axis around which a flexible degree of freedom exists for the model.

A possible solution to this problem is the integral representation of a whole gully section within one single photogrammetric model. Thus, the GCPs on both banks could be used for the final model transformation. Figure 19 illustrates how continuously taking photos while moving around the

gully head could deliver input data for modelling both walls and adjacent GCPs. Unfortunately this requires significantly variable image orientations which, despite their changing projection center location and perspective, allow for the (automated) measurement of homologous image points (feature matching, see 3.1.2) and the continuous stereo-model approximation via bundle adjustment. For this crucial situation at the gully head it is not important to ensure approximate image plane parallelism. Furthermore it is not mandatory that the stereo-pairs taken from above the nick-point (e.g. 2-4 or 5-4 in figure 19) cover any GCPs, as long as it is consistently possible to manually recognise and match other accurate tie-points in any of the image combinations.

At specific gully sections it was difficult to following the image recording pattern. Mainly due to vegetation at the gully bank it was impossible to achieving adequate camera positions. Only the ephemeral gully 4 allowed for absolute freedom in terms of exterior camera orientations. Despite that freedom, the subsequent processing of the images revealed that an insufficient number and/or inappropriate image orientations would delay the aforementioned cohesive model approach figure 19 illustrates.

The only way to take overlapping photos at G3 was to walk along the gully sole and take photos at a certain degree to both sides. Due to the resulting stereo image geometry, this data is difficult to process. After various failed attempts of automated image orientation, further attempts to evaluate of gully 4 were found to be too labour-intensive for this study. Deep V-shaped gullies may require the use of dedicated SfM software to allow for CRP-process automatisation.

4.3 Dataprocessing

To compare data from the plumb line measurements with the outcomes from the CRP analysis, (i) three dimensional surface coordinates, (ii) cross-section areas and (iii) volumetric variables are the focus of this study. Following subsections describe the establishment and embedding of three dimensional coordinates in a common superior coordinate system (WGS 84) and the evaluation of the variables enumerated previously.

4.3.1 Plumb Line

The geographic definition of each plumb line reading X_{PL} is given by the coordinates of the reference-line anchoring GCPs (A_i, B_i in figure 15 and 13), the height of the reference-line above them (hA_i and hB_i) as well as the horizontal and the vertical measurement distance VD_i and sHD_i.

Representing gully cross-sections by a set of simple geometric shapes is a way to assess their total area $A_{CS,j}$. In order to avoid the influence of the occasionally artificially raised reference-line, an imaginary vector AB

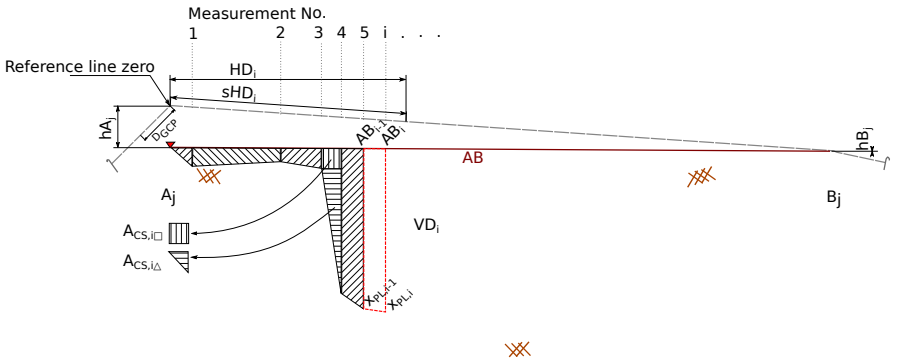

Figure (20) Discretisation of a Gully CS into simple geometric shapes. The perimeters AB, VDi, VDi-1 and the soil surface define each 'CS-Slice' and a trapezoid (the combination of $A_{CS,i\square}$ and $A_{CS,i\triangle}$) approximates its area.

connects A_i and B_i and forms the upper edge of the geometries. While this still does not result in the calculation of absolute CS-areas[1], it increases the meaning of quantitative aerial changes.

Figure 20 includes two points of the soil surface ($X_{PL,i}$ and $X_{PL,i-1}$) as well as two points on AB (AB_i and AB_{i-1}) which define a single geometry of the CS-area. Linear interpolation between the elevations of two GCPs provides for the absolute Z-value of AB_i and for each point on the reference-line. For the sake of simplification the horizontal distance between points on the references line and the (elevated) GCPs A_i equals the skew distance between the coordinates ($HD_i \approx sHD_i$). The applied calculations further assume AB to be horizontal. As a result the area sum of a rectangle and a triangle or a single trapezoid may represent each CS-slice. Inaccuracies due to a slacking and also slightly stretching reference line are likely to outweigh the these simplifications. Based on the evaluation of 18 CS the length error this approach introduces is 0.41% at maximum and 0.16% on average for AB, and 0.58% at maximum and 0.19% on average for the reference-line.

Using the product of average CS areas and averaged distances between the anchor points (A_j and B_j) simply approximates the gully volume in between two CSs (15).

[1] In order to evaluate correct absolute figures, a qualitative manual or geo-statistical approach is necessary to define the gully edges

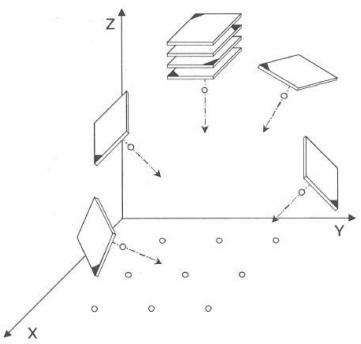

(a) 8 Camera-positions above a test field without GCPs (Luhmann [2002, p. 508])

(b) One out of 12 shots for a calibration attempt at the Gondar Agricultural Research Institute.

Figure (21) Calibration software demands a certain amount of photos that show varying perspective angles and cover a high share of the image plane.

$$V_j = \frac{(A_{CS,j} + A_{CS,j+1}) \times (d_A + d_B)}{2} \tag{15}$$

with

$$d_A = \sqrt{[X(A_{j+1}) - X(A_j)]^2 + [Y(A_{j+1}) - Y(A_j)]^2}$$

and

$$d_B = \sqrt{[X(B_{j+1}) - X(B_j)]^2 + [Y(B_{j+1}) - y(Y_j)]^2}$$

4.3.2 Close Range Photogrammetry

Camera Calibration: Eos Systems Inc. software PhotoModeller Scanner® (PM) comes with a tool-set to define the interior orientation parameters of a camera. The software also provides for self- or on-the-job calibration capabilities. Despite the latter being a somewhat advantageous approach for certain scenarios (see 3.1.2), a planar test field was used in this study to perform the camera calibration.

PM uses a) a term for radial and b) a term for de-centering distortion effects, but the formulation of the former is different to (3) in paragraph 3.1.2. As a result, the parameters K1 – K3 in table 3b are not equal to A1 - A3 in the balanced distortion formulation and a conversion is necessary to use the calibration results with other software. The PM manual explains

Table 3: Camera calibration results for a Panasonic DMC-FZ8

(a) Camera parameters

Parameter	Value	Unit
Focal Length:	5.1543	mm
Format Size		
Width	6.2999	mm
Height	4.7250	mm
Principal Point		
X	3.0897	mm
Y	2.3713	mm

(b) Lens distortion

Parameter	Value	Unit
Lens Distortion		
K1	9.473×10^{-4}	mm^{-2}
K2	2.666×10^{-5}	mm^{-4}
K3	0.000×10^{0}	mm^{-6}
P1	2.600×10^{-4}	mm^{-1}
P1	1.731×10^{-4}	mm^{-1}-

(c) Calibration quality

Parameter	Value	Unit
Calibration Quality Values		
Overall RMS	0.3302	px
Max Residual	0.9057	px
Photo Coverage	92	%

the necessary relationships, though a transformation was not required for this study. The parameter P1 and P2 describe the decentering or radial-asymmetric and tangential distortion and are equal to B1 and B2 in (4).

The parameters in table 3c, 'Overall RMS', 'Maximum Residual' and 'Photo Coverage', are not internal orientation parameters, but they reflect deviations of measured point marks from their position in the explicit solution of the basic collinearity equations. 'Photo coverage' is the area share of the image which is covered by the calibration and is a result of how well the point marks in figure 21b fill the scene. These indicators therefore provide feedback about the calibration quality.

Photogrammetric Models: After the first attempts at creating models from images sourced during the field sessions it became clear that many of the image sets only partially fulfil the requirements to serve as model input data. There are different approaches to a) enhance the image qualities and b) to create holistic models by using additional (non-photogrammetric) spatial data in order to enable the photogrammetric process with suboptimal data sources. However, due to time constraints the photogrammetric models in this study only covers the research site with the highest availability of quality imagery (G4) at two different points in time.

No image preprocessing, such as spatial or frequency filtering [Luhmann 2002, 375ff.] was performed, yet this is not the reason that none of the image data of gully four could provide for a holistic model. On the contrary, it was the geometric difficulties section 4.2.4 explains, which made it advantageous to implement five sub-models representing G4 at S2 and four sub-models representing G4 at S3.

Of course it is possible to manually identify and measure features for the bundle adjustment process, but the software PM also supports the automation of this step. 'Smart points' are automatically recognised and matched object features. They can provide all information necessary to relatively orient multiple images. It is also possible to include manual point measurements in the image processing of a 'smart points project' and from personal experience it can be said that this is a efficient approach: The automated image orientation process of a 'smart points project' quickly shows whether the selected images result in a robust model and existing orientations allow for a software guided marking of GCPs.

Purely manual marking and referencing of features is somewhat more tedious but makes the user recognise relevant image properties which is useful for further studies. This strategy also allows for the use of photo-sets with higher orientation variability where feature matching algorithms would fail. Such images are most likely not useful when it comes to the surface reconstruction process but can increase the chance that certain scenes (e.g. the scene figure 19 shows) can be modelled at all.

Table 10 and 11 condense essential information of all models used for the method comparison. Each table lists a certain number of self-contained photogrammetric sub-models. They show the according number of photos/smart-points/GCPs as well as each project's point-could-size (PCS) and overall point marking RMS. According to the software user manual, point marking residuals are differences between the point a user marks in the photos and the ideal case x,y-pixel coordinates the program calculates for the same object point. The residual root mean square (RMS) averages the errors of all explicitly marked points in the project.

This study uses another quality criterion, the comparison of modelled and surveyed real world GCP-coordinates, to validate and assess photogrammetric models. Therefore, not all available GCPs are set as parameters for the Helmert transformation, which PM uses to establish the absolute orientation of models and point clouds. The GCPs or check points (CP) surveyed in excess, together with their modelled pendants, then give a reliable measure of the model and absolute orientation quality. This is especially true if the CPs are distant to the transformation coordinates. Tables 12 to 20 provide information on the error of both GCPs used as transformation parameters and CPs.

Dense Surface Models: In all sub-model projects, only image pairs with geometric parameters within certain thresholds serve as input data for the dense surface model (DSM) generation process. PM Scanner® assists photo selection by listing the b/h ratio and the angle separation of all photo pairs in the project. The software suggests using pairs with an h/h ratio between 0.2 and 1.0 and, in contrast to requirements of the bundle adjustment process, a rather small angle between the camera stations ($< 20°$).

Each image pair forms the basis for a single point mesh. Photo input for the DSM generation process allowed for a point sampling interval between coordinates of less than 5 mm. However, a sampling distance of roughly 10 mm was used in this study. Subsequent to the DSM generation, the software comprises functionality for the subsequent consolidation of these point meshes. The use of PM Scanner® furthermore enables the removal of redundant points, to thin out the point mesh, to create, fill and smooth a triangulated irregular network (TIN) surface or to clear outliers. The prevailing workflow only merges all point meshes of a model, removes point redundancy and those outliers which obviously classify as vegetation taller than grass.

Especially when dealing with lush vegetation within the perimeter of the model, restricting the area available for DSM generation is preferable to a subsequent editing of DSM process results. In the framework of this study it was simply faster to draw 'DSM-Trims' as polygons on each photo than removing unnecessarily generated DSM regions, which potentially obstruct the deviation of surface models.

Model Post-processing: Despite PM Scanner® provides functionality to export surface cross-sections, the approach here is to export all generated point clouds and combine them in a geographic information system (GIS). This bears the advantage that CS-extracts can be derived from either a raster or TIN surface. In the prevailing case this is a four-step process:

1. After exporting the DSM point clouds of CRP-projects belonging to either session two or three (see table 10 and 11 respectively) to text files, a R-macro[2] merges the point data. As each line of the text file represents a point and it's corresponding RGB-color space values, this process potentially incorporates color-based filtering. The code used in the prevailing study creates two output files for each gully model: One containing all points, and one containing only points where the green cromaticity is smaller than either the corresponding blue or red value. This is supposed to reduce the impact of living biomass but is by far not scientifically based.

[2] see [*The R Project for Statistical Computing* 2006]

2. Conversion to a performance oriented data format and further processing: Despite Esri's GIS software ArcGIS®[3] theoretically being capable of dealing with serious amounts of point data, it showed poor performance when importing the DSM point clouds originally comprising a total of roughly 3.8 and 5.5 million points for G4 at S2 and S4 respectively. The solution was to interpose tools developed for lidar data processing. The LAStools software suite [Isenburg 2014c] includes the following programs. The list reflects the order of their use in the framework of this study:

   (a) text2las: 'Converts LIDAR data from a standard ASCII format into the more efficient binary LAS/LAZ/BIN representations' [Isenburg 2014d].

   (b) lasthin: 'A simple LIDAR thinning algorithm for LAS/LAZ/ASCII. It places a uniform grid over the points and within each grid cell keeps only the point with the lowest (or '-highest' or '-random') Z coordinate' [Isenburg 2014b]. Using lasthin in the context of this study follows two main ideas. First, it helps to overcome the aforementioned performance issues by reducing the data. Secondly, it alleviates the influence of above-ground vegetation. Therefore the algorithm must be configured to search for the lowest Z coordinate and at least one soil surface point representation must exists within a grid cell. Beside the point-selection strategy, the length of a raster cell edge (thinning grid edge length – TGEL) is the second parameter of the algorithm. To investigate the effect of decreasing surface point densities on the method comparison, this parameter was altered between 1, 2, 5, 10, 20 and 30 cm for the DSM Point clouds without RGB based point decimation. Only one thinning result was generated using the RGB-filtered point cloud data and a thinning grid edge length of 5 cm.

      Per investigation session, the result of that operation were four LAS files derived from the original DSM clouds, and four file derived from the RGB-filtered DSM clouds. The latter was thinned out with a cell edge length of 5 cm.

   (c) las2shape: 'Converts LIDAR from LAS/LAZ/ASCII to ESRI's Shapefile format by grouping consecutive points into MultiPointZ records' [Isenburg 2014a]. All binary LAS documents as well as the original DSM cloud ASCII files were finally converted to shape files accessible to the GIS software.

3. GIS import: The items listed in table 21 and 22, except the ones representing original DSM point clouds, were subsequently imported to the GIS Software.

[3] see Esri's ArcGIS product website, [Esri 2014]

4. DEM Surface generation: In this study, point feature classes represent gully topographies and are stored in a terrain dataset. This dataset contains the surveyed GCPs as well. Both the point features and the GCPs are the basis for surface data in the terrain format, which in the prevailing case is basically a TIN surface held within Esri's spatial database format.

At this point it is important to point out that while this approach works well for G4, it would produce misleading results for the other gully reaches. The reason is that only distinct data formats and tools of Esri's ArcGIS or the Lastools software suit are capable of dealing with real 3D data. Especially the head regions of G1 and G2 feature overhanging faces which can not be processed or even stored. A data format problem most obviously prevails when using raster datasets. In this format each cell can provide for one Z value only.

4.3.3 Method Comparison

As mentioned at the beginning of this section spatial point-, areal- and volumetric variables serve to compare the plumb line and the photogrammetric method.

Coordinate Z-Values: To juxtapose soil surface elevations from the plumb line measurements (Z_{PL}) with those from the CRP measurements (Z_{CRP}), it is necessary to extract the corresponding surface elevation from the surface model. Therefore, 14 different terrain surfaces resulting from the thinning approach subsequently provide for elevation data when draping 3D line geometries at the CS locations on them. Esri's 'Interpolate Line' tool (part of the 3D Analyst Extentions library) creates 3D poly-lines, whose vertices (X_V) result from intersecting TIN edges with a 2D poly-line. Figure 22 illustrates how the line spatially intersects with certain TIN faces. Obviously the number of vertices depends on the TIN resolution (see figure 26).

After transforming the geometric data to a table format, applying Pythagoras' theorem to the x,y-position of a GCP and the interception points X_V (similar to the distance calculations in (15)) yields the horizontal (euclidean) distance $HD_{V,i}$ between these coordinates. Linear interpolating the elevation in between pairs of vertices ($X_{V,i}$, $X_{V,i+1}$) finally provides for elevation values ($Z_{CRP,HD}$) at arbitrary horizontal distances HD along the reference vector AB. Using this procedure, it is possible to look-up the CRP-based coordinate elevation at the very same spots where PL measurements prevail.

In this context the root mean square error (RMSE, see (16)) is a measure of the differences between plumb line and CRP elevation results. A second statistical measure for the accordance of the variables Z_{PL} and Z_{CRP} is the Pearson-Coefficient r. It provides information about the linear dependence

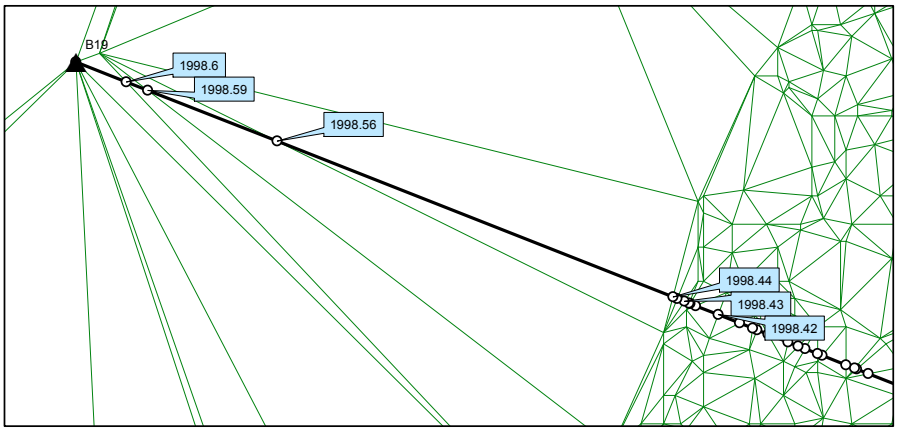

Figure (22) CS line intersection with a TIN and extracted line vertices congruent with TIN edges.

of the two variables and takes the value of 1, if each value of Z_{CRP} is equal to the according PL-measurement. Both measures where calculated for sample sub-sets representing a single CS, and for the collective data of gully four. They were evaluated respectively for datasets of recording session two and three.

$$RMSE = \sqrt{\frac{1}{n-2}\sum_{i=1}^{n}(Z_{PL} - Z_{CRP})^2} \tag{16}$$

Furthermore, this study evaluates the same statistical measures for a second set of variables. Here, RMSE and r result from the residuals between Z_{PL} and values of Z_{CRP} derived for positions $HD{+}Lag$. Using the Microsoft Excel® Solver add-on the lag value was altered with the target of minimizing the $RMSE_{Lag}$. This strategy aims at alleviating the random error of wrongly recorded reference line zero point offsets D_{GCP} in figure 15.

After assessing the RMSE change with respect to the thinning grid edge length (see 4.3.2 and figure 27), the decision was made to conduct the CS-area and volume comparison based on the CRP-surface data thinned out to one point per $4cm^2$ ($TGEL = 0.02m$).

Volumes: Processing of the plumb-line data integrates CS-areas over the gully longitudinal extent to derive volumes ($V_{PL,i}$) for each segment between two CS. Using zonal calculations in the GIS-based volume assessment, results in an analogous variable $V_{CRP,i}$. Index i refers to the lower end CS-number

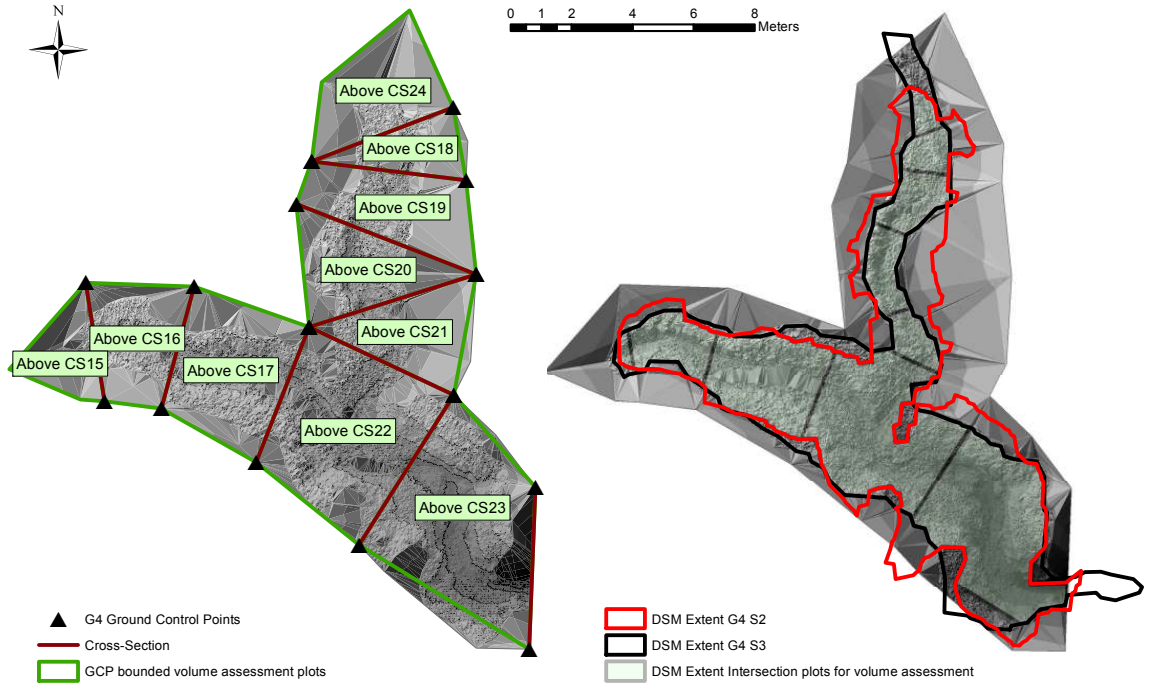

(a) (b)

Figure (23) Calculating the gully volumes explicitly for zones between cross-sections enables the comparison with plumb-line sourced volumes. 23b illustrates a further restriction of these zones to the perimeters of CRP-surface models.

of the volume-segment. Figure 24 shows the steps undertaken to derive gully volumes from a surface model.

GCP-coordinates span a TIN-plane which represents the unimpaired reference surface. After deriving raster-data surface representations with a cell size of one by one centimetre, summing up differences between elevation values of the CRP-model and the unimpaired surface results in volumes for each zone between two CS. In contrast to the PL-approach to derive the topmost segment volumes of a gully reach, no information about the nick point distance is available in the CPR-approach. Furthermore, no distinct incisions prevail at the gully heads of the G4 research site. This impedes the development of an objective (e.g. geo-statistical) process to define the gully boundaries. Instead, this study uses the unimpaired surface model and the DSM extents to limit the topmost zones ('Above CS15' and 'Above CS24' in figure 23a).

Reviewing the DSM Point cloud data revealed that surface information does not exist consistently within the perimeter of the GCPs (see 23a). As a consequence, the study comprises volume calculations which are potentially

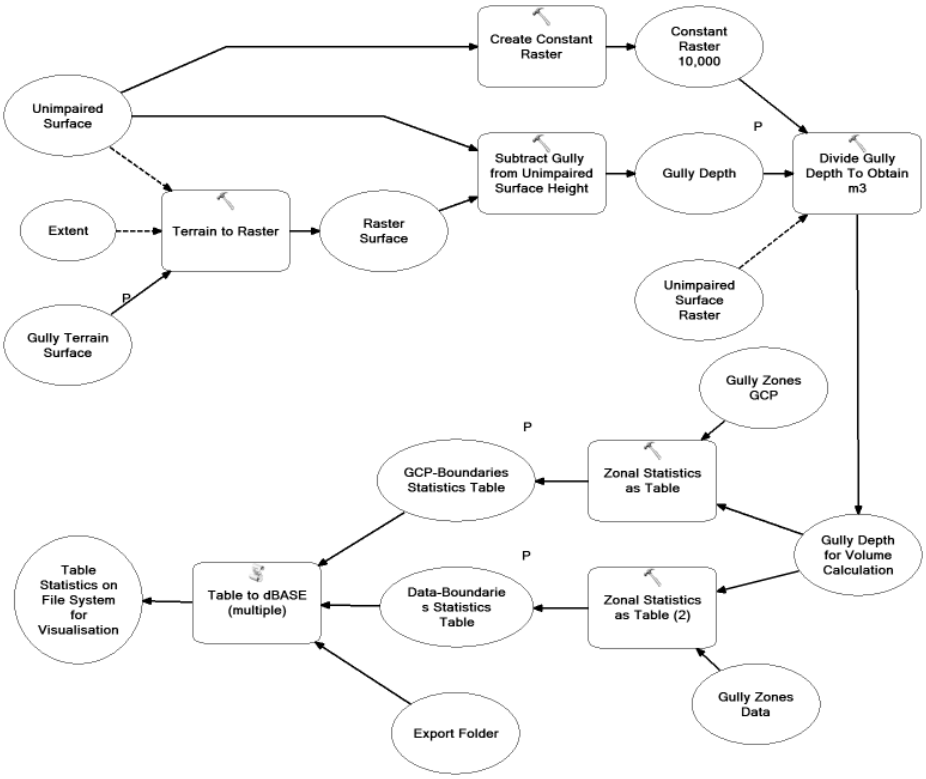

Figure (24) The data process from surface terrain to sectional gully volumes modelled in ArcGIS.

erroneous due to missing data. Volume calculations for zones limited to the DSM-data extents (23b) try to mitigate this weakness.

CS Areas: CRP-based estimation of CS-areas uses all coordinates (X_{edge}) gained from intersecting CS lines with the terrain surfaces such exemplarily illustrated in figure 22. According to the method used to compute A_{CS} from PL-Data, the strategy here again is to determine the elevation of points in the reference vector AB corresponding to X_{edge}. Finally, the horizontal distance between given points complete the geometric description of CS-slices.

5 Results and Discussion

5.1 Method Analysis

Despite the considerable amount of photos taken during three recording sessions, easy and partially automatized generation of CRP models was only possible for the G4 reach. At G1 and G2 either the automated image matching, or the attempts at generating consistent DSMs failed. Unsuccessful DSM generation is doubtlessly a result of flawed stereo models. This is the case when too few images of good geometrical quality are available as model input (see 4.2.4). One specific problem was the automated image matching of intermixed landscape and portrait format images, where only manual feature recognition and matching enabled the use of all photo sources.
However, this is not to say that it is impossible to model the surface morphologies of G1 and G2. Yet since manual image matching is a rather tedious task, the frame of this study did not allow spending time on these locations.

Table 10 and 11 list the photogrammetric models of G4. Tables 12 through 20 itemize the GCPs used within these models. While a total of 42 GCPs of the type *multipoint transform* establish absolute orientations, 15 *check point* type GCPs serve to validate the results of both recording sessions. It is conclusive that the *multipoint transform* model coordinates differ on average only 2.5 cm ($Q_1 = 1.3$, $Q_3 = 3.1$) from the surveyed points, while for the validation coordinates this measure is 4.3 cm ($Q_1 = 2.5$, $Q_3 = 5.8$). Figure 25 illustrates the residuals for each recording session respectively.

Table 21 and 22 list point cloud properties respectively for S2 and S3. The lists reveal the effect of TGEL-based point thinning (see 4.3.2) on the data load. Figure 26 maps two levels of data reduction and qualitatively visualizes the change in resulting terrain surface models. In the right map, negative values (dark) show that the gully depth modelled with low resolution data is less than the depth modelled with a TGEL of $0.02m$. Bright and very dark regions at break lines (see inset map in figure 26) therefore stress errors from the interpolation of too sparse point clouds.

Section 4.3.3 describes the qualitative approach to assess the impact of point cloud densities. It uses the coordinate Z-value RMSE measure. Figure 27 depicts the relationship between this measure and point data densities. It is important to notice that when addressing performance issues, the use of thinning algorithms has different effects than the use of lower sampling intervals in the DSM generation process. Already sparsely sampled DSM point clouds most likely contain different points than a thinning algorithm preserves from a dense point cloud. The thinning tool in this study provides no control e.g. to align cell edges with break lines. There is also no information if cells include areas with bare soil or (higher) vegetation only. If

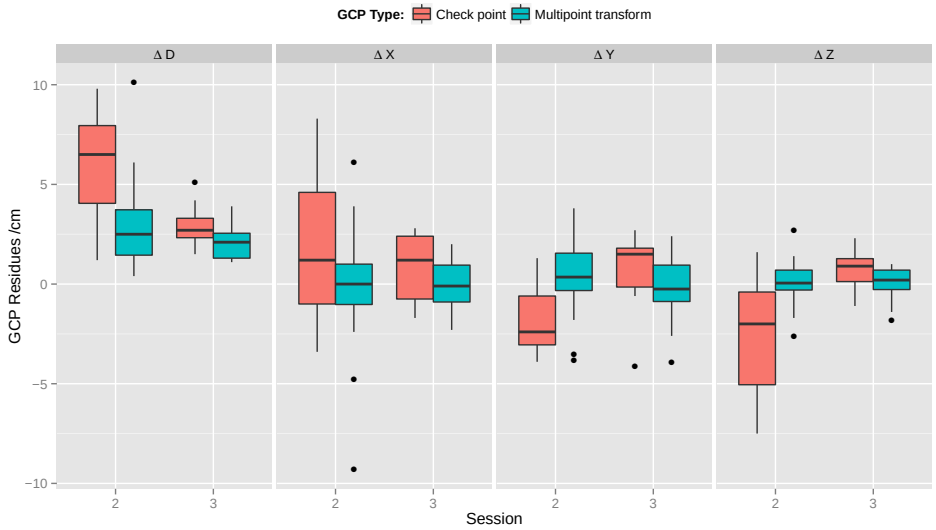

Figure (25) Boxplot of modelled and surveyed GCP coordinate residuals.

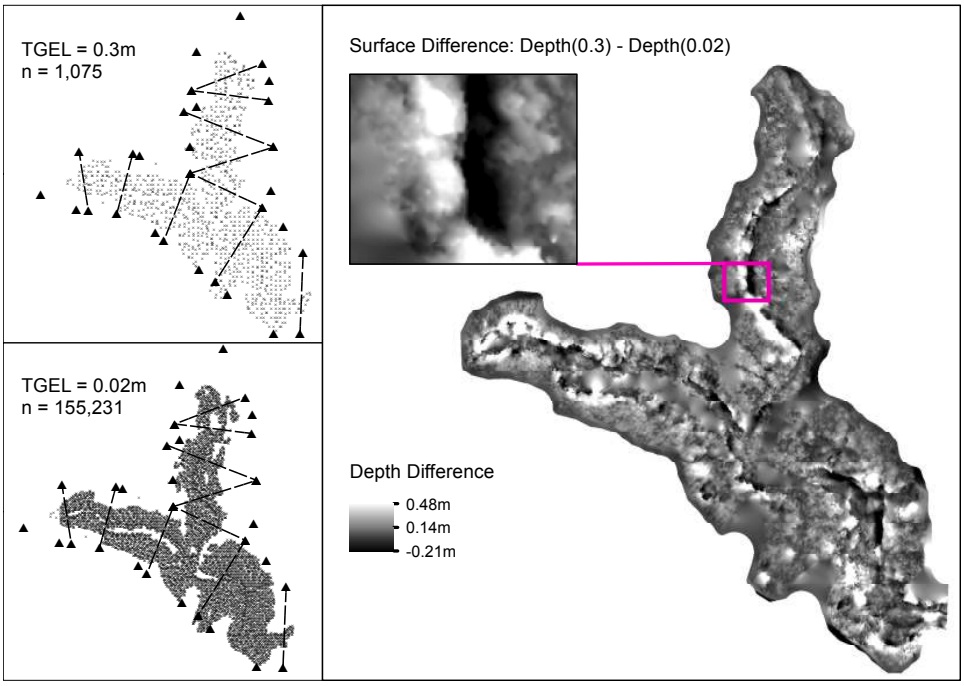

Figure (26) Visualisation of different surface point densities as a result of changing thinning parameters.

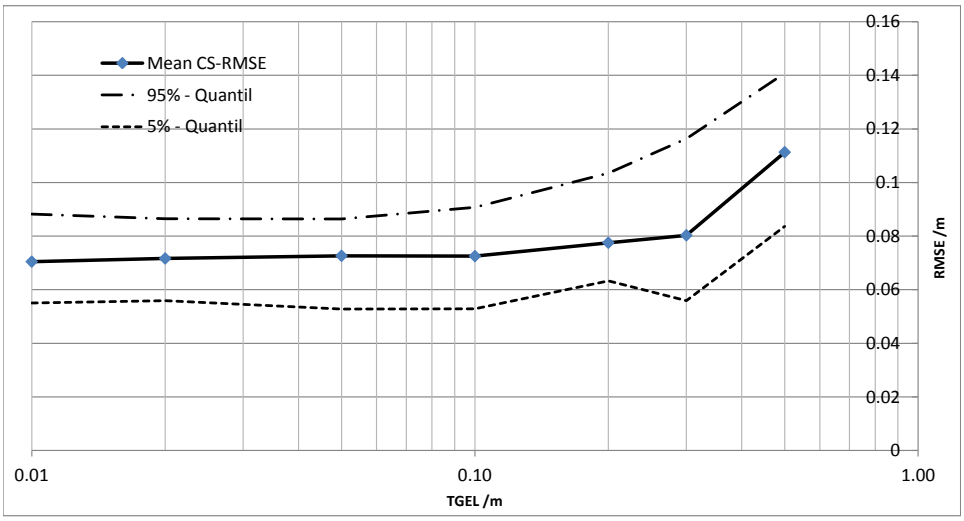

Figure (27) The RMSE over the thinning grid edge length (log-scaled).

pare soil points prevail in a cell, the algorithm preserves these coordinates due to their low elevation. For the same cell, a large DSM sampling interval might contain other real world features than the soil surface coordinate. The functional relation of RMSE and TGEL (figure 27) therefore depends on the existence and pattern of e.g. bare soil features.

5.2 Method Comparison

The following subsections condense information about G4 and compare point, area and volume results from plumb line and photogrammetric measurements. It is important to note that in this study PL-measurements generally form the reference data. One must keep in mind that PL data is likely to misrepresent true surface CS. As a result, it is not possible to rank the two methods with respect to their result accuracy. In this respect terms such as *over-* or *underestimation* are somewhat misleading. Nevertheless the following sections use such vocabulary to describe the CRP based coordinate datasets. Evaluating the accordance of coordinate elevations is more based on the residuals RSME value than on the Pearson-coefficient. However, plots in the appendix of this study do incorporate figures for the latter statistical measure.
Focusing on certain regions within the domain of the G4 investigation site outlines deficient photo acquisition. Exclusion of these potentially avoidable flawed sections seeks to support the validity of derived measures.

5.2.1 Cross-Section Coordinates

As section 4.3.3 describes, this study uses elevation residues between PL- and CRP-measured CS-vertices to validate the consistency between terrestrial CRP and manual PL-measurement results. Here, a good starting point is to examine scatter-plots of CRP- over PL-elevations on a session and CS basis. In such plots, the distance between data points and a line of perfect linear relationship between the two elevation variables, represents the residuals.

Incorporating graphs for the recording session two, figure 45 reveals i.a. inconsistent elevations for CS19 and high residuals for CS15. At CS16, CS17, CS22 and CS23 the CRP-method almost consistently overestimates the elevation with the residues of CS23 being rather high. Note that CS23 lies in a region with shrubby gully wall and bank vegetation.
A underestimation prevails for CS18 and CS24. In both cases, higher residuals are given in the lower part of the CS or, in other words, at the gully sole. At CS20 and CS21 the residues are rather normally distributed around a mean of $-2.6\ cm$ ($Q_1 = -5.4$, $Q_3 = -0.3$) and $-0.2\ cm$ ($Q_1 = -2.8$, $Q_3 = 3.1$) respectively. For session three, all graphs except the ones for CS16, CS20 and CS21 in figure 46 show a smaller RMSE of the surface coordinate Z-values. Eye-catching are the large residues of CS23 ($RMSE = 36\ cm$) and in addition, those of CS21 with a RSME of 7.9 cm which was 4.4 cm in the previous session. The outliers visible for CS19 of session two are not present in the session three comparison and the original RMSE decreases from 20.9 cm in S2 to 9.4 cm in S3. A closer examination of CS19 CRP data shows, that coordinate interpolation errors result from sparse or non existent data.

In order to minimize the impact of (avoidable) deficient data acquisition, it seems valid to exclude erroneous data when calculating overall quality measures. For the orographic left hand side of CS19 (S2) or CS21 (S3), figure 47 and 48 show significant discrepancies in the elevations of PL and CRP data. These discrepancies are clearly attributable to a flawed method set-up as section 6 further examines. It is arguable whether it's valid to exclude CS23 (S2 & S3), the cross-section where the worst congruence between PL and CRP measurements prevails. Nevertheless, RMSEs calculations which incorporate all measurements of G4 exclude these CSs. The plots in figure 30 comprise all elevation data except the aforementioned ones. As the CRP data of CS21 is erroneous at session three only, it is not valid to directly compare the overall RMSE values of 8.1 cm for session two and 7.1 cm for session three. Removing CS21 from the session two dataset as well, results in a RMSE of 8.6 cm.

Figure 28 condenses statistic residual data in CS- and session-specific box-plot diagrams. Figure 29, as well as the CS-specific scatter-plots (see

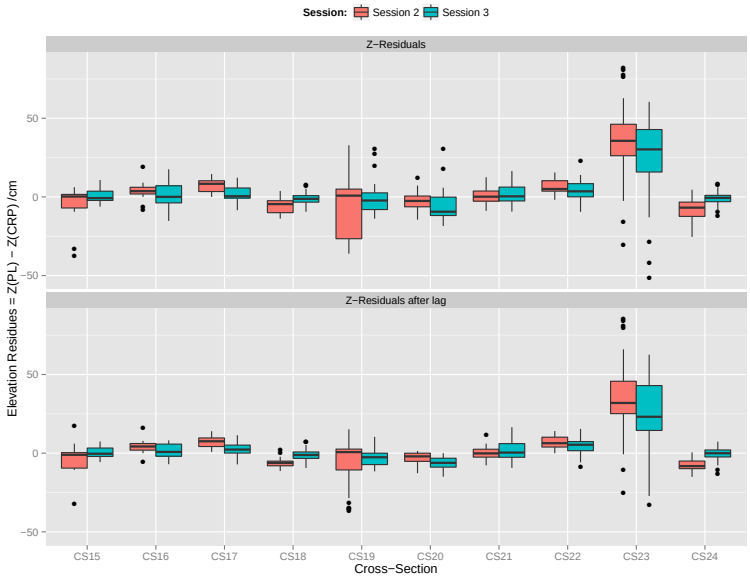

Figure (28) Boxplot of the CS specific residuals between PL and CRP coordinate elevations.

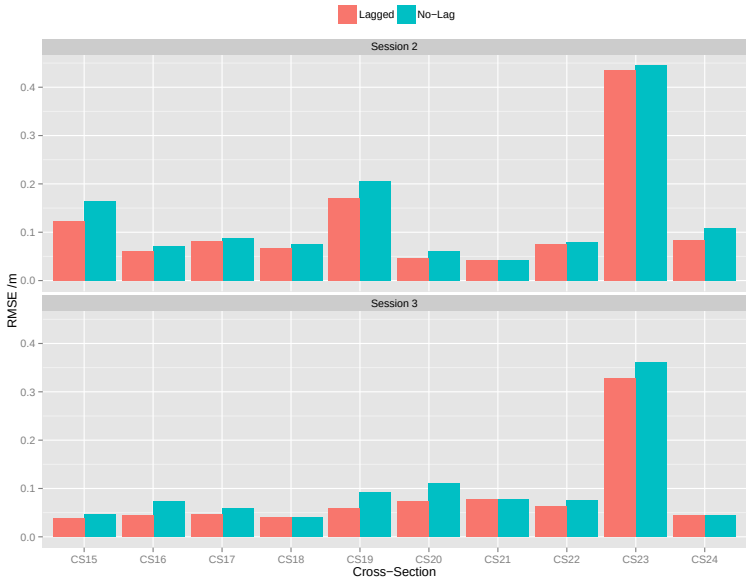

Figure (29) Barplot of the CS specific RMSE measure contrasting results for lagged and non-lagged CSs.

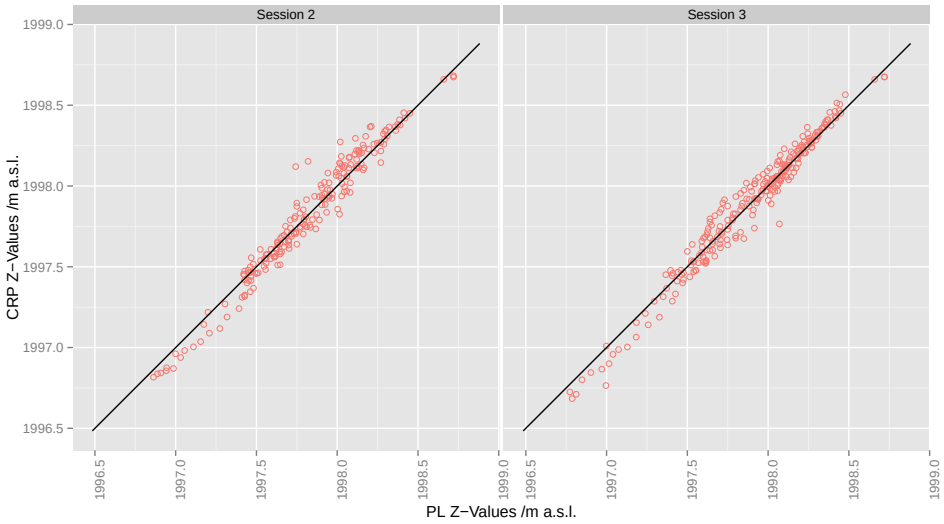

Figure (30) Scatter-plot CRP over PL coordinate elevations of selected CS of G4.

7.3), include yet another measure. It is the residual analysis of horizontally shifted (or lagged, see 4.3.3) PL- and CRP-based cross-sections. Figure 29 contrasts the RMSE results of shifted, and non-shifted CRP-data for each CS.

5.2.2 Cross-Section Areas and Gully Volumes

Table 5 incorporates PL area and volume geometry results of G4. Table 4 comprises the geometry analysis based on CRP with additional columns for volume extracts on the basis of DSM data existence (see 4.3.3).

Most CSs show increasing areas when comparing a previous with a following field-session. Exceptions are CS17, CS21 and CS23 of the PL-dataset for S1 and S2, where the area decreases by 3.7%, 3.4% and 0.2% respectively. In the CRP-results one can observe a decent decrease of 1.6% at CS20 and 5.6% at CS23.
Only in between S2 and S3 data is available for both methods. Within this time span, the PL-CS-areas increase on average by 11.3% (3.1% at minimum, 26.6% at maximum) while the CRP-based areas enlarge on average by 21.1% with a minimum and maximum growth rate of -5.6% and $118,6\%$ respectively. Subsuming the CS-area changes between S2 and S3 results in additional 1.93 m^2 for the PL-data, and additional 1.60 m^2 for the CRP-data.

A steady increase in volume prevails for all zones with two exceptions. According to the CRP-Data, the volumes of the gully sections between CS16 and CS18, as well as between CS22 and CS23 decrease slightly. Further-

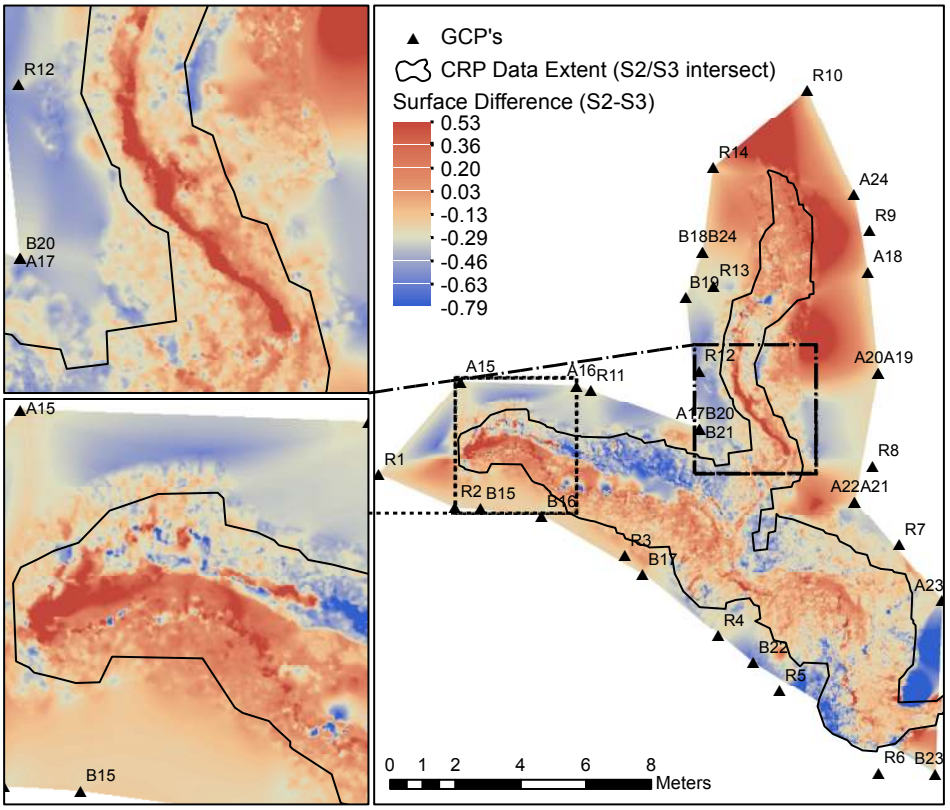

Figure (31) G4 Map illustrating erosion and deposition zones occurring in the time-span S1-S2. Reddish areas indicate erosion, blue areas deposition of soil.

more, with respect to this dataset the GCPs confined volume increases from 50.38 m^3 at S2 to 54.2 m^3 at S3. This equals an increase of 7.6%. For the same time span, the PL-measurements attest an increase from 39.5 m^3 to 44.7 m^3 or 13.3%.

The volumes one can observe for the zones with DSM surface data available are of course comparably smaller than the aforementioned ones. Surprisingly, also the percentage increase of 4.4% is significantly smaller than the one resulting for the whole gully plot-area. Considering the GCP and DSM extent plot areas of respectively 136.9 m^2 and 62.5 m^2 the specific volumetric soil loss calculates to 2.78 m^3/m^2 and 2.38 m^3/m^2. On the basis of PL-data, the specific volumetric soil loss between S2 and S3 is 3.83 m^3/m^2.

5.3 Case Study Results

The CRP approach allows a detailed analysis of the morphological changes G4 experienced during the period S2-S3. Figure 31 is the result of subtracting the S3- from the S2-surface model elevation values. The map shows

Table 4: G4 geometrical cross-section areas and volumes (for different ground plots) as a result from photogrammetric measurements

Location	**Area**		**Volume (GCP)**		**Volume (DSM)**	
CS	S2	S3	S2	S3	S2	S3
-	m^2	m^2	m^3	m^3	m^3	m^3
CS15	0.76	0.91	0.79	0.84	0.13	0.16
CS16	1.09	1.10	2.71	2.96	1.89	2.18
CS17	1.57	1.57	4.91	4.83	4.28	4.24
CS18	1.10	1.47	0.98	1.72	0.57	0.77
CS19	1.58	2.14	2.34	3.26	1.22	1.38
CS20	1.86	1.83	3.34	3.64	1.24	1.36
CS21	1.72	1.85	3.61	3.69	0.99	1.12
CS22	2.60	2.65	11.55	11.84	9.62	9.86
CS23	5.70	5.38	18.59	18.40	14.68	14.94
CS24	0.58	1.26	1.56	3.02	0.33	0.46
Σ	17.98	18.90	50.38	54.18	34.97	36.46

Table 5: G4's geometrical cross-section areas and volumes as a result from plumb line measurements

Location	**Area**			**Volume**		
CS	S1	S2	S3	S1	S2	S3
-	m^2	m^2	m^2	m^3	m^3	m^3
CS15	0.71	0.96	0.99	0.03	0.06	0.07
CS16	0.84	1.03	1.16	1.54	2.01	2.14
CS17	1.34	1.29	1.47	3.53	4.08	4.51
CS18	1.33	1.41	1.57	0.17	1.20	1.46
CS19	1.95	2.12	2.36	2.63	3.56	4.08
CS20	1.91	2.01	2.24	3.62	3.88	4.33
CS21	1.77	1.71	1.81	3.78	3.93	4.35
CS22	2.25	2.35	2.58	6.91	7.14	7.99
CS23	4.09	4.08	4.37	13.12	13.32	14.55
CS24	0.00	1.28	1.62	0.00	0.29	1.25
Σ	16.18	18.23	20.18	35.19	39.48	44.73

Table 6: G1's geometrical cross-section areas and volumes as a result of plumb line measurements

Location	**Area**			**Volume**		
CS	S1	S2	S3	S1	S2	S3
-	m^2	m^2	m^2	m^3	m^3	m^3
CS1	2.0	3.78	4.35	0.76	1.64	2.07
CS2	2.1	3.14	3.48	3.80	6.74	7.66
CS3	3.7	4.14	4.64	8.94	12.86	14.44
CS4	4.8	5.42	5.54	5.94	7.00	7.60
Σ	12.6	16.48	18.01	19.44	28.23	31.77

several regions where erosion led to lower elevations but also spots within and especially at the banks of the gully where a higher elevation prevails at S3. Continuous or scattered (higher) vegetation, deposition of soil and large stones are reasons for the latter. Significant erosion is visible at both gully head regions. The lower inset map of figure 31 exemplary visualises the G4.1 head region. The lower inset map in figure 31 illustrates the erosion process at a cut bank like gully feature. CS20 transects the incision in this area, but it is comparatively difficult to capture the bank erosion process extent with the CS-graphs in figure 62.

Since no CRP-data exists for G1, G2 and G3, the assessment of gully erosion in the Aba Kaloye catchment must rest on the data acquired with the plumb line method. After a first review of field protocols it was found that the PL recording set-up was not adequate for the situation at G3. Especially the dense vegetation obstructed a vertical arrangement of the measurement tape and furthermore it was difficult to determine the exact position of the CSs for each session. As a result, this study does not include the analysis of this reach. However, high erosion rates are not likely for this reach — erosion already cut deep into a rather sturdy C-horizon or bedrock material — and it is crucial to realize that only three gully reaches with a total length of approximately 47 m are under investigation. Evaluating these areas under investigation at G1, G2 and G4 leads to the results table 6, 7 and 5 list.

The previous section 5.2.2 examines the variables volume and CS-area of G4. Figure 32 and 33 illustrate the percentual changes in area and volume for each CS or inter-CS section (see section 4.3.1). When examining this data one should keep in mind that CS1 through CS4 describe G1, CS5 through CS8 belong to G2 and the remainder is attributable to G4.

Table 7: G2's geometrical cross-section areas and volumes as a result of plumb line measurements

Location	**Area**			**Volume**		
CS	S1	S2	S3	S1	S2	S3
-	m^2	m^2	m^2	m^3	m^3	m^3
CS5	3.03	4.93	4.92	1.09	1.93	2.15
CS6	4.55	5.03	5.26	4.43	6.21	6.30
CS7	3.35	3.64	3.63	11.52	13.87	14.19
CS8	5.98	5.92	6.16	25.84	27.34	28.02
Σ	16.91	19.52	19.97	42.88	49.36	50.66

5.3.1 Cross-Section Areas

Within the reaches G1 and G2 area and volumetric changes clearly appear stronger in the top regions of a particular reach. In fact, the topmost CS-area of G1 more than doubles in total (119% growth). It is therefore off the scale in figure 32. At many CSs, the better part of the area increase takes place within the first time-interval S1-S2. While covering a span 1.6 times longer than the second period (27 days), 1.9 times more soil volume is lost in the first time frame (42 days). More intensive erosion in the first period is especially present at the CSs close to the gully head such as CS1, CS2, CS5 and CS15. The latter belongs to G4, which in the top regions comprises ephemeral gully attributes. In comparison to G2 and G1, at the G4 site it is more difficult to find a pattern which relates the CS-area development to the CS-position within the gully reach.

The negative area-growth of CS17 between S1 and S2 is at least partially attributable to deficient data collection of the left hand side gully bank at S2. Figure 59 reveals the erroneous interpolation of surface coordinates. The same is true for CS21. There, the outermost data points of session two and three result in an overestimating surface interpolation between the GCPs and the first and last data point.

5.3.2 Gully Volumes

According to the topographic survey, an area of 3.76 *ha* contributes to the surface incision of G1. An additional 8.19 *ha*, and therefore a total 11.95 *ha*, of agricultural- pasture- and rather steep shrub-land drains to the section of G2. At the lower and less steep part of the catchment, a cultivated area of only 0.15 *ha* contributes to the G4 research area. Nevertheless, at this

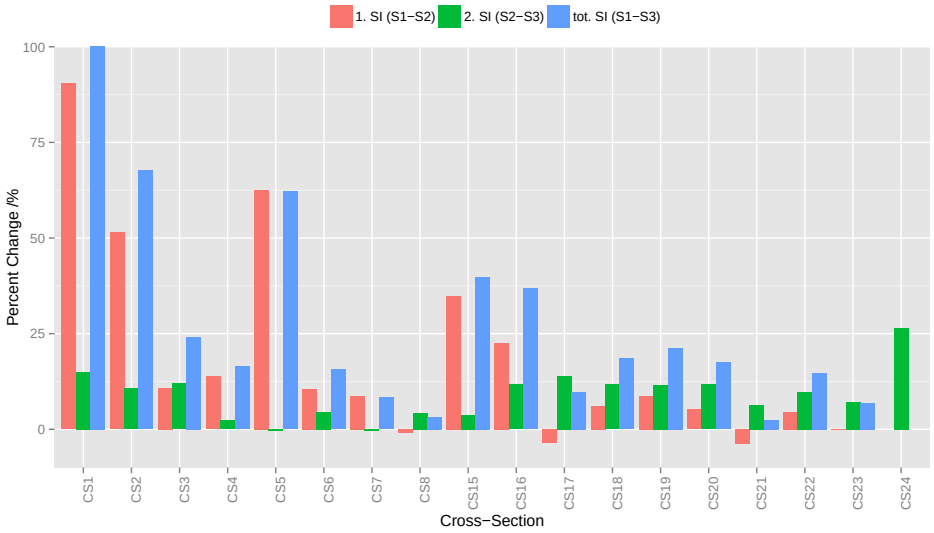

Figure (32) Barplot showing changes in the area between recording sessions for each CS in G1, G2 and G4 (PL-data)

location one can observe a total of 5.25 m^3 soil lost due to gullying over a length of approximately $27m$ in between S1 and S3.

At G1 and G2 the total soil loss during the whole period of consideration adds up to 12.32 m^3 and to 7.78 m^3 respectively. Table 8 condenses this information and incorporates figures, which relate the volumetric changes to gully reach lengths, as well as to the contributing areas. In order to calculate specific erosion rates in tons per unit length or area, it is necessary to assumes a bulk density for the soil. This parameter possesses a high spatial variability and samples do not exist for the areas under investigation. Nevertheless, a bulk density of $\rho_D = 1.2\ g/cm^3$ is a fairly conservative estimate in order to calculate the mass of eroded soil.

While it was difficult to recognise a distinct gully head at the northern branch of G4 (G4.2) especially at the beginning of the rainy season, a significant incision prevailed at all other locations. The extremely high headcut retreat of 4.05 m at G4.2 is at least partially attributable to the poor distinctiveness of the gully head. Table 9 comprises the gully head retreats for all locations.

Allocating gully erosion soil loss to runoff and sediment load data of the Abak Kaloye catchment is highly uncertain [Zehetbauer 2014, pp. 60,62]. Consistent data neither prevails for the time interval between S2 and S2, nor for the one between S2 and S3. However, for the first time-span, figure 34 shows that at least 15 rainfall events led to significant surface runoff in the gully system. Due to frequent malfunctions, the gauging station was not able to detect potentially high runoff events on seven days. Considering the

Table 8: Gully parameters investigated: reach length (L), contributing area (A) and total volume change per investigation are during the period of consideration (ΔV). Further specific erosion figures are the specific change in soil volume and mass per unit (gully) length and per unit contributing area (ΔV_L, ΔV_A, ΔM_L, ΔM_A)

Gully	L	A	ΔV	ΔV_L	ΔV_A	ΔM_L	ΔM_A
–	m	ha	m^3	m^3/m	m^3/ha	t/m	t/ha
G1	8.6	3.75	12.32	1.43	3.28	1.71	3.94
G2	12.0	11.94	7.78	0.65	0.65	0.78	0.78
G4	27.1	0.15	9.40	0.35	63.85	0.42	76.62

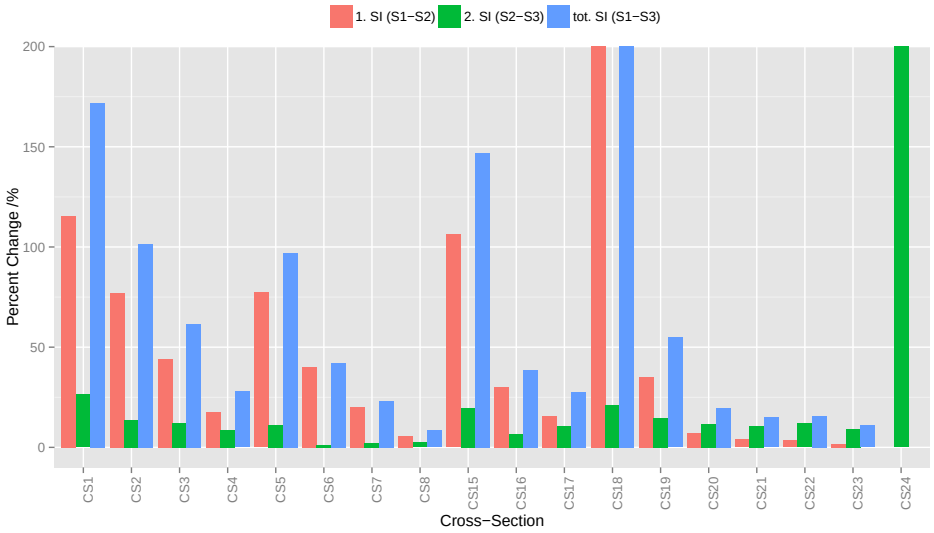

Figure (33) Barplot showing changes in volume between recording sessions for each inter-CS reach in G1, G2 and G4 (PL-data). The CS labels mark the lower margin of a volume.

Table 9: Distances between topmost CS and gully head (NPD)

Gully	S1	S2	S3
–	m	m	m
G1	1.53	1.73	1.9
G2	1.44	1.57	1.75
G4.1	0.17	0.26	0.3
G4.2	0.25	2.12	4.3

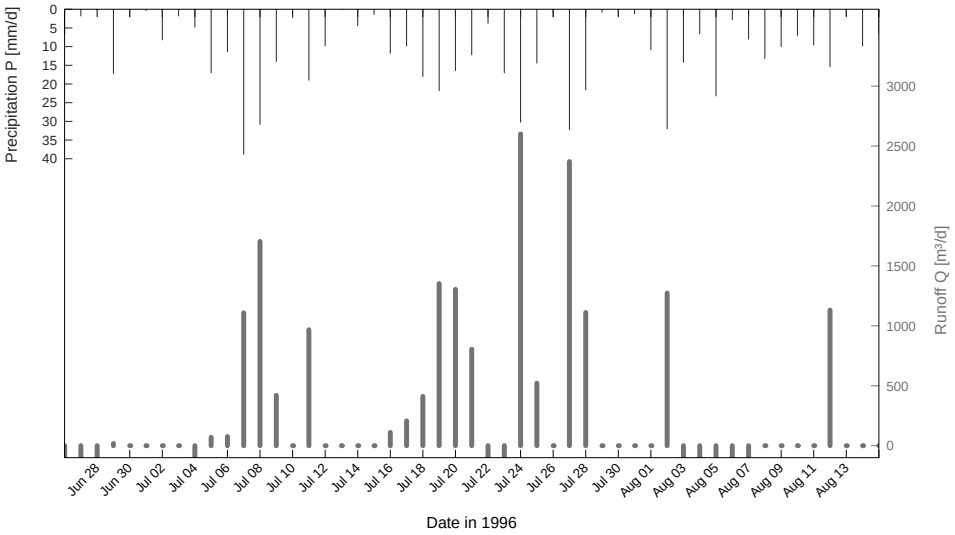

Figure (34) Rainfall and runoff events in the Aba Kaloye catchment. Runoff measurements at the gauging station shown in figure 10. Negative values represent missing data (Data: [Zehetbauer 2014, pp. 60,62]).

rainfall data there is a good chance that a surface runoff event occurred e.g. on August 5^{th}. Furthermore, Zehetbauer reports problems recording small runoff events at all. This means, that the runoff was less than a certain threshold for at least 10 days.

For the time in between S1 and S2, this study attributes a soil loss of 19.56 m^3 (23.47 t) to the gully reaches G1, G2 and G4. Within the same time frame, a sediment load of at least 435.47 t was recorded at the Aba Kaloye catchment outlet [Zehetbauer 2014, p. 63]. 5.3 % of total soil erosion is attributable to gullying under following premises: a) Besides the recorded gully erosion no further gullying occurred in any other part of the catchment and b) the aforementioned figure for the sediment load completely covers the periods sediment load. 5.3 % is a considerably low share and section 6 outlines the importance of more informed assumptions.

6 Conclusion

During this study, the development of a work-flow for assessment of gully morphological changes took place. It shows to some extent the capabilities of ground based photogrammetry to model terrain features such as the broad gully number four. Simultaneously it demonstrates the difficulties the CRP method involves:

- The photogrammetric process provides much space for mistakes due to its complexity. A synergy of hardware, software and an adequate data-recording approach is required to provide accurate results.
- Having begun the research with the goal of modelling four gully reaches at three points in time, the study ends up modelling one gully reach at two stages. Less then 200 out of 2000+ photos form the data basis for these two models. Time constraints in conjunction with tedious modelling processes is the limiting factor while the latter is at least partially the result of lacking user experience.
- The natural shape of erosion gullies, especially deep U-shaped incisions, imposed particular requirements on the recording strategy of photographs. This again expresses the need for qualified surveyors and a prudent ground control at the recording site. At the time being, this contradicts the idea of rapid data acquisition and processing and therefore potentially high temporal resolutions.
- The in-situ recording setup seems to be a key to expedited data processing. Tools like coded targets (GCPs) and on-the-job camera calibration already provide for additional image quality and potentially reduce processing efforts. Again this requires comprehensive knowledge of the whole modelling work-flow; a reason why this study did not make use of this capability. Recent and future developments in the photogrammetric field of Structure from Motion (SfM) accompanied by the continuing rise in computing power could potentially alleviate the need for professional qualities.

The prevailing approach uses CPs as a basis for the models absolute orientation accuracy estimations. The results also include the residuals of the models over-determined Helmert transformation parameters ('Multipoint Transform' GCPs). These residuals act as an indicator for the relative orientation quality of the CRP models. Compared to figures one can find in the literature, these figures are rather high. Reasons for such high model inaccuracies are a) the use of low-cost hardware, b) lacking experience in the modelling process and c) the comparatively sophisticated feature shape and the corresponding GCP set-up. The study therefore suggests an improved

recoding strategy, comprising of a better distribution of the ground control within the extent of a single model covering whole gully reaches.

In the prevailing study, the most prominent measure of accordance between the PL- and CRP-gathered surface data is the CS-coordinate elevations RMSE. On the CS level, it is possible to reveal at least two examples, for which incomplete CRP data results in a flawed representation of the surface (CS19/S2 and CS21/S3, see 5.2.1). Here, an improved image acquisition approach would avoid this outcome. At one location (CS23), shrub-vegetation undermines the establishment of good CS-representation based on CRP. This supports the conclusion that only gully reaches sparsely vegetated with higher plants are potential examination objects for automated DSM generation.

In comparison with the CS-residual analysis of S2, the S3 analysis gives a smaller overall RMSE and an almost consistently smaller RMSE for all CSs. Assuming the advancement of plant growth in the rainy season this suggests, that the vegetation on gully banks has less influence on the CRP models than the model set-up (photo acquisition, image selection for modelling and DSM-generation) itself. However, the CRP-model accuracy indicators (CPs and 'Multipoint Transform' GCPs) as well as livestock which keeps gully bank grass cover at a minimum, prohibits this proposition.

The CS area calculation for both data recording methods is deficient in a way, as the extent and density of available data strongly affects the CS-area results. In the case of PL-measurements, a possible solution is to enforce the recording of the outermost measurements being at a certain distance from the GCPs. Alternatively, CS-area calculations may include only those parts of the subsection, where data exists for all recording sessions.

For the assessment of gully erosion in the context of the case study, the study examines the volumetric soil loss at four gully reaches with a total length of approximately $47m$. Figures for CS-area changes and gully volume changes exists for the time intervals S1 through S2 and S2 through S3. These figures suggest increased erosion rates at the beginning of the rainy season.

An attempt to assess the share of gully erosion contributing the total erosion in the catchment is difficult. Three unknown factors necessitate the introduction of hypothetical scenarios. Assumptions are necessary for:

- Soil bulk density: Samples do not exist so an approximation of this soil parameter rests on the soil class and texture, as well as on the prevailing land use and tillage practices. An examination of this value is not part of this study but it uses the reasonable estimate of $1.2\ g/cm^3$ for an example scenario.

- The ratio of gully erosion that the measurements cover, compared to the total gully erosion in the catchment: That the research sites were

selected by the prevalence of active erosion does not mean that gullying does not occur in other parts of the drainage network. Considering that zones under investigation represent only a small share of the catchment's total channel system — in terms of longitudinal extent, 3.7% — it is unlikely that gully erosion only takes place at these reaches. Nevertheless, several photos of zones not under investigation allow a qualitative assessment of the gully erosion activity. Providing figures for this ratio is admittedly difficult, but for hypothetical scenarios this number may vary between 30% and 70%.

- Total soil erosion during the period of consideration: Gaps exist in the rainfall, runoff and sediment-load data [Zehetbauer 2014, pp. 41 sqq.] for the period between June 26^{th} and August 8^{th}. It is therefore necessary to make assumptions for this data, however considering the sample size for the variables *runoff* and *sediment load*, this is difficult. Here again it is possible to form variable scenarios: The measurements give the lower boundary of total sediment load. Sediment load models based on the rainfall data and runoff coefficients could provide the upper boundary. A high upper boundary leads to diminishing gully erosion ratios. Without undertaking any sort of regression analysis one may assume a maximum total unrecorded sediment load of 132 t for the sake of a hypothetical example scenario.

Using the reasonable (but purely hypothetical) aforementioned values, gullying accounts for 5.8% to 18% of total erosion. Once more, it is important to stress that these figures are based on a set of assumptions and on a temporal subset of erosion figures within a single rainy season.

References

Albertz, Joerg (May 2007). "A look back - 140 Years of "photogrammetry" - Some remarks on the history of photogrammetry". English. In: *Photogrammetric Engineering and Remote Sensing* 73.5. WOS:000246238800006, pp. 504–506. ISSN: 0099-1112.

American Society for Photogrammetry and Remote Sensing (2004). *Manual of photogrammetry*. 5th ed. Bethesda, Md: American Society for Photogrammetry and Remote Sensing. ISBN: 1570830711.

Anderson, K. and H. Croft (Jan. 2009). "Remote sensing of soil surface properties". en. In: *Progress in Physical Geography* 33.4, pp. 457–473. ISSN: 0309-1333, 1477-0296.

Baghdadi, N. et al. (Jan. 2002). "Potential of ERS and Radarsat data for surface roughness monitoring over bare agricultural fields: Application to catchments in Northern France". In: *International Journal of Remote Sensing* 23.17, pp. 3427–3442. ISSN: 0143-1161, 1366-5901.

Bartley, Rebecca et al. (2008). "Bank erosion and channel width change in a tropical catchment". en. In: *Earth Surface Processes and Landforms* 33.14, 2174–2200. ISSN: 1096-9837.

Bocco, G. (Dec. 1991). "Gully Erosion - Processes and Models". English. In: *Progress in Physical Geography* 15.4, pp. 392–406. ISSN: 0309-1333.

Brown, Lisa Gottesfeld (1992). "Survey of image registration techniques". English. In: *ACM Computing Surveys* 24.4, pp. 325–376. ISSN: 03600300.

Castillo, C. et al. (2012). "Comparing the Accuracy of Several Field Methods for Measuring Gully Erosion". In: *Soil Science Society of America Journal* 76.4, p. 1319. ISSN: 0361-5995.

Chandler, Jim (1999). "Effective application of automated digital photogrammetry for geomorphological research". en. In: *Earth Surface Processes and Landforms* 24.1, 51–63. ISSN: 1096-9837.

Daba, Shibru, Wolfgang Rieger, and Peter Strauss (Jan. 2003). "Assessment of gully erosion in eastern Ethiopia using photogrammetric techniques". In: *CATENA* 50.2–4, pp. 273–291. ISSN: 0341-8162.

Dixon, John (2001). *Farming systems and poverty: improving farmers' livelihoods in a changing world*. Rome : Washington, D.C: FAO ; World Bank. ISBN: 9251046271.

Esri (2014). *ArcGIS - Mapping and Spatial Analysis for Understanding Our World*. URL: `http://www.esri.com/software/arcgis` (visited on 02/05/2014).

Online. File:Amhara in Ethiopia.svg. URL: `http://en.wikipedia.org/wiki/File:Amhara_in_Ethiopia.svg` (visited on 03/10/2014).

Online. File:Ethiopia shaded relief map 1999, CIA.jpg. URL: `http://en.wikipedia.org/wiki/File:Ethiopia_shaded_relief_map_1999,_CIA.jpg` (visited on 03/10/2014).

Fonstad, Mark A. et al. (2013). "Topographic structure from motion: a new development in photogrammetric measurement". en. In: *Earth Surface Processes and Landforms* 38.4, 421–430. ISSN: 1096-9837.

Fox, J. F. and A. N. Papanicolaou (2008). "An un-mixing model to study watershed erosion processes". In: *Advances in Water Resources* 31.1, pp. 96–108. ISSN: 0309-1708.

Gardner, Thomas W., Kathryn F. Connors, and Haiyan Hu (Oct. 1989). "Extraction of fluvial networks from SPOT panchromatic data in a low relief, arid basin". In: *International Journal of Remote Sensing* 10.11, pp. 1789–1801. ISSN: 0143-1161, 1366-5901.

Giménez, R. et al. (2009). "Accuracy of high-resolution photogrammetric measurements of gullies with contrasting morphology". en. In: *Earth Surface Processes and Landforms* 34.14, 1915–1926. ISSN: 1096-9837.

Gissila, T. et al. (2004). "Seasonal forecasting of the Ethiopian summer rains". en. In: *International Journal of Climatology* 24.11, 1345–1358. ISSN: 1097-0088.

Grepperud, Sverre (Jan. 1996). "Population Pressure and Land Degradation: The Case of Ethiopia". In: *Journal of Environmental Economics and Management* 30.1, pp. 18–33. ISSN: 0095-0696.

Haregeweyn, N. et al. (2013). "Assessing the Performance of a Spatially Distributed Soil Erosion and Sediment Delivery Model (watem/Sedem) in Northern Ethiopia". In: *Land Degradation & Development* 24.2, 188–204. ISSN: 1099-145X.

Hughes, Michael L., Patricia F. McDowell, and W. Andrew Marcus (Mar. 2006). "Accuracy assessment of georectified aerial photographs: Implications for measuring lateral channel movement in a GIS". In: *Geomorphology* 74.1–4, pp. 1–16. ISSN: 0169-555X.

ICARDA. *Unlocking the potential of rainfed agriculture in Ethiopia for improved rural livelihoods Ongoing Research*. URL: `http://ongoing-research.cgiar.org/factsheets/unlocking-the-potential-of-rainfed-agriculture-in-ethiopia-for-improved-rural-livelihoods/` (visited on 12/02/2013).

Isenburg, Martin (2014a). *las2shp README.txt*. URL: `http://www.cs.unc.edu/~isenburg/lastools/download/las2shp_README.txt` (visited on 02/05/2014).

— (2014b). *lasthin README.txt*. URL: `http://www.cs.unc.edu/~isenburg/lastools/download/lasthin_README.txt` (visited on 02/05/2014).

— (2014c). *LAStools: converting, filtering, viewing, processing, and compressing LIDAR data in LAS format*. URL: `http://cs.unc.edu/~isenburg/lastools/` (visited on 02/05/2014).

— (2014d). *txt2las README.txt*. URL: `http://www.cs.unc.edu/~isenburg/lastools/download/txt2las_README.txt` (visited on 02/05/2014).

Jester, Werner and Andreas Klik (Dec. 2005). "Soil surface roughness measurement—methods, applicability, and surface representation". In: *CATENA* 64.2–3, pp. 174–192. ISSN: 0341-8162.

Jetten, Victor, Ad de Roo, and David Favis-Mortlock (Oct. 1999). "Evaluation of field-scale and catchment-scale soil erosion models". In: *CATENA* 37.3, pp. 521–541. ISSN: 0341-8162.

King, C. et al. (Aug. 2005a). "Remote-sensing data as an alternative input for the 'STREAM' runoff model". In: *CATENA* 62.2–3, pp. 125–135. ISSN: 0341-8162.

King, C. et al. (Aug. 2005b). "The application of remote-sensing data to monitoring and modelling of soil erosion". In: *CATENA* 62.2–3, pp. 79–93. ISSN: 0341-8162.

Krauer, J. (1988). *Rainfall, Erosivity & Isoerodent Map of Ethiopia*. Soil conservation research project. Research report. University of Berne, Switzerland ; The Ministry of Agriculture and Environmental Protection. Ethiopia ; The United Nations University.

Krause, A. K. et al. (Nov. 1, 2003). "Multi-parameter fingerprinting of sediment deposition in a small gullied catchment in SE Australia". In: *CATENA* 53.4, pp. 327–348. ISSN: 0341-8162.

Linder, Wilfried (2003). *Digital photogrammetry: theory and applications*. Berlin ; New York: Springer. ISBN: 3540008101.

Lowe, David G. (Nov. 2004). "Distinctive Image Features from Scale-Invariant Keypoints". en. In: *International Journal of Computer Vision* 60.2, pp. 91–110. ISSN: 0920-5691, 1573-1405.

Luhmann, Thomas (2002). *Nahbereichsphotogrammetrie in der Praxis: Beispiele und Problemlösungen*. German. Heidelberg: Wichmann. ISBN: 9783879073986.

Marzolff, I. and J. Poesen (Oct. 2009). "The potential of 3D gully monitoring with GIS using high-resolution aerial photography and a digital photogrammetry system". In: *Geomorphology* 111.1–2, pp. 48–60. ISSN: 0169-555X.

Mather, Paul M. (1999). *Computer processing of remotely-sensed images: an introduction*. 2nd ed. Chichester ; New York: Wiley. ISBN: 0471985503.

Mehammednur Seid, Nurhussen et al. (Oct. 23, 2013). "Soil-Landscape Modeling and Remote Sensing to Provide Spatial Representation of Soil Attributes for an Ethiopian Watershed". In: *Applied and Environmental Soil Science* 2013. ISSN: 1687-7667.

Merritt, W. S., R. A. Letcher, and A. J. Jakeman (Oct. 2003). "A review of erosion and sediment transport models". In: *Environmental Modelling & Software* 18.8, pp. 761–799. ISSN: 1364-8152.

Moran, M. Susan et al. (Feb. 2002). "Comparison of ERS-2 SAR and Landsat TM imagery for monitoring agricultural crop and soil conditions". In: *Remote Sensing of Environment* 79.2–3, pp. 243–252. ISSN: 0034-4257.

Morgan, R. P. C (2005). *Soil erosion and conservation*. English. Malden, MA: Blackwell Pub. ISBN: 1405117818 9781405117814.

Morgan, R. P. C and M. A Nearing (2011). *Handbook of erosion modelling*. Chichester, West Sussex, UK; Hoboken, NJ: Wiley-Blackwell. ISBN: 9781405190107 1405190108.

Nachtergaele, J. and J. Poesen (1999). "Assessment of soil losses by ephemeral gully erosion using high-altitude (stereo) aerial photographs". en. In: *Earth Surface Processes and Landforms* 24.8, 693–706. ISSN: 1096-9837.

Nardi, L., L. Campo, and M. Rinaldi (Oct. 2013). "Quantification of riverbank erosion and application in risk analysis". en. In: *Natural Hazards* 69.1, pp. 869–887. ISSN: 0921-030X, 1573-0840.

Newby, Paul R. T. (2012). "Photogrammetric Terminology: Second Edition". en. In: *The Photogrammetric Record* 27.139, 360–386. ISSN: 1477-9730.

Niethammer, U. et al. (Mar. 2012). "UAV-based remote sensing of the Super-Sauze landslide: Evaluation and results". In: *Engineering Geology* 128, pp. 2–11. ISSN: 0013-7952.

Nyssen, Jan, Jean Poesen, and Jozef Deckers (May 2009). "Land degradation and soil and water conservation in tropical highlands". In: *Soil and Tillage Research* 103.2, pp. 197–202. ISSN: 0167-1987.

Nyssen, Jan et al. (Feb. 2004). "Human impact on the environment in the Ethiopian and Eritrean highlands—a state of the art". In: *Earth-Science Reviews* 64.3, pp. 273–320. ISSN: 0012-8252.

Ottlé, C., D. Vidal-Madjar, and G. Girard (Feb. 1989). "Remote sensing applications to hydrological modeling". In: *Journal of Hydrology* 105.3-4, pp. 369–384. ISSN: 00221694.

Pimentel, David et al. (Feb. 1995). "Environmental and Economic Costs of Soil Erosion and Conservation Benefits". en. In: *Science* 267.5201. PMID: 17789193, pp. 1117–1123. ISSN: 0036-8075, 1095-9203.

Poesen, J et al. (2003). "Gully erosion and environmental change: importance and research needs". In: *CATENA* 50.2, pp. 91–133. ISSN: 0341-8162.

Rocca, F., C. Prati, and A. Ferretti. *An Overview of SAR Interferometry.*

Schmugge, Thomas J. et al. (Aug. 2002). "Remote sensing in hydrology". In: *Advances in Water Resources* 25.8–12, pp. 1367–1385. ISSN: 0309-1708.

Seleshi, Yilma and Ulrich Zanke (2004). "Recent changes in rainfall and rainy days in Ethiopia". en. In: *International Journal of Climatology* 24.8, 973–983. ISSN: 1097-0088.

Setegn, Shimelis G., Ragahavan Srinivasan, and Bijan Dargahi (2008). "Hydrological modelling in the Lake Tana Basin, Ethiopia using SWAT model". In: *The Open Hydrology Journal* 2.2008, 49–62.

Setegn, Shimelis G. et al. (2009). "Spatial delineation of soil erosion vulnerability in the Lake Tana Basin, Ethiopia". en. In: *Hydrological Processes* 23.26, 3738–3750. ISSN: 1099-1085.

Snavely, Noah, Steven M. Seitz, and Richard Szeliski (Nov. 2008). "Modeling the World from Internet Photo Collections". en. In: *International Journal of Computer Vision* 80.2, pp. 189–210. ISSN: 0920-5691, 1573-1405.

Soil Science Society of America (2008). *Glossary of soil science terms.* Madison, WI: Soil Science Society of America. ISBN: 9780891188513 0891188517.

Taconet, O. and V. Ciarletti (Mar. 2007). "Estimating soil roughness indices on a ridge-and-furrow surface using stereo photogrammetry". In: *Soil and Tillage Research* 93.1, pp. 64–76. ISSN: 0167-1987.

Tebourbi, R. et al. (2000). "Three-dimensional surface reconstruction by stereovision and soil roughness modeling". In: *Geoscience and Remote Sensing Symposium, 2000. Proceedings. IGARSS 2000. IEEE 2000 International*. Vol. 2, 791–793 vol.2.

The R Project for Statistical Computing (2006). URL: `http://www.r-project.org/` (visited on 02/05/2014).

Valentin, C., J. Poesen, and Yong Li (Oct. 31, 2005). "Gully erosion: Impacts, factors and control". In: *CATENA* 63.2, pp. 132–153. ISSN: 0341-8162.

Warner, William S. (June 1995). "Mapping a three-dimensional soil surface with hand-held 35 mm photography". In: *Soil and Tillage Research* 34, pp. 187–197. ISSN: 0167-1987.

Zachar, Dušan (1982). *Soil erosion*. Developments in soil science 10. Amsterdam ; New York: Elsevier Scientific Pub. Co. : distribution for the U.S.A. and Canada, Elsevier North-Holland, Inc, pp. 47–64. ISBN: 0444997253.

Zehetbauer, Ingrid (2014). "The Paradox of Overfitting". MA thesis. University of Applied Life Science, BOKU Vienna.

Zitová, Barbara and Jan Flusser (Oct. 2003). "Image registration methods: a survey". In: *Image and Vision Computing* 21.11, pp. 977–1000. ISSN: 0262-8856.

7 Appendices

7.1 Gully Reaches Photographs

Figure (35) Gully 1 (S1) looking in flow direction

Figure (36) Gully 1 (S1) from orographic right hand side gully bank

Figure (37) Gully 2 (S2) looking in direction of flow

Figure (38) Gully 2 (S2) head cut from orographic right hand side gully bank

Figure (39) Gully 3 (S2) almost not visible from the orographic left hand side

Figure (40) Gully 3 (S2) - taking photographs from 'inside'

Figure (41) Gully 4 (S1)

Figure (42) Gully 4 (S1)

Figure (43) Gully 4 (S2)

7.2 Gully Sections Not Under Investigation

(a) Part of the drainage network just above the outlet gauge looking towards flow direction

(b) Part of the drainage network in between G1 and G2

Figure (44) Most parts of the drainage network which are not under investigation do not show significant gullying activities or seem to be stabilized.

7.3 CS-Elevation Scatter-Plots

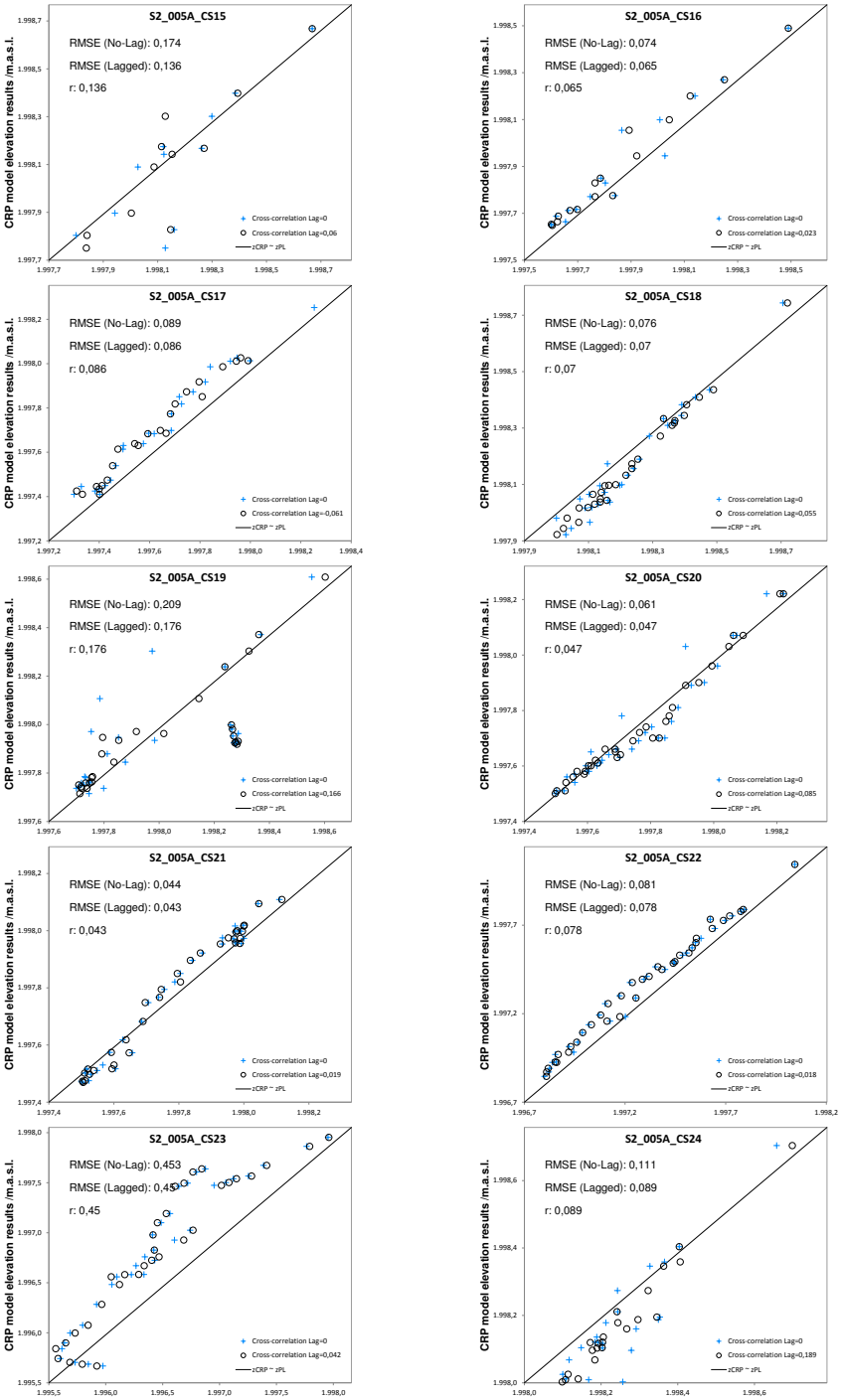

Figure (45) Scatterplots of photogrammetric over the plumb line measured coordinate elevations for each cross-section of gully for at session 2. Each plot includes the root mean square error and the Pearson coefficient of the two variables.

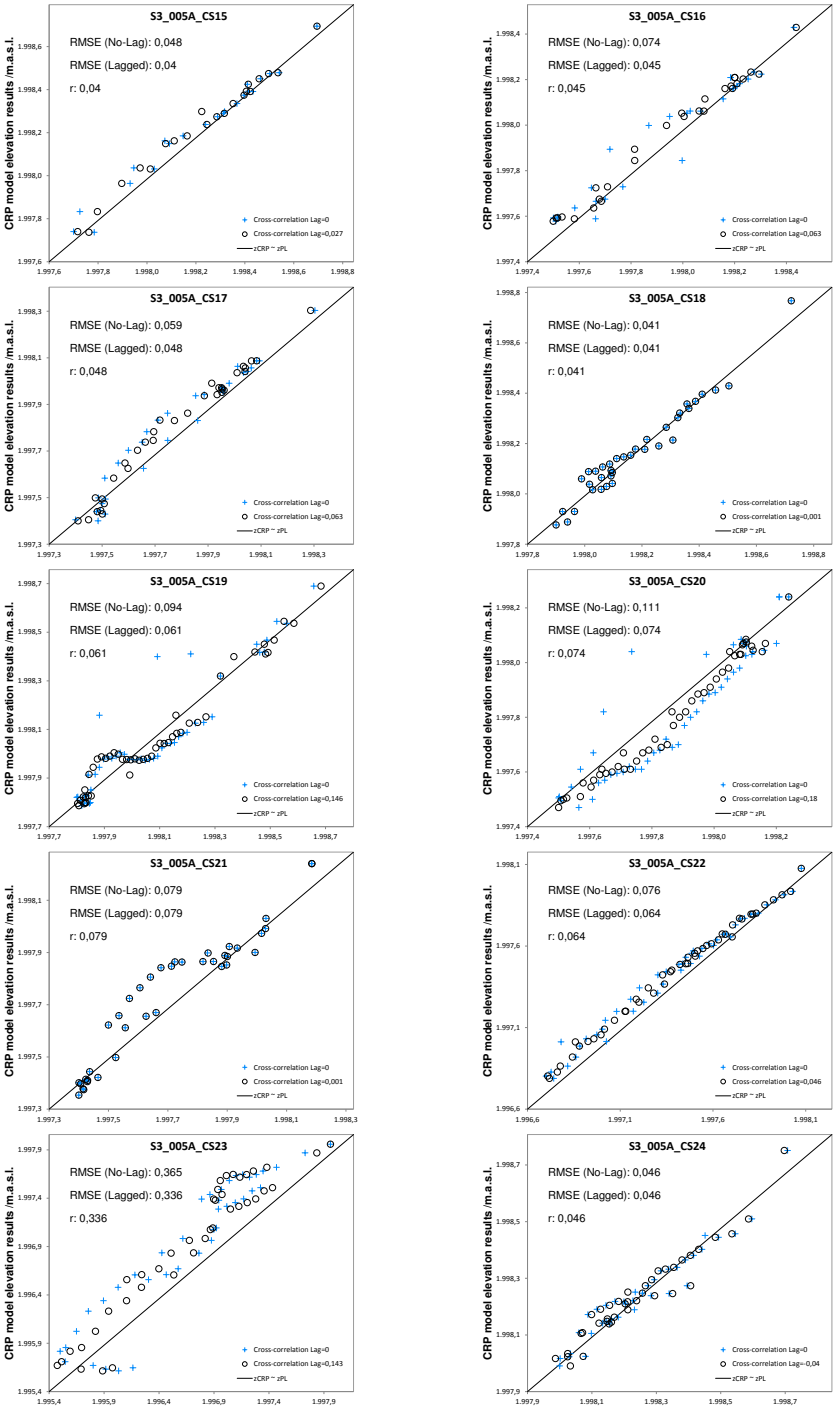

Figure (46) Scatterplots of photogrammetric over the plumb line measured coordinate elevations for each cross-section of gully for at session 3. Each plot includes the root mean square error and the Pearson coefficient of the two variables.

7.4 CS-Comparison Graphs

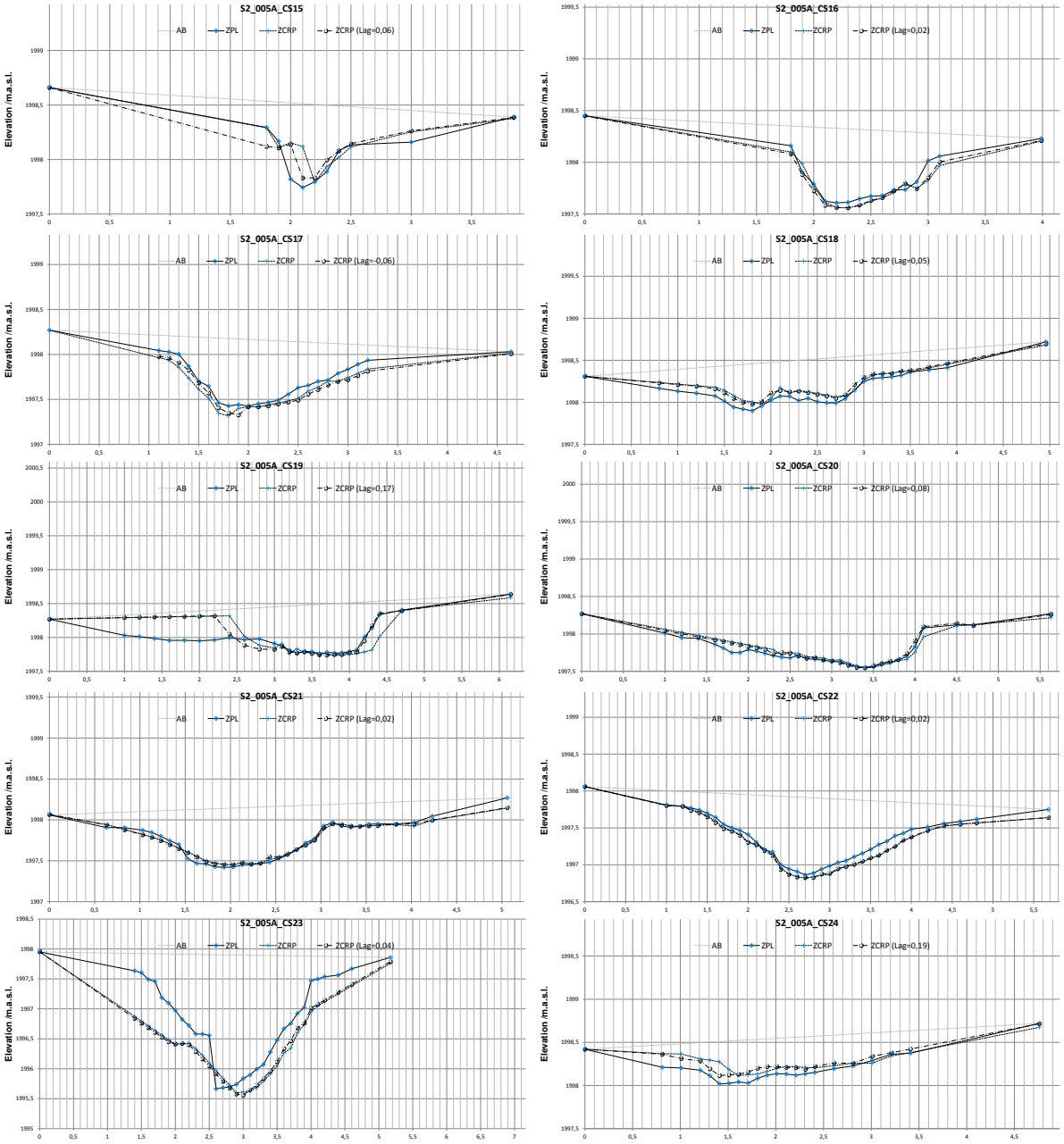

Figure (47) Cross section plumb line and photogrammetric (CRP measurements at gully number four, recording session 2. The horizontal offset of the second CRP graph aims to minimize the RMS error between CRP and plumb line measurements.

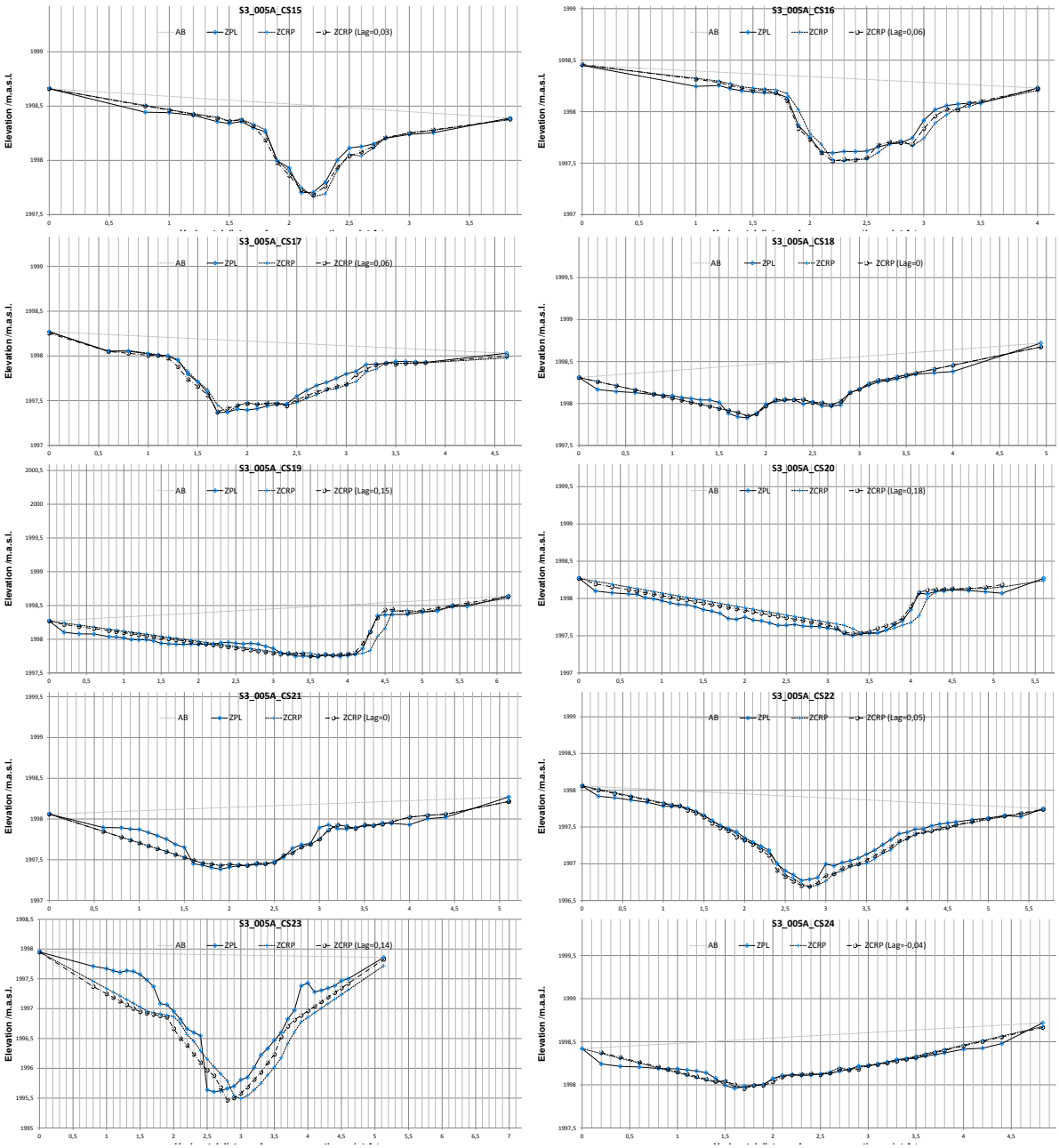

Figure (48) Cross section plumb line and photogrammetric (CRP measurements at gully number four, recording session 3. The horizontal offset of the second CRP graph aims to minimize the RMS error between CRP and plumb line measurements.

7.5 CS Session Comparison Graphs

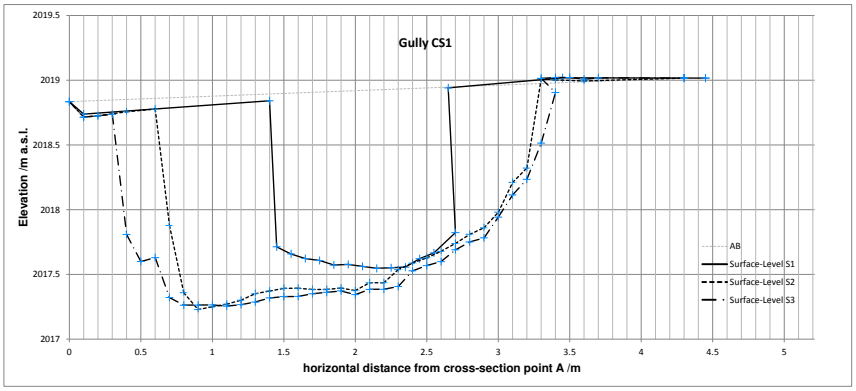

Figure (49) Gully CS1 shape plumb line survey results.

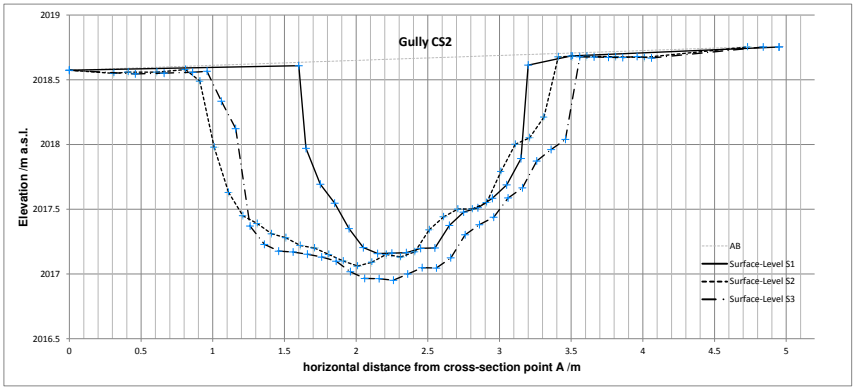

Figure (50) Gully CS2 shape plumb line survey results.

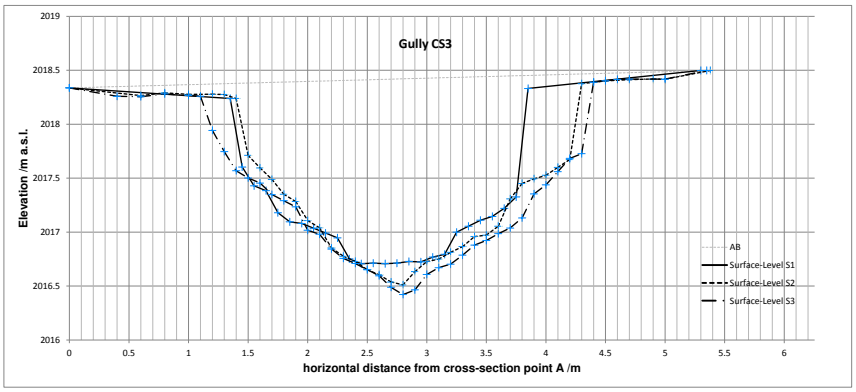

Figure (51) Gully CS3 shape plumb line survey results.

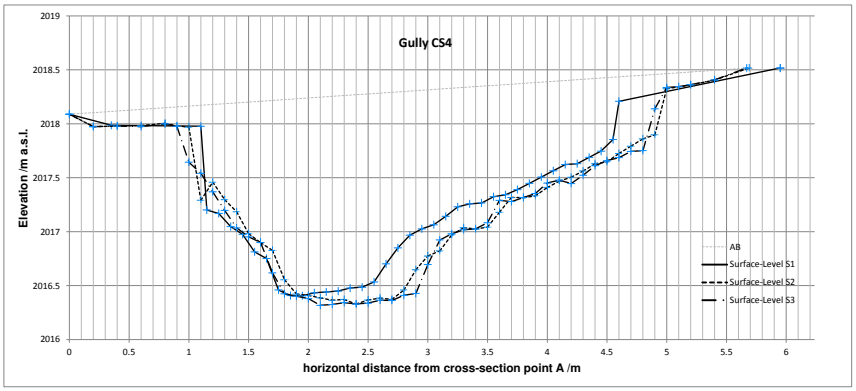

Figure (52) Gully CS4 shape plumb line survey results.

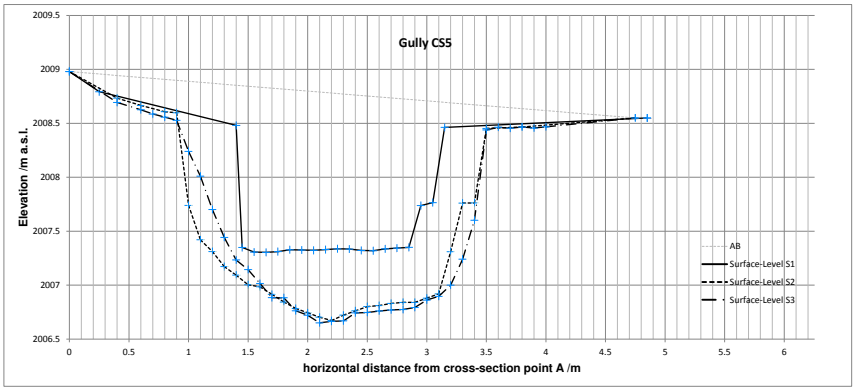

Figure (53) Gully CS5 shape plumb line survey results.

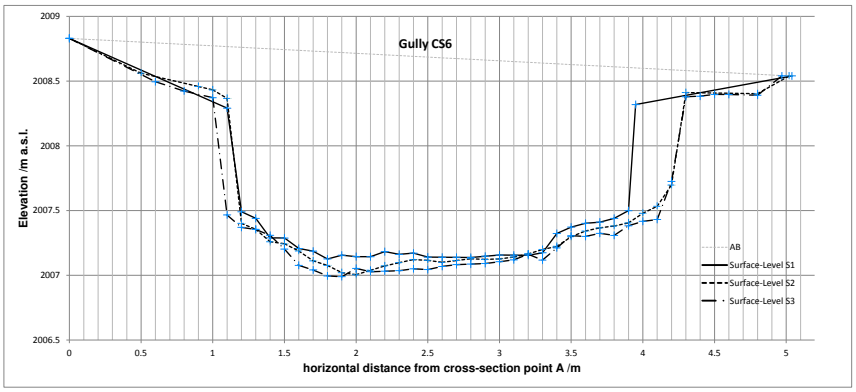

Figure (54) Gully CS6 shape plumb line survey results.

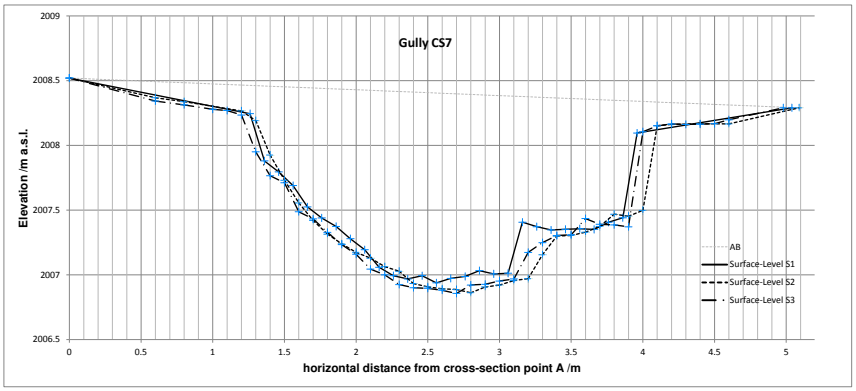

Figure (55) Gully CS7 shape plumb line survey results.

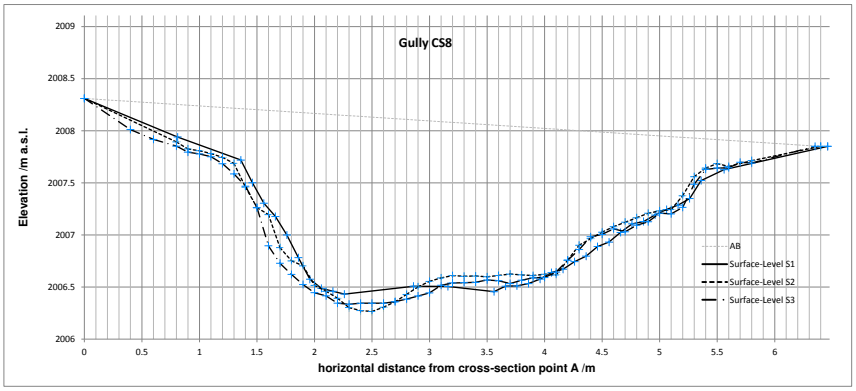

Figure (56) Gully CS8 shape plumb line survey results.

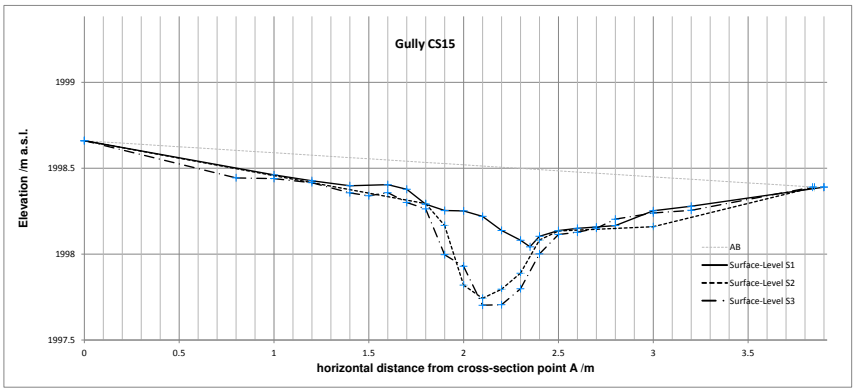

Figure (57) Gully CS15 shape plumb line survey results.

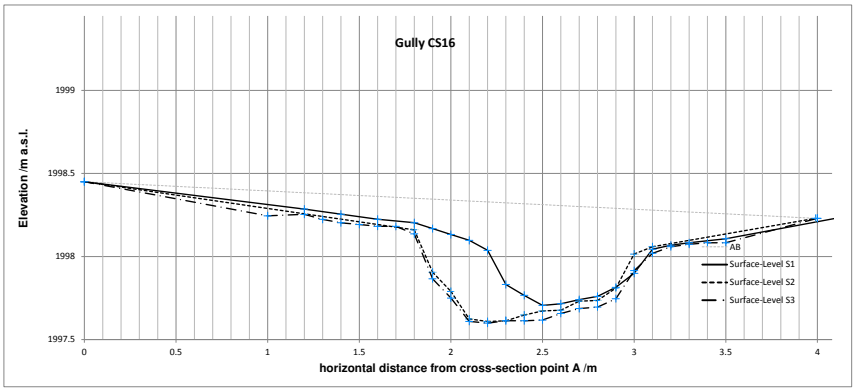

Figure (58) Gully CS16 shape plumb line survey results.

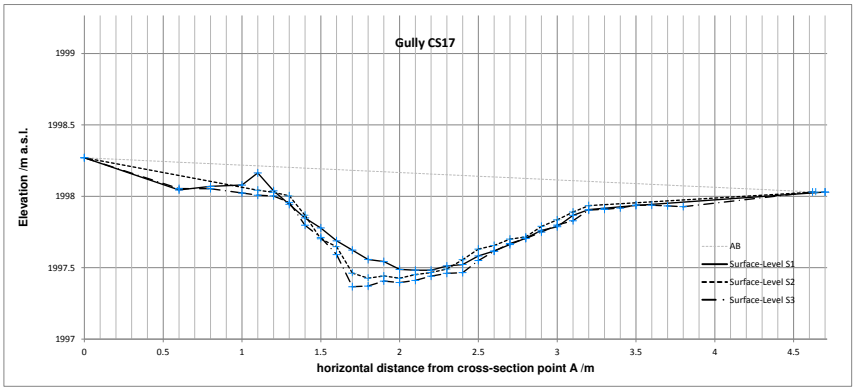

Figure (59) Gully CS17 shape plumb line survey results.

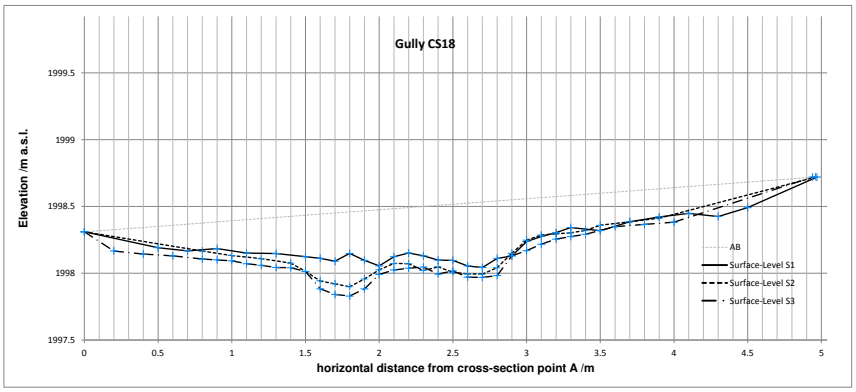

Figure (60) Gully CS18 shape plumb line survey results.

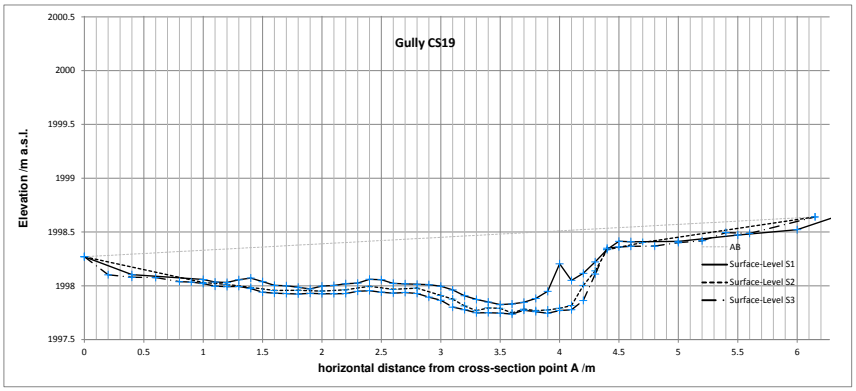

Figure (61) Gully CS19 shape plumb line survey results.

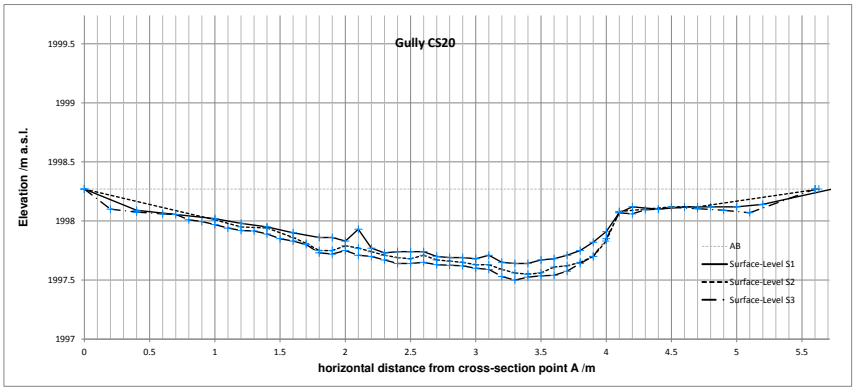

Figure (62) Gully CS20 shape plumb line survey results.

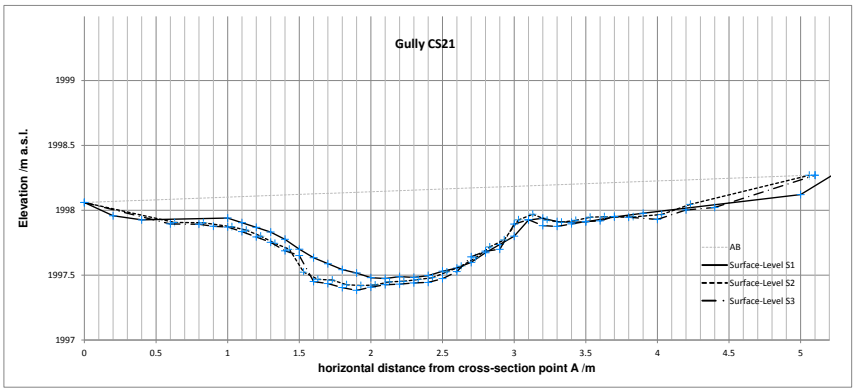

Figure (63) Gully CS21 shape plumb line survey results.

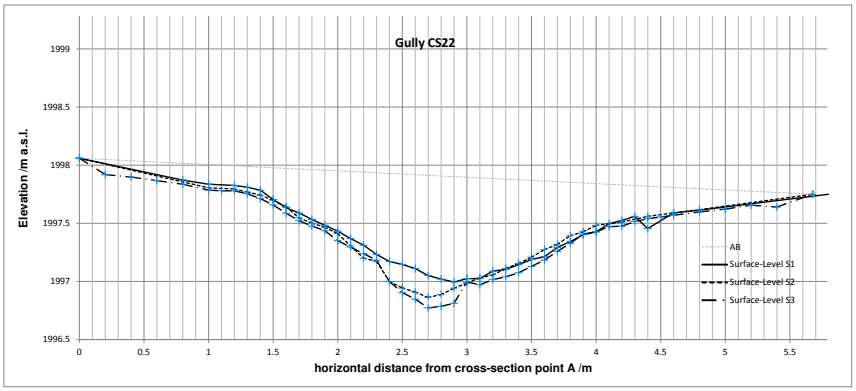

Figure (64) Gully CS22 shape plumb line survey results.

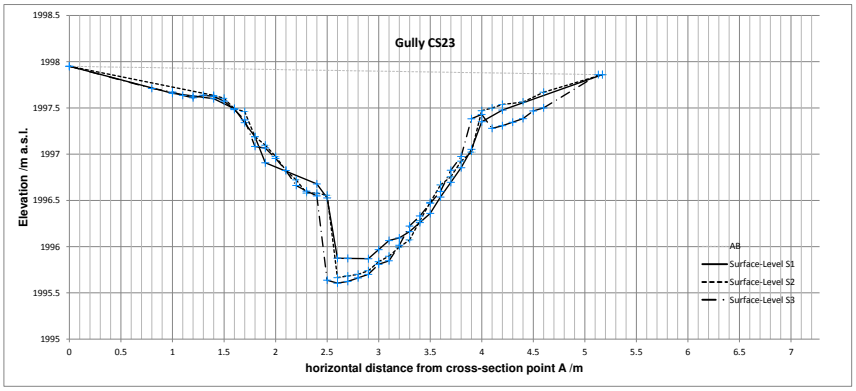

Figure (65) Gully CS23 shape plumb line survey results.

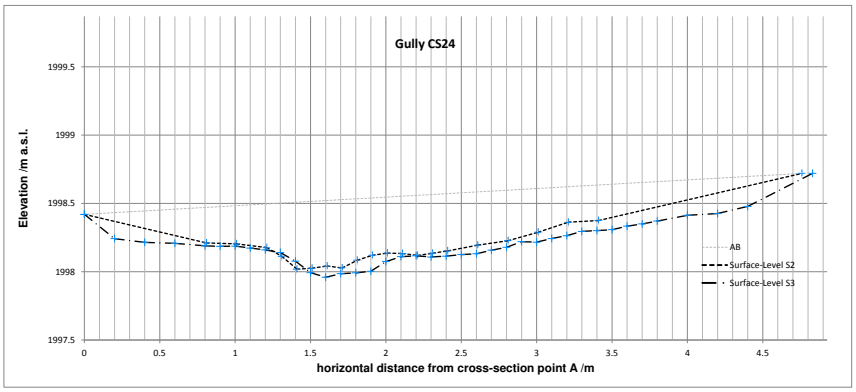

Figure (66) Gully CS24 shape plumb line survey results.

7.6 Tables

7.6.1 Photogrammetric Models - Overview

Following tables list all photogrammetric models of G4 at recording session number 2 and three respectively. The overall point RMS is provided in pixel units. See 4.3.2 for further information.

Table 10: The photogrammetric sub-models covering G4 at S2

Name	# Smart Points	# Img.	GCP's	Overall RMS	PCS
G4_1S2_1L	0	9	A15, A16, A17, B15, R11, R2	0.703	687,737
G4_1S2_2L	3,405	12	A21, A23, B23, R7, R8	0.480	1,465,188
G4_1S2_1R	0	10	B15, B16, B17, CoordSys-Helper1R, R2, R3, R4	0.521	2,090,074
G4_1S2_2R	9,729	17	CoordSys-Helper_2R, R4, R5, R6, B22, B23	0.797	274,533
G4_2S2_1R	0	10	R14, R12, FromG4_1_1L, B20, R13, B18, B19	0.657	1,172,541

Table 11: The photogrammetric sub-models covering G4 at S3

Name	# Smart Points	# Img.	GCP's	Overall RMS	PCS
G4_1S3_1L	10,576	39	R11, A17, A16, R7, A22, A23, A15	0.54	1,358,760
G4_1S3_1R	3,852	24	R2, R3, B15, B16, B17	0.655	439,596
G4_1S3_2R	5,100	39	R3, R6, R4, R4, B23, B17, B22	0.805	2,467,271
G4_2S3_1R	8,527	37	B18, R12, B19, R14, B20, R13, R4	0.557	1,280,550

7.6.2 Photogrammetric Models - GCP Precision

Table 12: GCPs for absolute orientation (Type = Multipoint transform) and validation (Type=CheckPoint) in model G4_1S2_1L

Id -	Type -	Delta Distance /m	Delta X /m	Delta Y /m	Delta Z /m
A15	Multipoint transform	0.013	0.006	-0.012	-0.001
A16	Multipoint transform	0.006	-0.004	0.004	-0.002
A17	Check point	0.098	0.083	0.013	-0.051
B15	Multipoint transform	0.020	0.009	-0.018	0.000
R11	Multipoint transform	0.007	0.004	0.005	0.002
R2	Multipoint transform	0.026	-0.014	0.021	0.001

Table 13: GCPs for absolute orientation (Type = Multipoint transform) and validation (Type=CheckPoint) in model G4_2S2_2L

Id	Type	Delta Distance	Delta X	Delta Y	Delta Z
-	-	/m	/m	/m	/m
A21	Multipoint transform	0.015	0.001	0.003	0.014
A23	Multipoint transform	0.017	0.013	-0.003	0.010
B23	Multipoint transform	0.005	-0.005	-0.001	-0.002
R7	Multipoint transform	0.024	-0.005	0.017	-0.017
R8	Multipoint transform	0.015	-0.003	-0.014	-0.006

Table 14: GCPs for absolute orientation (Type = Multipoint transform) and validation (Type=CheckPoint) in model G4_1S2_1R

Id	Type	Delta Distance	Delta X	Delta Y	Delta Z
-	-	/m	/m	/m	/m
B15	Check point	0.012	0.012	-0.003	0.001
B16	Multipoint transform	0.031	0.003	0.030	0.007
B17	Check point	0.075	0.074	-0.009	-0.009
CoordSysHelper1R	Multipoint transform	0.035	0.003	-0.035	0.003
R2	Multipoint transform	0.026	-0.024	0.011	-0.001
R3	Multipoint transform	0.032	0.028	-0.004	-0.016
R4	Multipoint transform	0.012	-0.009	-0.002	0.007

Table 15: GCPs for absolute orientation (Type = Multipoint transform) and validation (Type=CheckPoint) in model G4_1S2_2R

Id	Type	Delta Distance	Delta X	Delta Y	Delta Z
-	-	/m	/m	/m	/m
CoordSysHelper_2R	Multipoint transform	0.101	-0.093	0.038	0.009
R4	Multipoint transform	0.061	0.061	0.008	0.001
R5	Multipoint transform	0.044	0.039	0.018	-0.008
R6	Check point	0.042	-0.001	-0.039	0.016
B22	Check point	0.039	0.018	-0.028	-0.020
B23	Multipoint transform	0.023	-0.023	0.002	0.001

Table 16: GCPs for absolute orientation (Type = Multipoint transform) and validation (Type=CheckPoint) in model G4_2S2_1R

Id	Type	Delta Distance	Delta X	Delta Y	Delta Z
-	-	/m	/m	/m	/m
R14	Multipoint transform	0.059	-0.048	0.021	0.027
R12	Check point	0.065	-0.034	-0.024	-0.050
FromG4_1_1L	Multipoint transform	0.026	-0.022	-0.003	0.014
B20	Check point	0.084	-0.019	-0.033	-0.075
R13	Multipoint transform	0.004	-0.001	0.004	-0.001
B18	Multipoint transform	0.053	0.034	-0.038	-0.014
B19	Multipoint transform	0.047	0.036	0.015	-0.026

Table 17: GCPs for absolute orientation (Type = Multipoint transform) and validation (Type=CheckPoint) in model G4_2S3_1L

Id	Type	Delta Distance	Delta X	Delta Y	Delta Z
-	-	/m	/m	/m	/m
R11	Check point	0.028	-0.017	0.000	0.023
A17	Multipoint transform	0.022	0.016	0.006	-0.014
A16	Multipoint transform	0.021	-0.011	-0.017	0.007
R7	Check point	0.018	-0.006	0.016	0.004
A22	Multipoint transform	0.013	0.008	-0.007	0.008
A23	Multipoint transform	0.012	-0.009	0.008	-0.002
A15	Multipoint transform	0.011	-0.003	0.010	0.000

Table 18: GCPs for absolute orientation (Type = Multipoint transform) and validation (Type=CheckPoint) in model G4_2S3_1R

Id	Type	Delta Distance	Delta X	Delta Y	Delta Z
-	-	/m	/m	/m	/m
R2	Check point	0.030	0.023	0.016	0.011
R3	Check point	0.015	-0.012	-0.006	-0.007
B15	Multipoint transform	0.033	-0.008	-0.026	-0.018
B16	Multipoint transform	0.031	-0.023	0.019	0.010
B17	Multipoint transform	0.021	0.020	-0.003	0.004

Table 19: GCPs for absolute orientation (Type = Multipoint transform) and validation (Type=CheckPoint) in model G4_1S3_2R

Id	Type	Delta Distance	Delta X	Delta Y	Delta Z
-	-	/m	/m	/m	/m
R3	Check point	0.042	0.027	0.027	0.018
R6	Multipoint transform	0.039	0.002	-0.039	0.005
R4	Check point	0.026	0.004	0.024	0.010
R4	Multipoint transform	0.026	0.004	0.024	0.010
B23	Multipoint transform	0.026	0.001	0.024	-0.009
B17	Multipoint transform	0.024	0.010	-0.017	-0.014
B22	Multipoint transform	0.020	-0.017	0.008	0.008

Table 20: GCPs for absolute orientation (Type = Multipoint transform) and validation (Type=CheckPoint) in model G4_2S3_1R

Id	Type	Delta Distance	Delta X	Delta Y	Delta Z
-	-	/m	/m	/m	/m
B18	Check point	0.051	0.028	-0.041	-0.011
R12	Check point	0.025	0.020	0.014	0.008
B19	Multipoint transform	0.023	0.012	0.020	-0.003
R14	Multipoint transform	0.016	-0.013	-0.008	-0.001
B20	Multipoint transform	0.013	-0.009	-0.009	-0.002
R13	Multipoint transform	0.012	0.010	-0.003	0.006
R4	Multipoint transform	0.012	-0.009	-0.002	0.007

7.6.3 Thinning of DSM Point clouds

Table 21: Shape files of gully 4 recording session 2 for the import into the GIS system.

Shape File	File size	Points
-	/Mb	-
G4S2_A.shp	159.84	3,809,227
G4S2_A_001thin.shp	21.67	516,507
G4S2_A_002thin.shp	6.51	155,231
G4S2_A_005thin.shp	1.23	29,227
G4S2_A_01thin.shp	0.34	7,992
G4S2_A_02thin.shp	0.09	2225
G4S2_A_03thin.shp	0.05	1075
G4S2_F.shp	130.76	3,116,132
G4S2_F_001thin.shp	17.64	420,343
G4S2_F_002thin.shp	5.65	134,745

Table 22: Shape files of gully 4 recording session 3 for the import into the GIS system.

Shape File	File size	Points
-	/Mb	-
G4S3_A.shp	232.73	5,546,289
G4S3_A_001thin.shp	27.99	667,073
G4S3_A_002thin.shp	7.54	179,795
G4S3_A_005thin.shp	1.27	30,325
G4S3_A_01thin.shp	0.33	7,964
G4S3_A_02thin.shp	0.09	2169
G4S3_A_03thin.shp	0.04	1027
G4S3_F.shp	149.65	3,566,250
G4S3_F_001thin.shp	19.89	474,008
G4S3_F_002thin.shp	6.14	146,339

8 List of Figures, List of Tables

List of Figures

List of Tables